

# ***A Mathematical and Experimental Study of Anchor Ice***

---

By Yuexia Qu

A thesis submitted to the Faculty of Graduate Studies in partial fulfillment of the requirements for the degree of

**Doctor of Philosophy**

Department of Civil Engineering  
University of Manitoba

Winnipeg, Manitoba, Canada

December, 2006

© Yuexia Qu, 2006

---

**THE UNIVERSITY OF MANITOBA**  
**FACULTY OF GRADUATE STUDIES**  
\*\*\*\*\*  
**COPYRIGHT PERMISSION**

**A Mathematical and Experimental Study of Anchor Ice**

**by**

**Yuexia Qu**

**A Thesis/Practicum submitted to the Faculty of Graduate Studies of The University of**

**Manitoba in partial fulfillment of the requirement of the degree**

**of**

**Doctor of Philosophy**

**Yuexia Qu © 2006**

**Permission has been granted to the Library of the University of Manitoba to lend or sell copies of this thesis/practicum, to the National Library of Canada to microfilm this thesis and to lend or sell copies of the film, and to University Microfilms Inc. to publish an abstract of this thesis/practicum.**

**This reproduction or copy of this thesis has been made available by authority of the copyright owner solely for the purpose of private study and research, and may only be reproduced and copied as permitted by copyright laws or with express written authorization from the copyright owner.**

---

---

## ABSTRACT

The existence of anchor ice in supercooled water can have a profound impact on the management of water resource infrastructures in cold regions. For example, it can raise a tailrace water level and cause significant losses in generation revenue. So far, there have been limited studies on anchor ice, therefore, many problems still exist and much more study is needed. In the present research, experimental and mathematical studies of anchor ice were carried out.

Experiments were conducted in a counter-rotating flume, located in a cold room at the University of Manitoba. The experiments were mainly focused on anchor ice evolution around rocks and on gravel beds under different hydro-meteorological conditions. The results are compared to a mathematical model developed herein and some important parameters such as anchor ice porosity and frazil ice deposition coefficient are examined. The growth process of anchor ice was monitored by two CCD cameras. A digital processing program was developed to analyze anchor ice images and determine the growth rate of anchor ice. In addition, anchor ice density, an important factor when studying anchor ice, was estimated and the effect of air temperature, Froude number and Reynolds number is explored. By analyzing torque load signals from the counter-rotating flume, the variation of bed roughness with the growth of anchor ice is elucidated. The deposition coefficient of anchor ice growth was also determined from the experiments.

---

---

A mathematical model was developed based on a two-stage method to simulate the process of frazil ice transportation and deposition. Both frazil ice attachment and heat transfer between the supercooled water and ice crystals are considered in the model. Four governing equations related to the distribution of velocity and frazil ice transportation and deposition inside and outside the roughness layers were built. A fourth-order Runge-Kutta numerical method was used and programmed in Matlab to solve the governing equations. The growth rate of anchor ice under different hydro-meteorological conditions can be simulated by this numerical model.

The proposed experimental and mathematical studies of anchor ice are presented intuitively in this paper and the results from this study contribute to a better understanding of the anchor ice growth mechanism. This study will help to develop better management strategies to mitigate ice related complications associated with hydroelectric generating stations and other hydraulic structures in cold regions.

---

---

## ACKNOWLEDGEMENTS

The assistance and support of many people over the past four years allowed me to complete this thesis. The names of a few follow.

I would like to thank Dr. J. Doering, my advisor, who has provided endless support, guidance, and encouragement throughout my graduate studies. It has been a great pleasure to have been one of Dr. Doering's students and it is a time that I will always be proud of. Thanks also go to my examining committee members, Dr. Rasmussen, Dr. Tachie and Mr. Carson for their questions and contributions to this thesis.

I would like to thank Mr. Roy Hartle who helped immensely in the completion of this study. Thanks also go to other graduate students in the HTRF whom I have been working with throughout the years. They have helped me a lot on my English and research and they have made my academic experience very enjoyable.

My husband has provided support and encouragement through my years of graduate studies. Special thanks go to Ruth and Frank Vust who have supported and encouraged me through hard times.

Many thanks go to the University of Manitoba for honoring me with a graduate fellowship and to Manitoba Hydro, for supporting the research financially.

---

---

# Table of Contents

<b>Abstract.....</b>	<b>i</b>
<b>Acknowledgements.....</b>	<b>iii</b>
<b>Table of Contents.....</b>	<b>iv</b>
<b>List of Figures.....</b>	<b>vii</b>
<b>List of Tables.....</b>	<b>xvi</b>
<b>Nomenclature.....</b>	<b>xvii</b>
<b>Chapter 1. Introduction.....</b>	<b>1</b>
1.1 General Description of Anchor Ice.....	1
1.1.1 Anchor Ice Formed by Underwater Nucleation.....	2
1.1.2 Anchor Ice Formed by Frazil Adhesion.....	3
1.1.3 Limitation on Thickness of Anchor Ice.....	4
1.1.4 Effects of Anchor ice.....	5
1.2 Literature Review.....	7
1.2.1 Theoretical Model of Anchor Ice.....	7
1.2.2 Experimental Study of Anchor Ice.....	9
1.2.3 Field Study.....	11
1.3 Study Objectives.....	12
<b>Chapter 2. Experimental Setting.....</b>	<b>17</b>
2.1 Introduction of Counter-rotating Flume.....	17
2.2 Velocity Calibration of the Counter-rotating Flume.....	19
2.3 Data Acquisition Systems.....	19
2.3.1 Temperature Recording Equipment.....	19
2.3.2 Image Recording Equipment.....	20
2.3.3 Torque Load Measurement Equipment.....	21
2.4 Digital Image Processing.....	21
2.4.1 Removal of Background Lights.....	22
2.4.2 Morphological Operations.....	23
2.4.3 Pixel Calibration and Conversion.....	24
<b>Chapter 3. Anchor Ice Evolution around Rocks and on Gravel Beds.....</b>	<b>37</b>
3.1 Introduction.....	37
3.2 Evolution of Anchor Ice around Rocks.....	37

3.2.1	Evolution of Anchor Ice Around One Rock.....	39
3.2.2	Evolution of Anchor Ice on Five Rocks in a Row.....	40
3.2.3	Evolution of Anchor Ice on Six Rocks in Two Row.....	41
3.3	Evolution of Anchor Ice on Gravel Beds.....	42
3.3.1	Scale Type of Anchor Ice.....	42
3.3.2	Ball Type of Anchor Ice.....	43
3.4	Anchor Ice Release on Gravel Beds.....	43
3.5	In-situ Thermo Growth.....	44
<b>Chapter 4. Anchor Ice Growth on Gravel Beds.....</b>		<b>60</b>
4.1	Introduction.....	61
4.2	Anchor Ice Density and Porosity.....	61
4.2.1	Measurement of Anchor Ice Density.....	61
4.2.2	Effect of Flow Parameters on Anchor Ice Density.....	62
4.2.2.1	Effect of Froude Number.....	63
4.2.2.2	Effect of the Gravel Reynolds Number.....	63
4.3	Variation of the Bed/ice Surface Roughness.....	64
4.3.1	Analysis of the Torque Load Signals.....	64
4.3.2	Derivation of Manning's n.....	65
4.3.3	Analysis the Measured Manning's n.....	66
4.3.4	Effect of Air Temperature and Flow Parameters on Manning's n.....	68
4.3.4.1	Effect of the Air Temperature.....	68
4.3.4.2	Effect of the Velocity.....	69
4.3.4.3	Effect of Froude and Reynolds Numbers.....	69
4.4	Growth Rate of Anchor Ice.....	70
4.4.1	Analysis of the Growth Rate of Anchor Ice.....	69
4.4.2	Effect of Air Temperature and Flow Parameters.....	72
4.4.2.1	Effect of the Air Temperature.....	72
4.4.2.2	Effect of the Gravel Bed Roughness.....	73
4.4.2.3	Effect of the Froude Number.....	74
<b>Chapter 5. Turbulence, Frazil Ice Transportation and Deposition Theory.....</b>		<b>97</b>
5.1	Turbulent Characteristics.....	97
5.1.1	Shear Velocity of Turbulent Flow.....	98
5.1.2	Eddy Diffusivity of Turbulence.....	99
5.1.3	Problems with Rough Surface.....	101
5.1.4	Effect of Roughness on Turbulent Intensity.....	103
5.2	Frazil Ice Transportation and Deposition Theory.....	104
5.2.1	Basic Principle.....	104
5.2.2	Introduction of Transport Equation.....	105
5.2.3	Rise Velocity of Frazil Ice.....	107
5.2.4	Deposition Theory.....	109
<b>Chapter 6. Numerical Simulation.....</b>		<b>112</b>

---



---

6.1 Heat Exchange Theory.....	112
6.1.1 Heat Transfer between Frazil Ice and Supercooled Water.....	113
6.1.2 Heat Exchange Between Anchor Ice and Supercooled Water.....	115
6.2 Model Formulation.....	116
6.2.1 Velocity Distribution Outside the Roughness Layer.....	116
6.2.2 Frazil Ice Transport Outside the Roughness Layer.....	117
6.2.3 Velocity Distribution Inside the Roughness Layer.....	118
6.2.4 Frazil Ice Transport and Deposition Inside the Roughness Layer.....	120
6.2.5 Boundary Conditions.....	120
6.2.6 Average Growth Rate of Anchor Ice.....	121
6.3 Result Discussion.....	122
6.3.1 Deposition Coefficient.....	123
6.3.2 Comparison of the Experimental and Theoretical Results.....	124
6.4 Release Theory of Anchor Ice.....	125
6.4.1 Melting Release of Anchor Ice.....	125
6.4.2 Buoyancy Release of Anchor Ice.....	126
<b>Chapter 7. Summary and Future Work.....</b>	<b>134</b>
7.1 Introduction.....	134
7.2 Summary.....	135
7.3 Conclusions.....	143
7.4 Future Work.....	144
<b>Reference.....</b>	<b>146</b>
<b>Appendix A Calibration Curves of the Counter-rotating Flume.....</b>	<b>152</b>
<b>Appendix B Water Temperature Measurements.....</b>	<b>156</b>
<b>Appendix C Anchor Ice Thickness and Growth Rate Measurements.....</b>	<b>169</b>
<b>Appendix D The Runge-Kutta Method.....</b>	<b>195</b>

---

## List of Figures

<b>Figure 1.1.</b>	Anchor ice bridge formed at Sundance Rapids downstream of Limestone Generation station.....	15
<b>Figure 1.2.</b>	Side view of anchor ice (Doering et al., 2001).....	16
<b>Figure 2.1.</b>	The counter-rotating flume.....	26
<b>Figure 2.2.</b>	The schematics of the bed and wall rotating frames.....	26
<b>Figure 2.3.</b>	The cold room.....	27
<b>Figure 2.4.</b>	Three bedplates with different size of gravels 0.34, 1 and 2 cm.....	27
<b>Figure 2.5.</b>	Kent-Lea probe used in the velocity calibration of the counter-rotating flume.....	28
<b>Figure 2.6.</b>	(a) The calibration curve when bed roughness is 0.34 cm and water depth is 10 cm, (b) The calibration curve when bed roughness is 1cm and water depth is 10 cm, (c) The calibration curve when bed roughness is 2cm and water depth is 10 cm .....	29
<b>Figure 2.7.</b>	The fluke black stack thermometer.....	31
<b>Figure 2.8.</b>	The thermometer probe.....	31
<b>Figure 2.9.</b>	Cross polarized light scheme.....	32
<b>Figure 2.10.</b>	A sketch of the position of the two cameras.....	32
<b>Figure 2.11.</b>	(a) Anchor ice image before the subtraction of the background lights, (b) Anchor ice image after the subtraction of the background lights.....	33
<b>Figure 2.12.</b>	Anchor ice images before and after digital image processing.....	34
<b>Figure 2.13.</b>	(a) Conversion image when the roughness height is 0.34 cm, (b) Conversion image when the roughness is 1 cm, (c) Conversion image when the roughness is 2 cm.....	35
<b>Figure 3.1.</b>	(a) - (d) Attachment of frazil ice to the gravel bottom.....	47

<b>Figure 3.2.</b>	(a)-(f) Anchor ice evolution around one rock when the bed velocity is 0.38 m/s, water depth is 10 cm and the air temperature is -16°C, (g) A sketch of the sequence of anchor ice development around one rock.....	48
<b>Figure 3.3.</b>	(a)-(c) Anchor ice growth when air temperature is -12 °C.....	49
<b>Figure 3.4.</b>	(a)-(c) Anchor ice growth when air temperature is -16°C.....	49
<b>Figure 3.5.</b>	(a)-(c) Anchor ice growth when air temperature is -20 °C.....	50
<b>Figure 3.6.</b>	(a)-(f) Anchor ice evolution around five rocks in a row when the velocity is 0.38 m/s, water depth is 10 cm and the air temperature is -16°C, (g) A sketch of the sequence of anchor ice development around the five rocks.....	51
<b>Figure 3.7.</b>	A top view of anchor ice grown on a row of rocks.....	52
<b>Figure 3.8.</b>	(a)–(d) Anchor ice evolution on six rocks when the velocity is 0.38 m/s, water depth is 10 cm and the air temperature is -16°C.....	53
<b>Figure 3.9.</b>	A top view of anchor ice on six rocks.....	54
<b>Figure 3.10.</b>	(a)–(d) Evolution of scale shaped anchor ice when the velocity is 0.23 m/s, water depth is 10 cm, the air temperature is -16°C, and the Froude number is 0.23, (e) A sketch of the development of scale shaped anchor ice.....	55
<b>Figure 3.11.</b>	(a)–(d) Evolution of ball shaped anchor ice when the velocity is 0.57 m/s, water depth is 8 cm, air temperature is -16°C, and Froude number is 0.64, (e) A sketch of the development of ball shaped anchor ice.....	56
<b>Figure 3.12.</b>	(a)–(d) Release of anchor ice due to the buoyant force when the velocity is 0.38 m/s, water depth is 8 cm, air temperature is -16°C and the gravel Reynolds number is 56.....	57
<b>Figure 3.13.</b>	Release of a big piece of anchor ice.....	58
<b>Figure 3.14.</b>	Floating anchor ice slush after releasing.....	58
<b>Figure 3.15.</b>	Schematic heat balance in a water body.....	59
<b>Figure 3.16.</b>	The temperature curve when the velocity is 0.38 m/s, water depth is 10 cm, and air temperature is -20°C.....	59

<b>Figure 4.1.</b>	Procedure of the experiments.....	75
<b>Figure 4.2.</b>	Taking out of anchor ice slush.....	76
<b>Figure 4.3.</b>	(a) Anchor ice image before digital image processing, (b) Anchor ice image after digital image processing.....	77
<b>Figure 4.4.</b>	Effect of Froude number on anchor ice densities when the air Temperature is $-16^{\circ}\text{C}$ .....	78
<b>Figure 4.5.</b>	The best linear regression between anchor ice porosity and gravel Reynolds number.....	79
<b>Figure 4.6.</b>	(a) The original torque load signals, (b) The original ice torque load signals, (c) The distribution of reference torque load signals, (d) The distribution of the ice torque load data, when the air temperature is $-16^{\circ}\text{C}$ , the velocity is 0.23 m/s and the gravel bed roughness is 2 cm.....	80
<b>Figure 4.7.</b>	(a) The change of relative Manning's n with the growth of anchor ice, (b) The change of absolute Manning's n with the growth of anchor ice when the water temperature is $-16^{\circ}\text{C}$ , the velocity is 0.23m/s and the gravel roughness is 2cm .....	82
<b>Figure 4.8.</b>	(a)–(c) Actual anchor ice images corresponding to different stages of bed/ice surface roughness change.....	84
<b>Figure 4.9.</b>	(a) The relative Manning's n, (b) The absolute Manning's n under different air temperature when the water depth is 8 cm, the gravel bed roughness is 1 cm, and the velocity is 0.38 m/s.....	85
<b>Figure 4.10.</b>	(a) The relative Manning's n, (b) The absolute Manning's n under different air temperature when the water depth is 10 cm, the gravel bed roughness is 0.34 cm, and the velocity is 0.38 m/s.....	86
<b>Figure 4.11.</b>	The variation of the relative Manning's n with the growth of anchor ice when the gravel bed roughness is 1 cm, the air temperature is $-16^{\circ}\text{C}$ and water depth is 8 cm.....	87
<b>Figure 4.12.</b>	The change of the relative Manning's n with the growth of anchor ice when gravel bed roughness is 2 cm, the air temperature is $-16^{\circ}\text{C}$ and water depth is 10 cm.....	87

<b>Figure 4.13.</b>	The effect of Froude number on the variation of the relative Manning's n.....	88
<b>Figure 4.14.</b>	The effect of Froude number on the mean relative Manning's n.....	88
<b>Figure 4.15.</b>	The effect of Reynolds number on the mean relative Manning's n....	89
<b>Figure 4.16.</b>	Supercooling curve with superimposed growth rate of anchor ice....	89
<b>Figure 4.17.</b>	(a), (b) Anchor ice thickness and growth rate when the water depth is 10 cm, roughness height is 0.34 cm, flow velocity is 0.38 m/s and air temperature is -16°C.....	90
<b>Figure 4.18.</b>	(a), (b) Anchor ice thickness and growth rate when the water depth is 8 cm, roughness height is 0.34 cm, flow velocity is 0.23 m/s and air temperature is -16°C.....	91
<b>Figure 4.19.</b>	(a), (b) The thickness and growth rate of anchor ice under different air temperatures.....	92
<b>Figure 4.20.</b>	(a), (b) The thickness and growth rate of anchor ice under different roughness heights.....	93
<b>Figure 4.21.</b>	(a) 30 minute after, roughness height is 2 cm, (b) 30 minute after, roughness height is 0.34 cm.....	94
<b>Figure 4.22.</b>	(a), (b) The thickness and growth rate of anchor ice under different Froude numbers.....	95
<b>Figure 4.23.</b>	Time of the peak growth rate of anchor ice under different Froude numbers.....	96
<b>Figure 5.1.</b>	Schematic description of turbulent flow on roughness surface.....	111
<b>Figure 5.2.</b>	The control volume of water body.....	111
<b>Figure 6.1.</b>	The flow chart of the process of solving the governing equations....	128
<b>Figure 6.2.</b>	(a), (b) Relationship between the deposition coefficient and Reynolds Number when Roughness is 1 cm and 2 cm respectively.....	129
<b>Figure 6.3.</b>	Velocity distribution along the flow depth from the numerical model	130
<b>Figure 6.4.</b>	Frazil ice concentration along the flow depth from the numerical model.....	131

<b>Figure 6.5.</b>	(a), (b) Comparison between experimental and numerical results....	132
<b>Figure 6.6.</b>	Determination of valid area.....	133
<b>Figure A1.</b>	Velocity calibration curve when bed roughness is 0.34 cm and water depth is 8 cm.....	153
<b>Figure A2.</b>	Velocity calibration curve when bed roughness is 0.34 cm and water depth is 12 cm.....	153
<b>Figure A3.</b>	Velocity calibration curve when bed roughness is 1 cm and water depth is 8 cm.....	154
<b>Figure A4.</b>	Velocity calibration curve when bed roughness is 1 cm and water depth is 12 cm.....	154
<b>Figure A5.</b>	Velocity calibration curve when bed roughness is 2 cm and water depth is 12 cm.....	155
<b>Figure B1.</b>	Water temperature curve from Exp. 3-2 when the bed velocity is 0.57 m/s, water depth is 0.1 m and air temperature is -20°C.....	157
<b>Figure B2.</b>	Water temperature curve from Exp. 3-3 when the bed velocity is 0.57 m/s, water depth is 0.1 m and air temperature is -16°C.....	157
<b>Figure B3.</b>	Water temperature curve from Exp. 3-4 when the bed velocity is 0.75 m/s, water depth is 0.1 m and air temperature is -16°C.....	158
<b>Figure B4.</b>	Water temperature curve from Exp. 3-5 when the bed velocity is 0.57 m/s, water depth is 0.1 m and air temperature is -12°C.....	158
<b>Figure B5.</b>	Water temperature curve from Exp. 3-9 when the bed velocity is 0.38 m/s, water depth is 0.12 m and air temperature is -16°C.....	159
<b>Figure B6.</b>	Water temperature curve from Exp. 3-10 when the bed velocity is 0.57 m/s, water depth is 0.12 m and air temperature is -20°C.....	159

<b>Figure B7.</b>	Water temperature curve from Exp. 3-12 when the bed velocity is 0.57 m/s, water depth is 0.12 m and air temperature is -16°C.....	160
<b>Figure B8.</b>	Water temperature curve from Exp. 3-15 when the bed velocity is 0.57 m/s, water depth is 0.12 m and air temperature is -12°C.....	160
<b>Figure B9.</b>	Water temperature curve from Exp. 3-16 when the bed velocity is 0.75 m/s, water depth is 0.12 m and air temperature is -16°C.....	161
<b>Figure B10.</b>	Water temperature curve from Exp. 3-17 when the bed velocity is 0.38 m/s, water depth is 0.08 m and air temperature is -12°C.....	161
<b>Figure B11.</b>	Water temperature curve from Exp. 4-5 when the bed velocity is 0.38 m/s, water depth is 0.1 m and air temperature is -20°C.....	162
<b>Figure B12.</b>	Water temperature curve from Exp. 4-6 when the bed velocity is 0.38 m/s, water depth is 0.1 m and air temperature is -16°C.....	162
<b>Figure B13.</b>	Water temperature curve from Exp. 4-7 when the bed velocity is 0.57 m/s, water depth is 0.1 m and air temperature is -16°C.....	163
<b>Figure B14.</b>	Water temperature curve from Exp. 4-9 when the bed velocity is 0.38 m/s, water depth is 0.1 m and air temperature is -12°C.....	163
<b>Figure B15.</b>	Water temperature curve from Exp. 4-12 when the bed velocity is 0.38 m/s, water depth is 0.12 m and air temperature is -16°C.....	164
<b>Figure B16.</b>	Water temperature curve from Exp. 4-14 when the bed velocity is 0.57 m/s, water depth is 0.12 m and air temperature is -16°C.....	164
<b>Figure B17.</b>	Water temperature curve from Exp. 4-25 when the bed velocity is 0.38 m/s, water depth is 0.1 m and air temperature is -20°C.....	165

<b>Figure B18.</b>	Water temperature curve from Exp. 4-27 when the bed velocity is 0.38 m/s, water depth is 0.1 m and air temperature is -12°C.....	165
<b>Figure B19.</b>	Water temperature curve from Exp. 4-29 when the bed velocity is 0.57 m/s, water depth is 0.1 m and air temperature is -16°C.....	166
<b>Figure B20.</b>	Water temperature curve from Exp. 4-30 when the bed velocity is 0.38 m/s, water depth is 0.12 m and air temperature is -20°C.....	166
<b>Figure B21.</b>	Water temperature curve from Exp. 5-2 when the bed velocity is 0.38 m/s, water depth is 0.12 m and air temperature is -16°C.....	167
<b>Figure B22.</b>	Water temperature curve from Exp. 5-4 when the bed velocity is 0.38 m/s, water depth is 0.12 m and air temperature is -12°C.....	167
<b>Figure B23.</b>	Water temperature curve from Exp. 5-5 when the bed velocity is 0.57 m/s, water depth is 0.12 m and air temperature is -16°C.....	168
<b>Figure C1.</b>	(a) Anchor ice thickness, (b) Anchor ice growth rate from Exp. 2-23 when the bed velocity is 0.38 m/s, water depth is 0.1 m and air temperature is -16°C.....	170
<b>Figure C2.</b>	(a) Anchor ice thickness, (b) Anchor ice growth rate from Exp. 2-24 when the bed velocity is 0.38 m/s, water depth is 0.1 m and air temperature is -12°C.....	171
<b>Figure C3.</b>	(a) Anchor ice thickness, (b) Anchor ice growth rate from Exp. 3-4 when the bed velocity is 0.75 m/s, water depth is 0.1 m and air temperature is -16°C.....	172
<b>Figure C4.</b>	(a) Anchor ice thickness, (b) Anchor ice growth rate from Exp. 3-8 when the bed velocity is 0.38 m/s, water depth is 0.12 m and air temperature is -20°C.....	173
<b>Figure C5.</b>	(a) Anchor ice thickness, (b) Anchor ice growth rate from Exp. 3-9 when the bed velocity is 0.38 m/s, water depth is 0.12 m and air temperature is -16°C.....	174

<b>Figure C6.</b>	(a) Anchor ice thickness, (b) Anchor ice growth rate from Exp. 3-10 when the bed velocity is 0.57 m/s, water depth is 0.12 m and air temperature is -20°C.....	175
<b>Figure C7.</b>	(a) Anchor ice thickness, (b) Anchor ice growth rate from Exp. 3-18 when the bed velocity is 0.38 m/s, water depth is 0.08 m and air temperature is -16°C.....	176
<b>Figure C8.</b>	(a) Anchor ice thickness, (b) Anchor ice growth rate from Exp. 3-19 when the bed velocity is 0.38 m/s, water depth is 0.08 m and air temperature is -20°C.....	177
<b>Figure C9.</b>	(a) Anchor ice thickness, (b) Anchor ice growth rate from Exp. 3-21 when the bed velocity is 0.57 m/s, water depth is 0.08 m and air temperature is -20°C.....	178
<b>Figure C10.</b>	(a) Anchor ice thickness, (b) Anchor ice growth rate from Exp. 3-22 when the bed velocity is 0.57 m/s, water depth is 0.08 m and air temperature is -16°C.....	179
<b>Figure C11.</b>	(a) Anchor ice thickness, (b) Anchor ice growth rate from Exp. 3-23 when the bed velocity is 0.57 m/s, water depth is 0.08 m and air temperature is -12°C.....	180
<b>Figure C12.</b>	(a) Anchor ice thickness, (b) Anchor ice growth rate from Exp. 3-30 when the bed velocity is 0.38 m/s, water depth is 0.08 m and air temperature is -20°C.....	181
<b>Figure C13.</b>	(a) Anchor ice thickness, (b) Anchor ice growth rate from Exp. 3-31 when the bed velocity is 0.38 m/s, water depth is 0.08 m and air temperature is -16°C.....	182
<b>Figure C14.</b>	(a) Anchor ice thickness, (b) Anchor ice growth rate from Exp. 4-1 when the bed velocity is 0.38 m/s, water depth is 0.08 m and air temperature is -12°C.....	183
<b>Figure C15.</b>	(a) Anchor ice thickness, (b) Anchor ice growth rate from Exp. 4-2 when the bed velocity is 0.57 m/s, water depth is 0.08 m and air temperature is -16°C.....	184
<b>Figure C16.</b>	(a) Anchor ice thickness, (b) Anchor ice growth rate from Exp. 4-5 when the bed velocity is 0.38 m/s, water depth is 0.1 m and air temperature is -20°C.....	185

---

<b>Figure C17.</b>	(a) Anchor ice thickness, (b) Anchor ice growth rate from Exp. 4-6 when the bed velocity is 0.38 m/s, water depth is 0.1 m and air temperature is -16°C.....	186
<b>Figure C18.</b>	(a) Anchor ice thickness, (b) Anchor ice growth rate from Exp. 4-7 when the bed velocity is 0.57 m/s, water depth is 0.1 m and air temperature is -16°C.....	187
<b>Figure C19.</b>	(a) Anchor ice thickness, (b) Anchor ice growth rate from Exp. 4-9 when the bed velocity is 0.38 m/s, water depth is 0.1 m and air temperature is -12°C.....	188
<b>Figure C20.</b>	(a) Anchor ice thickness, (b) Anchor ice growth rate from Exp. 4-12 when the bed velocity is 0.38 m/s, water depth is 0.12 m and air temperature is -16°C.....	189
<b>Figure C21.</b>	(a) Anchor ice thickness, (b) Anchor ice growth rate from Exp. 4-14 when the bed velocity is 0.57 m/s, water depth is 0.12 m and air temperature is -16°C.....	190
<b>Figure C22.</b>	(a) Anchor ice thickness, (b) Anchor ice growth rate from Exp. 4-19 when the bed velocity is 0.38 m/s, water depth is 0.08 m and air temperature is -20°C.....	191
<b>Figure C23.</b>	(a) Anchor ice thickness, (b) Anchor ice growth rate from Exp. 4-20 when the bed velocity is 0.38 m/s, water depth is 0.08 m and air temperature is -16°C.....	192
<b>Figure C24.</b>	(a) Anchor ice thickness, (b) Anchor ice growth rate from Exp. 5-4 when the bed velocity is 0.38 m/s, water depth is 0.12 m and air temperature is -12°C.....	193
<b>Figure C25.</b>	(a) Anchor ice thickness, (b) Anchor ice growth rate from Exp. 5-5 when the bed velocity is 0.57 m/s, water depth is 0.12 m and air temperature is -16°C.....	194

---

---

## List of Tables

<b>Table 2.1.</b>	Table of conversion equations.....	25
<b>Table 3.1.</b>	Experimental parameters of anchor ice evolution around rocks.....	38
<b>Table 4.1.</b>	Summarization of flow parameters and anchor ice densities.....	62
<b>Tabel 4.2.</b>	Summary of flow parameters and absolute Manning's n.....	68
<b>Tabel 4.3.</b>	Summary of flow parameters and experimental anchor ice growth rate..	72
<b>Table 6.1.</b>	Summary of the flow conditions and anchor ice growth rate.....	122
<b>Table 6.2.</b>	Parameters and numerical results of Hammar's numerical model.....	123

---



---

## Nomenclature

Symbol	Units	Physical Definition
$A$		constant
$A_b$	$m^2$	area of the flume bed
$A_c$	$m^2$	cross sectional area of the flow
$A_e$	$m^2$	mean ice particle area in the growing direction
$A_p$	$m^2$	projected area of the frazil disc
$A_s$	$m^2$	characteristic particle cross-section area
$A_t$	$^{\circ}C$	air temperature
$b$		constant
$C$		volume concentration of frazil ice
$C_b$		volume concentration at the river bottom
$C_d$		drag coefficient
$C_R$	$^{\circ}C/s$	supercooling rate
$C_{\mu}$		constant
$d$	$m$	the displacement height
$d_f$	$m$	mean face diameter of frazil particle
$d_e$	$m$	characteristic length of ice particle
$d_p$	$m$	diameter of particles
$d_s$	$m$	diameter of gravel
$D_l$		constant
$D_B$		Brownian diffusivity
$D_H$	$m$	hydraulic diameter
$D_x$	$m$	bed gravel diameter in the streamwise direction
$e_a$		porosity of anchor ice
$f$		Darcy friction factor
$f_d$	$N/m^3$	total drag force per unit volume of the fluid
$f_m$	$N$	friction force

---



---

$F$	$N$	drag force
$F_b$	$N$	buoyant force
$F_r$		Froude Number
$g$	$m/s^2$	gravity acceleration
$g'$	$m/s^2$	reduced gravity acceleration
$G_{re}$	$m/s$	experimental average growth rate of anchor ice
$G_{rt}$	$m/s$	theoretical growth rate of anchor ice
$J$		the flux of particles in $y$ direction
$h_a$	$m$	thickness of anchor ice
$h_{awi}$	$W m^{-2} / ^\circ C$	heat transfer between water and anchor ice
$h_{mh}$	$m$	melting height of anchor ice
$\bar{h}$		average convection heat-transfer coefficient
$H$	$m$	water depth
$k$		turbulent kinetic energy
$\bar{k}$		average turbulent kinetic energy
$k_s$	$m$	equivalent roughness height
$k_w$	$W/m^\circ C$	thermal conductivity of water, 0.5659
$l$	$m$	characteristic length of ice particle
$L$	$J/kg$	latent heat of ice
$n$		Manning's $n$
$N_m$	$N$	weights
$N_u$		Nusselt number
$P$	$m$	the wetted perimeter
$P_r$		Prandtl number
$\bar{P}$	$N/m^2$	average pressure
$q$	$W m^{-2}$	convection heat transfer per unit ice area
$q_a$	$W m^{-2}$	heat flux from anchor ice to channel flow
$Q$	$m^3/s$	the flux through a unit area
$Q_{aw}$	$W$	heat exchange between air and water
$Q_i$	$W$	heat release due to ice formation

---



---

$Q_w$	$W$	heat exchange due to water temperature variation
$r$	$m$	center radius of the flume bed
$r_f$	$m$	radius of frazil ice particles
$\hat{r}$	$m$	major linear dimension of frazil ice
$R$	$m$	hydraulic radius
$R_e$		Reynolds number
$R^*$		gravel Reynolds number
$s$	$m$	the stopping distance
$S$		channel slope
$S_c$		source term due to the thermal growth
$S_{cp}$		Schmidt number
$S_f$		friction slope
$S_y$		deposition rate of frazil particles
$S_*$		total deposition rate along the roughness layer
$t$	$s$	time
$T_i$	$^{\circ}C$	ice surface temperature
$T_{torque}$	$N.m$	torque load
$T_w$	$^{\circ}C$	water temperature
$u$	$m/s$	velocity at a distance $y$ from the boundary
$u_{max}$	$m/s$	maximum velocity at the outer edge of the boundary layer
$u_{cr1}$	$m/s$	low critical velocity of flow
$u_{cr2}$	$m/s$	high critical velocity of flow
$u_h$	$m/s$	velocity of the edge of the roughness layer
$u_*$	$m/s$	friction velocity at the bottom
$\bar{u}$	$m/s$	time-averaged velocity components of $u$
$u'$	$m/s$	fluctuate velocity component of $u$
$U$	$m/s$	mean flow velocity
$V$	$m/s$	flume bed velocity
$V_{ai}$	$m^3$	volume of anchor ice
$V_i$	$m^3$	volume of frazil ice

---



---

$v_{p0}$	$m/s$	The initial velocity of particles
$v'$	$m/s$	fluctuate velocity component of $v$
$V_i$	$m^3$	volume of anchor ice
$V_s$	$m^3$	volume of bed material
$w$	$m/s$	velocity across the flow direction
$W_a$	$lb$	weight of anchor ice
$w'$	$m/s$	fluctuate velocity component of $w$
$w_b$	$m/s$	buoyant velocity
$y$	$m$	vertical distance measured from the bed
$y_0$	$m$	roughness length
$\alpha$		attenuation coefficient, typically 1 ~ 2
$\alpha_T$		turbulence intensity
$\bar{\Gamma}$		certain time-averaged physical item
$\nu_T$	$m^2/s$	eddy viscosity of the fluid
$\nu_p$	$m^2/s$	eddy viscosity
$\nu$	$m^2/s$	kinematic viscosity
$\mu$	$kg/m/s$	dynamic viscosity
$\mu_d$		dynamic friction coefficient
$\rho$	$kg/m^3$	fluid density
$\rho_a$	$kg/m^3$	density of anchor ice
$\rho_i$	$kg/m^3$	the density of ice
$\rho_p$	$kg/m^3$	the density of particle
$\rho_s$	$kg/m^3$	density of bed materials
$\rho_w$	$kg/m^3$	the density of water
$\tau$	$N/m^2$	local shear stress
$\tau_0$	$N/m^2$	boundary shear stress
$\tau_p$	$N/m^2$	relaxation time of particle
$\tau_f$	$N/m^2$	turbulence time scale
$\gamma$	$N/m^3$	specific weight of a fluid

---



---

$\varepsilon$	$m^2/s$	turbulence dissipation rate
$\bar{\varepsilon}$	$m^2/s$	depth-averaged turbulence dissipation rate
$\eta$		the dissipation length scale
$\delta$	$m$	theoretical wall level
$\delta_c$	$m$	critical height of anchor ice release
$\delta_1$	$m$	thickness of viscous sublayer
$\delta_b$	$m$	thickness of boundary layer
$\beta$		deposition efficiency
$\phi$		the latitude in degrees
$\Phi_R$		the short wave radiation at the bottom
$\Gamma_r$		source item
$\kappa$		von Karman constant, 0.4

---

## 1.1 General Description of Anchor Ice

It is well known that in rivers and lakes, water is cooled from above by heat exchange with colder air. When the water temperature drops below zero, the water becomes supercooled and frazil ice begins to form. According to the US Army Corps of Engineers Cold Regions Research and Engineering Laboratory (CRREL, 1997), frazil ice is defined as “*fine, small, needle-like structures or thin, flat, circular plates of ice suspended in water*”. It is believed that frazil ice is the origin of almost all the other forms of river ice. Frazil ice will grow and agglomerate into flocs that float to the surface to form frazil slush, flocs and eventually a stationary ice cover. It may also stick to underwater objects to form anchor ice.

In turbulent rivers, supercooled surface water can be transported to a considerable depth within the flow. Since active frazil particles are highly adhesive and readily stick to each other as well as the river bottom, given the right hydro-meteorological conditions, anchor ice can grow and thicken to form extensive blankets of ice on the river bed.

Anchor ice is a form of ice which attaches to the bed in a river, stream, or ocean (Kivisild, 1970). It has been observed in all types of rivers, ranging from shallow streams with steep slopes to deep rivers with mild slopes (Arden and Wigle, 1972; Tesaker, 1994; and Parkinson, 1984) and in nearly all countries where river ice is formed. Anchor ice is also known as ground ice and bottom ice, among other names. It is a phenomenon unique to cold water streams during the winter season. Usually when ice forms, it floats to the river surface because of its lower density. Anchor ice, however, is formed due to the supercooling of the water and the sticky particles tend to attach instead of float. Figure 1.1 shows an anchor ice bridge formed at Sundance Rapids, downstream of Limestone Generation station, on the Nelson River, Manitoba.

Anchor ice can grow by two mechanisms on the river bottom. One mechanism is by underwater nucleation. The other mechanism includes attachment of frazil ice to the river bottom or to the existing anchor ice and also the growth of ice crystals of existing anchor ice in the supercooled flow.

### **1.1.1 Anchor Ice Formed by Underwater Nucleation**

If supercooled water is transported to the bottom, ice may be nucleated on underwater objects to produce anchor ice. It was seen from previous field research (Ontario Hydro, 1970) that the ice coated an underwater wire smoothly and it was not in the form of distinct agglomerated ice crystals. More ice was formed on the upstream side of the wire where supercooled water was supplied. Also local growth in the form of buds was noted.

As the temperature of the water at the time of formation of the anchor ice shown was only a few hundredths of a degree below  $0^{\circ}\text{C}$ , which is well above the threshold temperature for heterogeneous nucleation of ice, one may use Michel's (1967) theory to explain the nucleation since the surface of the river should have a thin layer of highly supercooled water. If the large eddies present in the turbulence brought this highly supercooled water in contact with underwater objects, heterogeneous nucleation should occur. Once the primary ice was formed, further ice nucleation could take place over the primary ice. It is evident that the objects on which anchor ice nucleates need not be on the bottom, as long as they are submerged (Tsang, 1982).

### **1.1.2 Anchor Ice Formed by Frazil Adhesion**

In addition to underwater nucleation, anchor ice can also be formed by the attachment of frazil ice to underwater objects. Thus, in a turbulent flow, if parcels of supercooled water containing frazil ice are transported to the river bottom by turbulence, the frazil ice will possibly stick to objects on the bottom and form anchor ice. Field investigations by Ontario Hydro (1967, 1968, 1969, 1970) showed that this mechanism is of primary importance in the anchor ice formation process. The growth of anchor ice, therefore, can be approximated by the rate of deposition of frazil ice to the river bottom or to existing anchor ice, which is affected by the following four factors:

- i) the presence of frazil ice on the bottom of the channel;
- ii) adhesion of frazil ice crystals present at the bottom to the channel bed or to existing anchor ice;
- iii) the growth of frazil ice crystals forming anchor ice; and

- iv) detachment of anchor ice from the bottom.

A dramatic difference can be seen in the formation of anchor ice by the two different processes. The surface of the anchor ice formed by frazil adhesion is much coarser than that formed by underwater nucleation and has distinct frazil crystals that are stuck to each other. Both processes show that more anchor ice is formed on the upstream side of the wire (right side of the wire); this is mainly because the upstream faces the direction of supply of both frazil ice and supercooled water. Also, the relative velocity between the supercooled flow and the anchor ice is greater on the upstream side due to greater packing of streamlines on the upstream side than that on the downstream side (Tsang, 1982); so the heat exchange is also quicker on the upstream side.

In addition to the attachment of frazil ice, the growth of attached frazil ice crystals also plays an important role in the growth rate of anchor ice. It is observed in nature that the lower part of the anchor ice is composed of large ice platelets and the upper part is mainly made up of fine frazil crystals. Between these parts, there is a transitional crystal size zone. The change of the frazil crystal size from the top to the bottom of the anchor ice occurs because of the different degrees of accelerated growth of the frazil ice crystals. The earlier the frazil ice crystals stick to the bottom or to anchor ice, the longer time they reside in a higher relative velocity, and hence the longer time they have for accelerated growth.

### **1.1.3 Limitation on Thickness of Anchor Ice**

Once formed, anchor ice is subject to a buoyancy force because its density is less than that of water. The buoyancy force increases proportionally to the change in anchor ice thickness and density. In addition, the drag of the flow also tends to tear it away from its anchoring place. The bond between the anchor ice and the river bottom must resist the combined action of the buoyancy force and the drag forces, or the anchor ice will lift up.

There are several limitations on the thickness of anchor ice. First, the flow depth provides the upper limit to the anchor ice thickness, as some rivers with large bottom roughness can accumulate very thick anchor ice. Anchor ice “peeling” is the second factor limiting anchor ice thickness. The drag force of the flow will increase with the growth of anchor ice and if the bond between the anchor ice and the bottom material is not strong enough to resist the increasing drag force, eventually the anchor ice will be torn away from the bottom. For some rivers with heavy rocky bottoms, “peeling” is the predominant factor controlling anchor ice thickness. Third, for some rivers with coarse sandy bottoms, the buoyancy force plays a major role in limiting the thickness to which anchor ice can grow. In addition, following sunrise and the warming up of the water, the bond between the anchor ice and the river bottom can become weakened to the point that buoyancy alone is sufficient to float the anchor ice off the bottom; the release of anchor ice stops quickly as evening approaches.

### **1.1.4 Effects of Anchor Ice**

The formation of anchor ice can have serious physical as well as biological implications.

a) Flow rate

Anchor ice formation and growth on the river bed changes the boundary roughness and reduces the flow depth. For example, the flow rate in a channel connecting two reservoirs with constant water level can be severely reduced because of anchor ice formation. It is worth noting that anchor ice does not have to form everywhere to reduce the flow. A local growth can effectively choke off a large part of the discharge and huge financial losses could be incurred by a hydro-power industry dependent on the flow.

b) Sediment transport

Released, floating anchor ice carries sediment to the water surface. This sediment is ice-rafted along shore and offshore under the influence of prevailing winds where the melting ice drops its sediment in some other area. This rafting can cause a significant sand loss in a sediment-starved near-shore zone.

c) Physical implications

Anchor ice can cause significant discharge and water level changes, since it raises the effective bed elevation and alters the bed roughness. It can be a major cause of hydropower production losses in the winter. For example, Manitoba Hydro continues to experience significant losses on generation revenue due to anchor ice growth at Sundance Rapids, downstream of the Limestone Generating Station. At four kilometers downstream from the generating station, anchor ice forms on a shallow granite rock shelf, which initiates the formation of an ice bridge that covers 80-90% of the channel's width

and results in up to 1.5 meters of staging in the tailrace of the station (Girling and Groeneveld, 1999).

d) Biological implications

Anchor ice can also have serious effects on invertebrates and fish, since it can block the supply of oxygen into the sediments and dislodge fish eggs from spawning beds by scouring action during its release.

Anchor ice forms on the seafloor at water depths of up to 33 meters, and most significantly at water depths shallower than 15 meters. It forms wherever conditions are suitable, including on or around slow-moving or sessile organisms. Anchor ice can entrap sea urchins, sea-stars, worms, isopods, sea spiders, sponges, and other animals as well as algae, rocks, and sediment. Animals may remain alive surrounded by an ice prison, or become frozen and killed. When an anchor ice mass becomes buoyant, it lifts off the bottom carrying its entrapped organisms up to the sea ice ceiling. Some become a food source for animals and bacteria. Some get frozen into the sea ice ceiling or may rain back down to the bottom some distance from where they were floated up. Anchor ice also serves as a refuge from predators with its numerous small cracks, crevices, and caves.

## 1.2 Literature Review

There have been a number of theoretical, experimental and field studies conducted on anchor ice that have achieved significant results. This section briefly summarizes

existing anchor ice research works as they provide the fundamental principles and starting point for the present study.

### 1.2.1 Theoretical Models of Anchor Ice

a) Marcott and Robert (1986) developed an empirical simulation model for anchor ice based on their field observations and measurements. The growth of anchor ice was considered to be due to turbulent heat exchange between the supercooled river water and the bottom ice. The frazil attachment process, which has been suggested to be the most important process in the formation of anchor ice (Ashton, 1986) was neglected. The release of anchor ice was considered to occur either when the water temperature became positive or when the buoyancy force was large enough to lift it off the bottom. Their formulation for anchor ice release was empirical.

b) Tsang (1988) built a thickness growth model of anchor ice, considering that the growth rate of anchor ice is equal to the flux of frazil reaching the bottom after the effects of porosity, adhesion and entrapment have been taken into account. The anchor ice thickness  $h_a$  is given by

$$\frac{\partial h_a}{\partial t} = \frac{\beta}{1 - e_a} C_b u_* , \quad (1-1)$$

where  $\beta$  is a deposition coefficient describing the ability of the frazil crystals to adhere to and being trapped by the river bottom or the existing anchor ice;  $C_b$  is the concentration of frazil at the river bottom;  $e_a$  is the porosity of the existing anchor ice

and  $u_*$  is the shear velocity at the bottom. However, a description of frazil ice distribution and the coefficient  $\beta$  was not given formulaically in his model.

c) Wang and Shen (1991) developed a one-dimensional simulation model for coupled frazil and anchor ice evolution in rivers. Both heat exchange and frazil attachment processes were considered. However, the vertical mixing in the flow was not explicitly formulated, and the detailed mechanism of frazil attachment was not examined. Wang (1993) elaborated a model for growth, decay and detachment of anchor ice. In this model there is no description of frazil ice distribution. In addition, two critical velocities regarding the growth of anchor ice were discussed, but were not formulated theoretically.

d) Hammar and Shen (1994, 1996) proposed a theoretical model for frazil ice accumulation on rough channel beds. They used the customary logarithmic law with a displacement height for the velocity profile outside the roughness layer. Inside the roughness layer, an empirical formulation for the velocity profile derived for a uniform rod-like roughness was used. The rate of deposition of frazil on the roughness elements was considered to be dependent on the frazil ice concentration as well as the geometry and distribution of the roughness elements. But the heat exchange between the supercooled water and frazil ice is ignored. The diffusion equation for frazil ice in this model was written as

$$-w_b C(y) + v_T(y) \frac{dC(y)}{dy} = \beta(y) u(y) C(y), \quad (1-2)$$

where  $w_b$  is the rising velocity of frazil ice,  $C$  is the frazil ice concentration,  $\nu_T$  is the fluid eddy viscosity and  $u(y)$  is the velocity component in the  $x$  direction.

The removal of frazil ice by the roughness elements is represented by the sink term on the right hand side of equation (1-2). The solution of this equation gives the concentration profile inside the roughness layer and the rate of deposition of frazil ice per unit thickness of the roughness layer, which varies in the vertical direction.

### **1.2.2 Experimental Studies of Anchor Ice**

a) Kerr (1997) conducted a series of laboratory studies on anchor ice formation and growth on gravel channel beds. The study showed that in a supercooled turbulent flow anchor ice is formed from the accumulation of frazil ice on the bed. The initial location of anchor ice accumulation as well as the growth pattern of anchor ice varies with flow conditions. The growth of anchor ice generally consisted of an initial stage of localized frazil deposition, followed by a transition stage, then a final stage of continued uniform growth. Three types of anchor ice forms were observed during the initial stage of growth: tails, scales, and balls. During the transition stage, flattening or releasing of anchor ice occurred. If the anchor ice was not released during the transition state, an anchor ice blanket would form and grow in thickness at a steady rate with respect to the heat loss rate.

b) Doering et al. (2001) used a counter-rotating flume housed in a cold room to study the growth of anchor ice. The laboratory experiments were carried out with Froude numbers

ranging from 0.18 to 0.76 and air temperatures ranging from -10 to -15<sup>0</sup>C. Also a digital image processing system was used to monitor the growth rate of anchor ice. From their experiments, they observed that the growth rate of anchor ice and the density of anchor ice had a dependence on the Froude number. They also observed that the release of anchor ice was related to the Reynolds number. However, the resolution of the images used to measure growth rate was not sufficient to determine the geometry of the anchor ice formed, nor were they able to closely examine the boundary between the anchor ice and the bed material. Figure 1.2 shows one of the experimental images from Doering et al. (2001).

### **1.2.3 Field Studies**

a) Robert Newbury (1968) undertook field observation programs throughout the winter and summer of 1966 and 1967 to discover the characteristics and effects of ice phenomena on Nelson River. A general ice regime theory was developed based on flow conditions in the Nelson channel and the net heat transferred at the river surface. An observation of frazil ice deposition was also observed below the water surface in shallow sections on boulders and on the river bed.

b) Parkinson (1984) did a limited two-year survey program on Lake St. Louis, on the St. Lawrence River at Montreal to measure water levels and temperatures as well as to observe the formation, growth, and release of anchor ice. Meteorological conditions such as air temperature, wind speed and hours of sunshine were obtained from the Atmospheric Environment Service at nearby Dorval Airport and the discharge was

provided by Hydro-Quebec. By interpreting these data, the anchor ice effects were evaluated as a function of the field observations and atmospheric conditions; the final results showed that the water level is very sensitive to the formation or release of anchor ice. It was observed that:

- i) a rise in water level up to 0.5 to 0.6 m can occur over a period of 6 or 7 days due to anchor ice formation;
- ii) a drop in water level of 0.6 to 0.7 m can occur in 5 or 6 days due to anchor ice release;
- iii) daily rises and falls of up to 0.3 m can be caused by either anchor ice formation or release; and
- iv) the cumulative effect of anchor ice can increase a lake level up to 0.9 m above its open water level for the same discharge.

c) Terada and Hirayama (1999) conducted field measurements of anchor ice for four years on the Niuppu River, a tributary of the Tesio river in Hokkaido, Japan. The growth pattern of anchor ice was observed and experiments of the adhesive properties of frazil particles on different materials were conducted about 100 m downstream of the grid for anchor ice. They concluded the following:

- i) anchor ice was formed mainly by flowing frazil crystals;
- ii) anchor ice was observed when air temperature was below about  $-10^{\circ}\text{C}$ ;
- iii) when air temperature was low, the volume of anchor ice mass increased;
- iv) the critical condition for anchor ice formation depends on the Froude number and air temperature;

- v) the coarseness of the surface of submerged objects influences the occurrence of anchor ice; and
- vi) the flow patterns around an object have an important role for the occurrence and the growth of anchor ice.

### **1.3 Study Objectives**

Although anchor ice can have many significant effects, our knowledge of anchor ice processes is still quite limited. As such, the mechanisms of anchor ice formation and growth have not been widely explored. Many questions remain unanswered and much more study is needed.

Field observation and measurement of the formation and growth of anchor ice are quite difficult because of the severe weather conditions. Therefore, for the present study of anchor ice, experiments will be conducted and a theory will be developed to elucidate the mechanism of anchor ice formation and growth by frazil attachment. The thermal growth of anchor ice caused by heat exchange between ice and the flume bottom material is not considered in this study. Accordingly, the main objectives of this research are:

- 1. Undertake a laboratory-based investigation to elucidate frazil ice entrainment, attachment and the associated formation and growth of anchor ice.**
  - a) a counter-rotating flume will be used to conduct the experiments

- b) by analyzing the data from the experiments, the governing factors for the formation and growth of anchor ice will be determined.
- c) anchor ice density, rotation torque load, bed/ice surface roughness with the growth of anchor ice will also be explored

**2. Develop algorithms to analyze digital images of anchor ice to characterize anchor ice formation and growth.**

- a) two high definition Hitachi CCD cameras will be used to take images of the entrainment and attachment of frazil ice from different angles and to monitor the growth of anchor ice.
- b) a Matlab-based digital image processing program using morphological techniques will be developed to process the images and to analyze the growth rate of anchor ice.

**3. Develop a numerical model to predict the growth rate of anchor ice.**

- a) a mathematical model to predict the growth rate of anchor ice in different hydraulic and air temperature conditions will be developed. The model will consider both frazil ice attachment and heat transfer between the anchor ice and the supercooled water.
- b) The deposition coefficient of frazil ice on gravel beds will be determined by analyzing experimental results. The numerical results will also be further verified by experimental data to increase its practicability.



**Figure 1.1** Anchor ice bridge formed at Sundance Rapids downstream of Limestone Generation station.

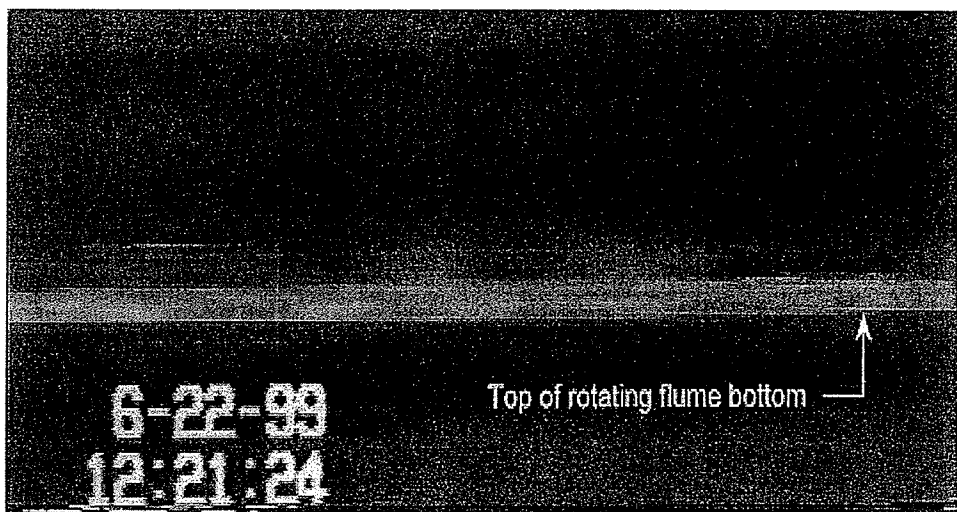


**Figure 1.2** Side view of anchor ice (Doering et al., 2001).

---

Laboratory experiments are more amenable than field tests to study anchor ice because of the ability to control the hydro-meteorological conditions in a lab. In addition, a long flume could be used to simulate the natural phenomenon, but would not be practical for such research because of the uneconomically long flume needed due to the nature of the formation and evolution of frazil and anchor ice. Therefore, a circular counter-rotating flume is used in the present study to overcome these problems.

## **2.1 Introduction of the Counter-rotating Flume**

The counter-rotating flume (Tsang 1992, Doering et al., 2001) used for the anchor ice experiments is shown in Figure 2.1. It is located in a cold room at the Hydraulics Research & Testing Facility, University of Manitoba. The counter-rotating flume is well-designed for studying frazil and anchor ice processes because its “infinite” length allows frazil ice crystals to form, grow as well as to agglomerate on the surface or attach to the river bottom to form anchor ice without being subjected to the stress of any recirculation mechanism.

The counter-rotating flume consists of two concentric cylinders mounted on a rotating frame, forming the inner and outer walls of the flume. The flume bed, which is supported by another frame, is able to rotate independently of, and in the opposite direction to, the flume walls. Figure 2.2 shows the schematics of the bed and wall rotating frames. The counter-rotating flume is 0.2 m wide (from the inside of the outer cylinder to the outside of the inner drum), 0.35 m deep and has a centerline diameter of 1.2 m. An air jacket below the base plates circulates warm air to simulate a geothermal heat flux from the bed. The air pocket is equipped with a heater and fan connected to a controller to maintain a constant temperature. The air temperature in this pocket is separated from the flume water by an insulator which consists of a 5 cm thick layer of UHMW (Ultra High Molecular Weight) plastic. In addition, in order to prevent the sidewalls of the flume from icing, warmed air is circulated in ducts surrounding the flume walls. The air spaces in the walls and under the bed-plates are held constant by a series of PID controllers. The temperature in the cavities was monitored during each experiment.

The cold room (Figure 2.3) housing the counter-rotating flume is a 4.3 m wide, 4.3 m deep and 2.7 m high chamber constructed of 4" thick Norbec insulated panels with an insulation-value of R30. It is equipped with two Blanchard Ness outdoor air-cooled condensing units, each with a capacity of 48,000 BTU's. Each condensing unit is coupled with a Blanchard Ness low silhouette evaporator coil via a Sporlan CDS-8 stepper motor evaporator control valve. The temperature of the cold room is regulated with an Omron E5GN temperature controller. The temperature can be adjusted between room temperature and -35°C and is held within  $\pm 0.1^\circ\text{C}$ .

## 2.2 Velocity Calibration of the Counter-rotating Flume

The counter rotation of the flume has the potential to induce a secondary circulation in the fluid due to centrifugal forces, therefore, the wall and bed rotation rates must be set to balance the shear forces on the water. The net result is that the water is stationary in an absolute frame of reference except in the thin boundary layers. However, in a frame of reference relative to the rotating bottom, the fluid has a velocity profile typical of a free surface flow over a bottom. The relative rates of the rotation required to achieve zero absolute velocity will, of course, depend on the boundary roughness, in particular, the bottom roughness. A series of detailed measurements of velocity distribution in the counter-rotating flume on different roughness beds were conducted using a conical hot film probe. (Clark and Doering, 2006). The present experiments were conducted using three different bottom roughness bedplates with mean gravel diameters of 0.34, 1 and 2 cm, as shown in Figure 2.4.

A Kent-Lea Probe was used to calibrate the bed and wall velocities of the counter-rotating flume for different bottom roughnesses and water depths as shown in Figure 2.5. The calibration procedure was carried out with the Kent Lea probe placed at 0.6 of the water depth. For a given bed speed, the wall speed was adjusted to match the angular velocity of the probe. In such a situation, the water would be stationary with respect to an observer in the cold room. Figures 2.6(a), (b) and (c) show the calibration curves for a water depth of 10 cm and bed roughnesses of 0.34, 1 and 2 cm, respectively. (Other calibration curve scenarios are given in Appendix B).

## 2.3 Data Acquisition Systems

### 2.3.1 Temperature Recording Equipment

A Fluke Blackstack thermometer with a resolution of  $0.0001^{\circ}\text{C}$  and an accuracy of  $\pm 0.001^{\circ}\text{C}$  was used in the present experiments (Figure 2.7). The temperature probe was inserted into the flow from the side to prevent any interaction between the water/air interface that would occur if the probe was submerged from the surface. It was about 6 cm from the side of the flume and 6 cm above the bed as shown in Figure 2.8.

### 2.3.2 Image Recording Equipment

A 250 W and a 400 W metal halide bulb with an output of 20,000 and 40,000 lumens, respectively, located inside the inner drum (opposite to the cameras) were used in the experiments. The metal halide bulbs are regulated by electronic ballasts to provide a steady output, which guarantee the level and color of illumination provided. Cross-polarized light conditions were used to obtain accurate ice images as shown in Figure 2.9. (Morris, 2002). A polarizing sheet (polarizer 1) is attached to the inner flume wall cavity. Each camera lens is fitted with a polarizer (polarizer 2) which is positioned so that the optic sills are perpendicular to the optic sills of the polarizing sheet. The polarizing sheet filters light oscillations perpendicular to its optic sills while the polarizers on the lenses filters the light in the other principle direction, preventing any light entering the camera directly from the light source. The only way for light to enter the camera is by passing through a particle of ice, which allows the normally transparent ice crystal to be seen distinctly by the camera, by changing the orientation of the original polarizer.

Two Hitachi KP-F100A CCD cameras with a resolution of 1300×1024, located in a heated cavity in the side of the flume, were used to take images. The Hitachi cameras have a larger CCD element, which when combined with the source of illumination permits shutter speeds up to 1/10,000 s. The two cameras were set to take images from different angles to observe the evolution of anchor ice on the flume bottom as shown in Figure 2.10.

A pair of Data Translation DT-3162 frame-grabber boards external triggered by a Visual Basic program were used to control the cameras. The frame-grabber boards were housed in a 1.8 GHz Pentium 4 computer. The system can allow up to 2M pixel images as well as simultaneous acquisition of images from multiple cameras.

### **2.3.3 Torque Load Measurement Equipment**

The independently rotating bed and wall frames were driven by a pair of Compumotor Gemini GV6 servo motor controller systems with encoder feedback, which could return the bed and wall torque load signals in a percentage of a full-scale torque load. The motors were located in two insulated boxes mounted on the counter-rotating frames in the cold room. The temperatures in the insulated boxes were kept constant at around 12°C during the tests. The Gemini GV6 is a controller/drive that has basic motion control and sequencing capabilities and can be used in distributed control applications. For the present tests, the GV6 was configured and programmed to return the torque load signals over a RS232 cable. An application program was developed using Labview to collect the torque loads returned from the GV6 controller/drive.

## **2.4 Digital Image Processing**

The digital images of anchor ice collected are gray scale TIFF (Tagged Image File Format) images with a resolution of 1300 by 1024 pixels. Each image is a  $1300 \times 1024$  matrix with an entry value ranging from 0 to 255, in which 0 represents black, 255 represents white and all numbers in between are shades of gray (higher numbers are brighter). All image analysis algorithms were developed using Matlab Release 13 equipped with the image and signal processing toolboxes. The algorithms have been developed to characterize the anchor ice so as to determine the growth of anchor ice on the gravel beds. The procedure of the digital image processing is introduced hereinafter.

### **2.4.1 Removal of the Background Lights**

A series of reference images were taken before collecting ice images. Herein, a reference image means an image taken prior to any anchor ice formation and an ice image refers to an image that contains anchor ice. Only one reference image was used for the background light subtraction because of the consistent lighting conditions despite the multiple reference images taken in each experiment.

Inside a reference image, there are brighter spots, which may be misinterpreted as ice particles as shown in Figure 2.11(a). A step is taken to remove the background lights by subtracting the brighter spots from the ice images so that anchor ice can be accurately defined. Since each image is a matrix, removing the brighter spots from the ice image is

actually a process of matrix subtraction. Figure 2.11(b) shows an anchor ice image after the subtraction process.

## 2.4.2 Morphological Operations

The images created after the removal of background ‘noise’ were transferred into binary images by using edge detection techniques with a ‘Canny’ estimator. The edge function is used to detect edges, which are places in an image that correspond to object boundaries. In order to find edges, this intrinsic Matlab function looks for places in the image where the gray scale intensity changes rapidly, using one of two criteria:

- i) places where the first derivative of the intensity is larger in magnitude than some threshold; and
- ii) places where the second derivative of the intensity has a zero crossing.

The ‘Canny’ method is a powerful edge-detection method. It differs from other edge-detection methods in that it uses two different thresholds to detect strong and weak edges, and includes the weak edges in the output only if they are connected to strong edges. This method is, therefore, less likely than others to be fooled by noise, and more likely to detect true weak edges.

The binary images formed by the edge function were processed further by the ‘imclose’ function. This closing procedure is actually a dilation operation followed by the erosion operation, both using the same structuring elements. The closing function immediately followed by a function called ‘imopen’, which erodes an image and then dilates the

eroded image using the same structuring element for both operations. The function 'bwareaopen' is also used to remove all connected components (objects) that have fewer than P pixels from the binary image and then produce another binary image (Doering, 2003).

Once the binary images of anchor ice were determined after the morphological image processing techniques, the thickness of anchor ice could then be calculated in units of pixels from the binary images. The white anchor ice part in the binary image is composed of elements of '1' while the black part is composed of elements of '0'. Figures 2.12 (a), (b) and (c) show the original anchor ice images and their corresponding binary images at different developing periods of anchor ice growth. The white line shown in the original images is the actual perimeter of the corresponding binary images and it is used to show how well the binary images locate the anchor ice edges; clearly, the agreement is very good.

### **2.4.3 Pixel Calibration and Conversion**

In order to get the thickness of anchor ice in units of length, the units of a pixel in each image has to be calibrated into units of length. The size of a particle in pixels can be converted to length by knowing the length of one pixel. The size of a pixel on the digital image depends on the position and the focal length of the camera lens, therefore, it is necessary to measure the size that each pixel represents in an image in order to convert the size of an object into the units we want. This is accomplished by taking a picture of a ruler placed in the middle of the flume; the size of a pixel can be determined by

measuring the number of pixels along a certain length on the ruler. Figures 2.13(a), (b) and (c) show the images of a ruler used to determine the pixel length for different gravel bed roughness conditions. The position and lens configuration of the two cameras were different for different gravel bed roughness. The conversions for the different bed roughnesses are listed in table 2.1.

**Table 2.1.** The conversion equations

<b>Roughness height</b>	<b>Conversion equations</b>
0.34 cm	1 pixel = 0.01096 cm
1 cm	1 pixel = 0.01172 cm
2 cm	1 pixel = 0.01307 cm

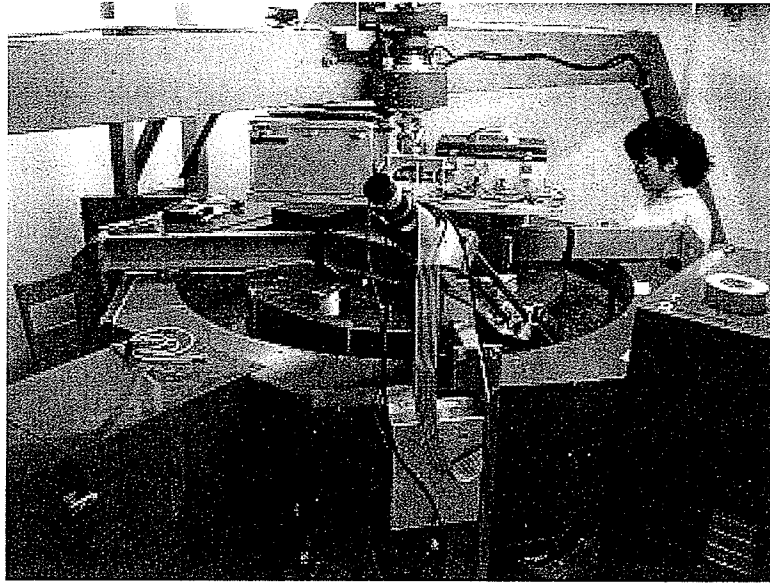


**Figure 2.1** The counter-rotating flume.

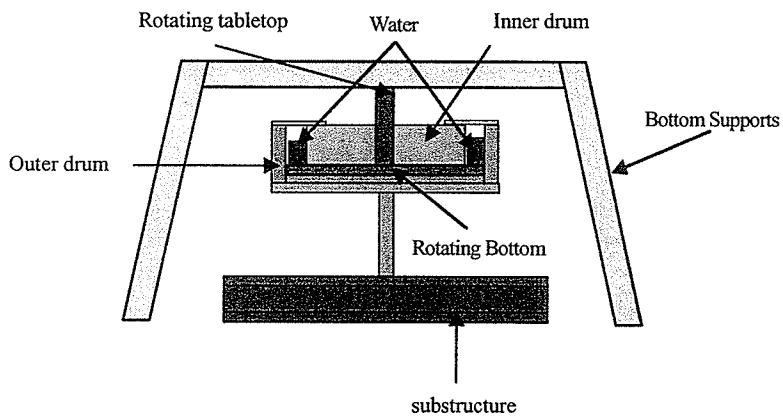


**Figure 2.2** Schematics of the structural component of the counter-rotating frames.

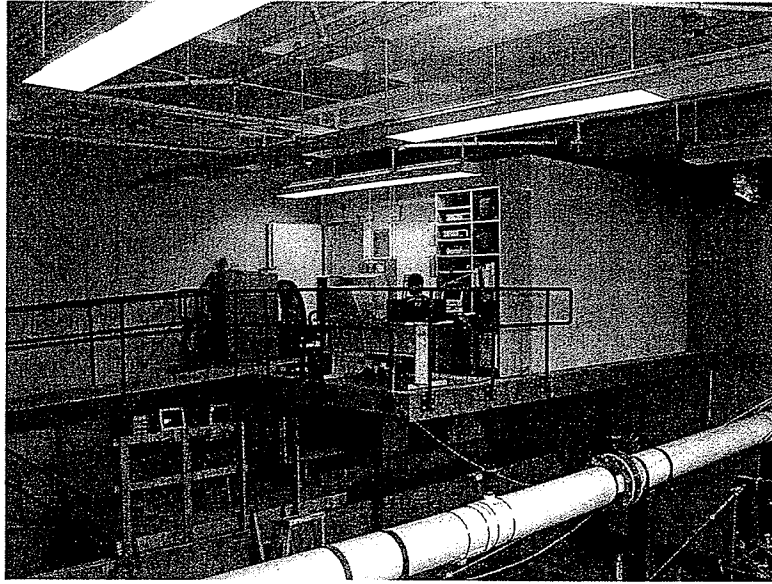


**Figure 2.3** The cold room.

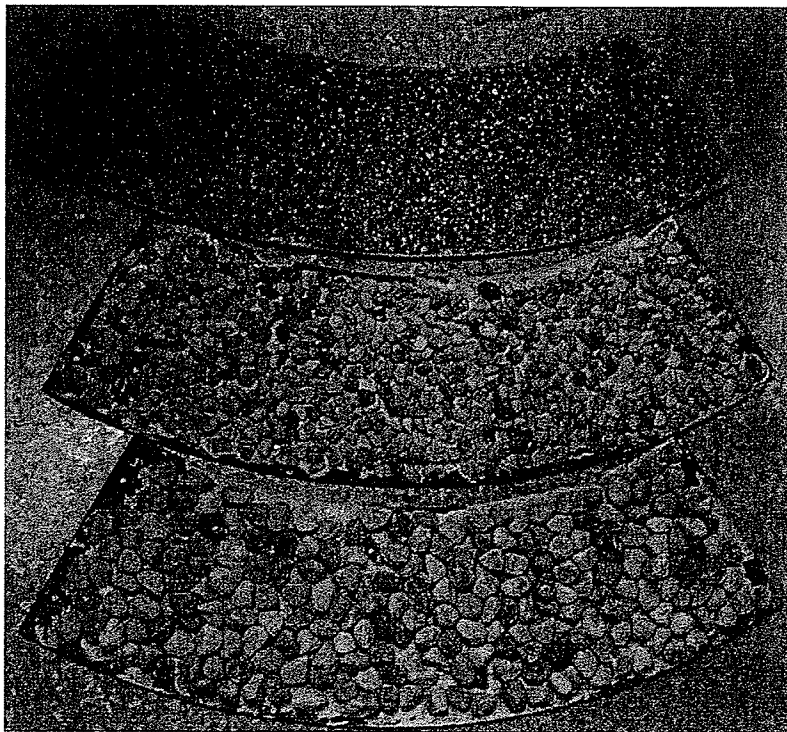


**Figure 2.4** Three bedplates with different sizes of gravel 0.34, 1 and 2 cm.

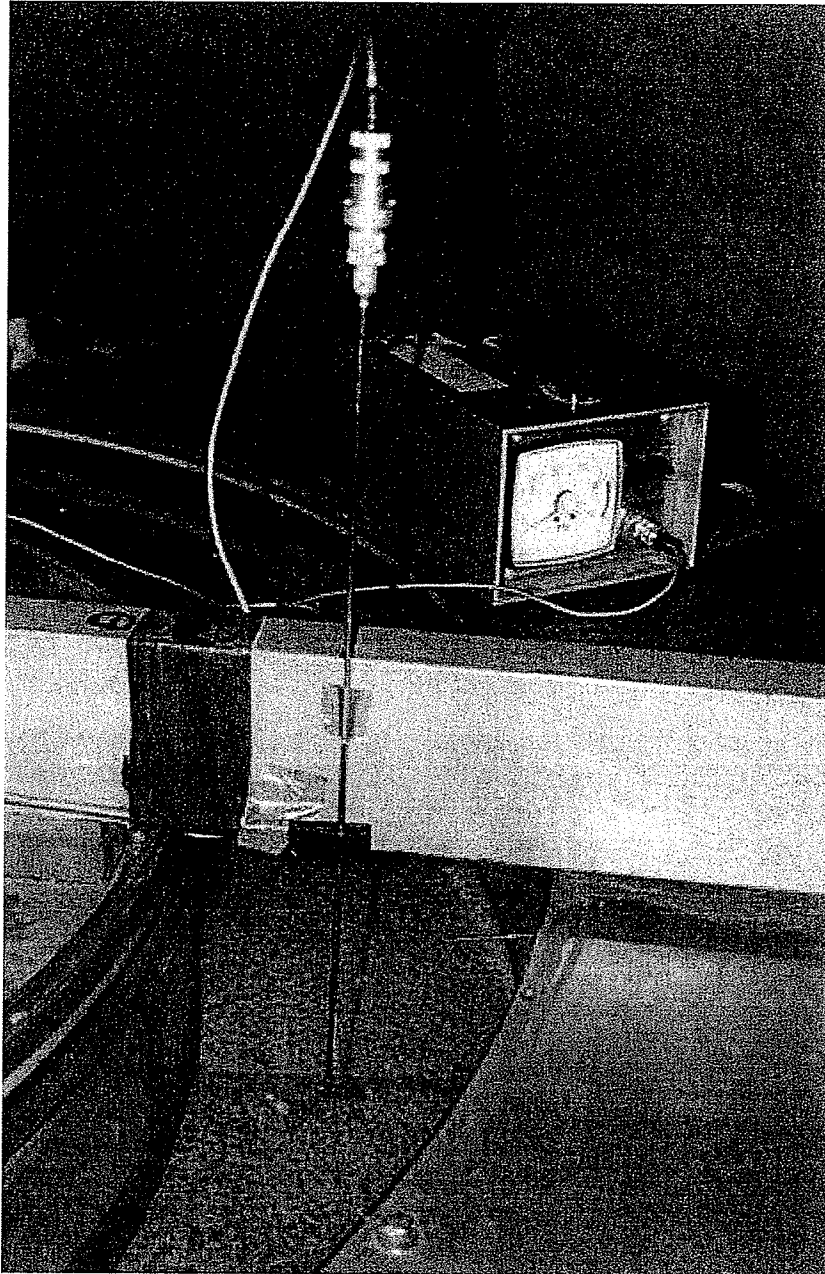


**Figure 2.5** Kent-Lea probe used in the velocity calibration of the counter-rotating flume.

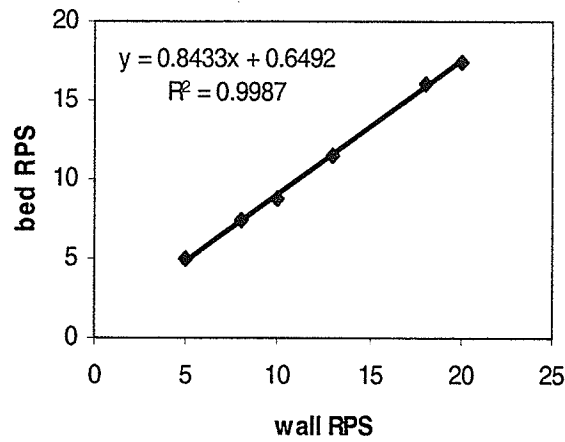


**Figure 2.6(a)** The calibration curve when bed roughness is 0.34 cm and water depth is 10 cm.

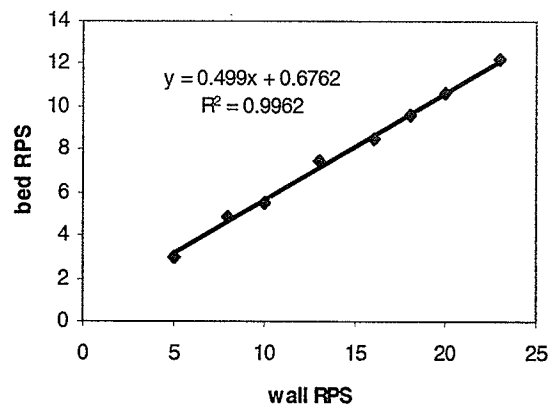


**Figure 2.6(b)** The calibration curves when bed roughness is 1cm and water depth is 10 cm.

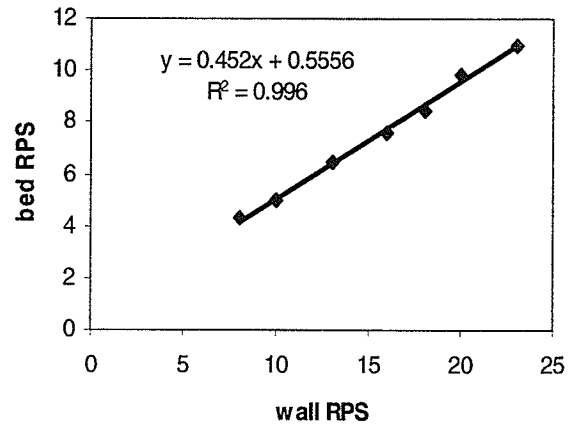


**Figure 2.6(c)** The calibration curve when bed roughness is 2cm and water depth is 10 cm.

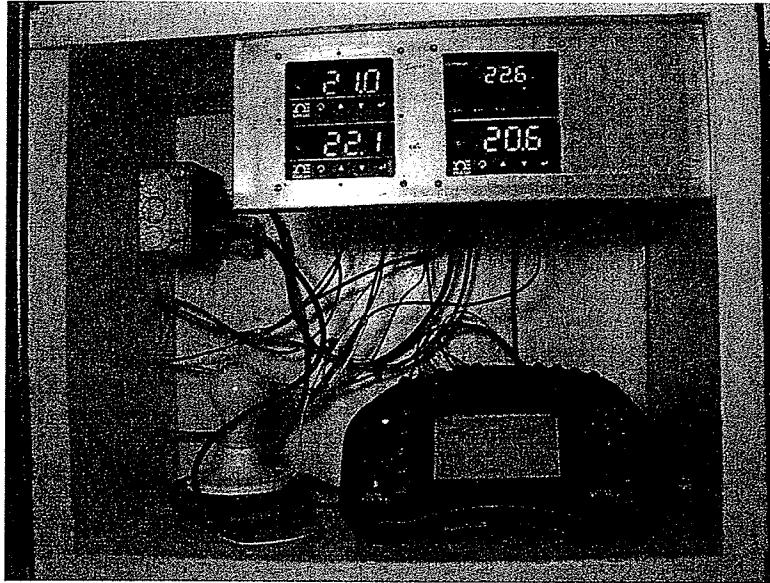


**Figure 2.7** The Fluke BlackStack thermometer (at lower right hand corner).

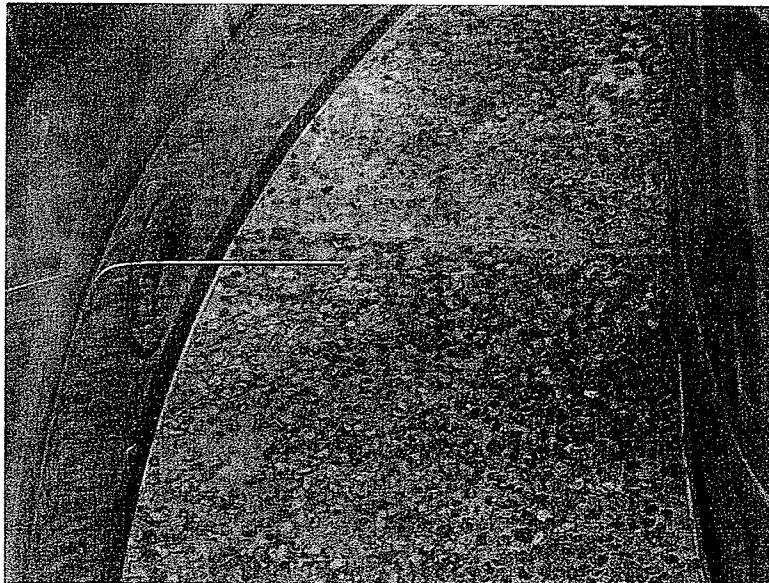


**Figure 2.8** The thermometer probe.

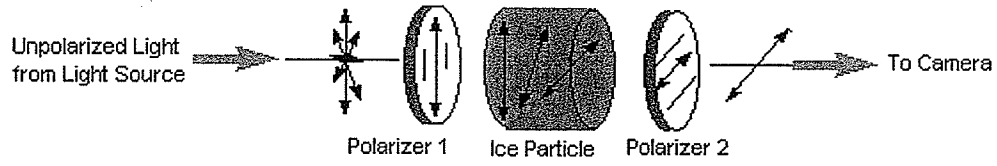


Figure 2.9 Cross polarized light scheme (Morris, 2002).

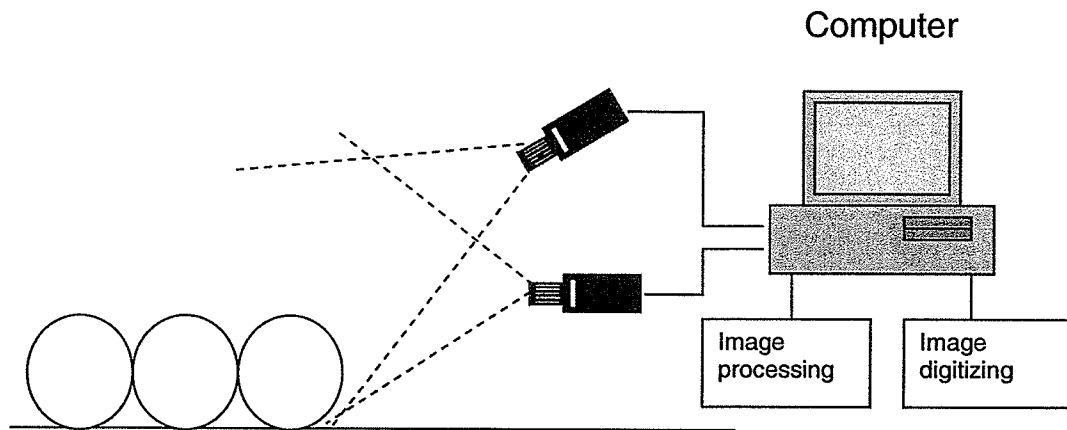
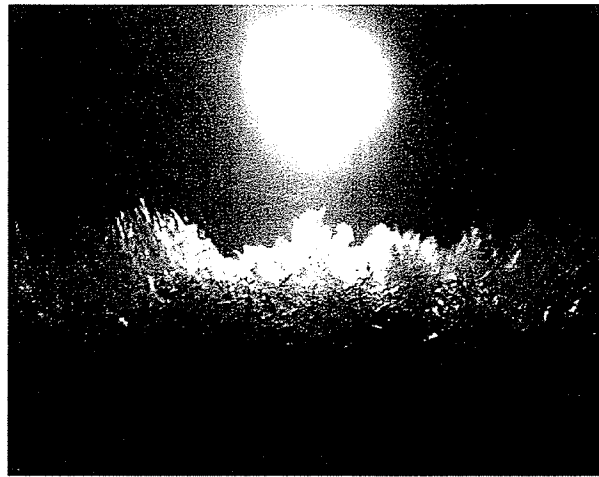
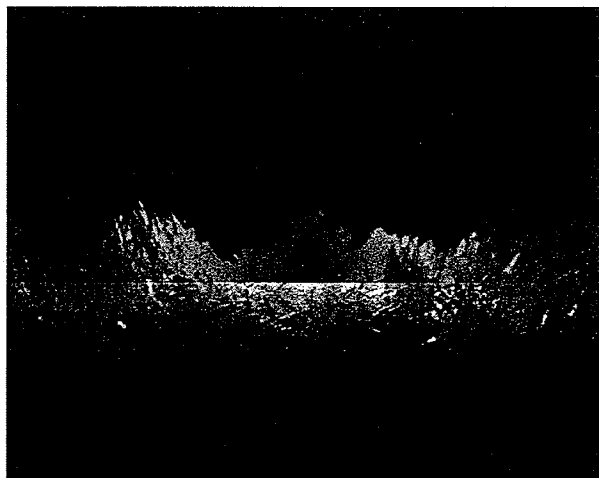


Figure 2.10 A sketch of the position of the two cameras.

(a)



(b)



**Figure 2.11** Anchor ice image before (a) and after (b) the subtraction of the reference image.

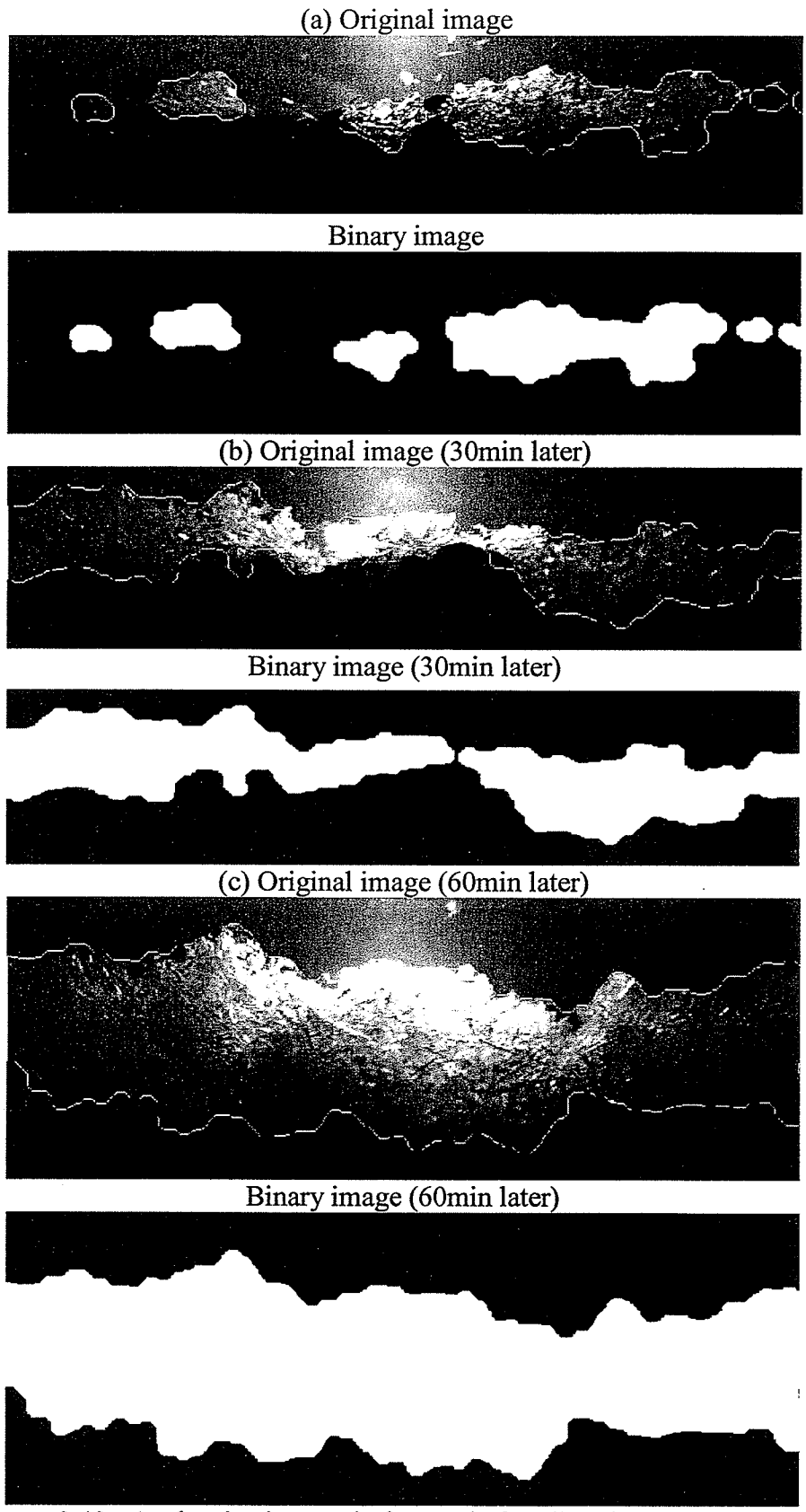
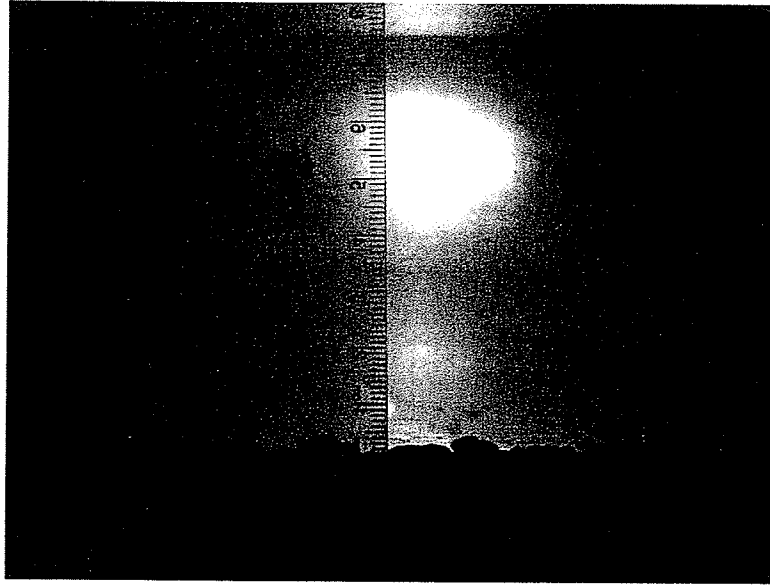
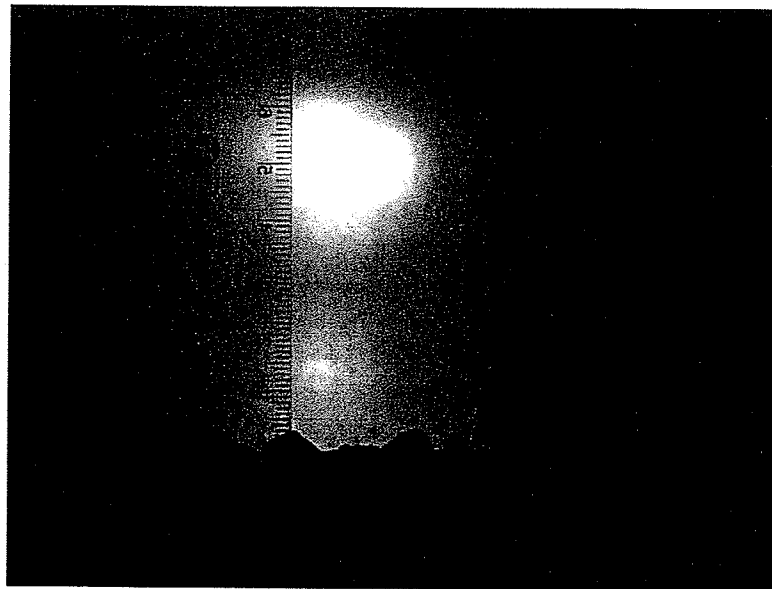


Figure 2.12. Anchor ice images before and after digital image processing.



**Figure 2.13(a)** Conversion image when the roughness height is 0.34 cm.



**Figure 2.13(b)** Conversion image when the roughness is 1 cm.

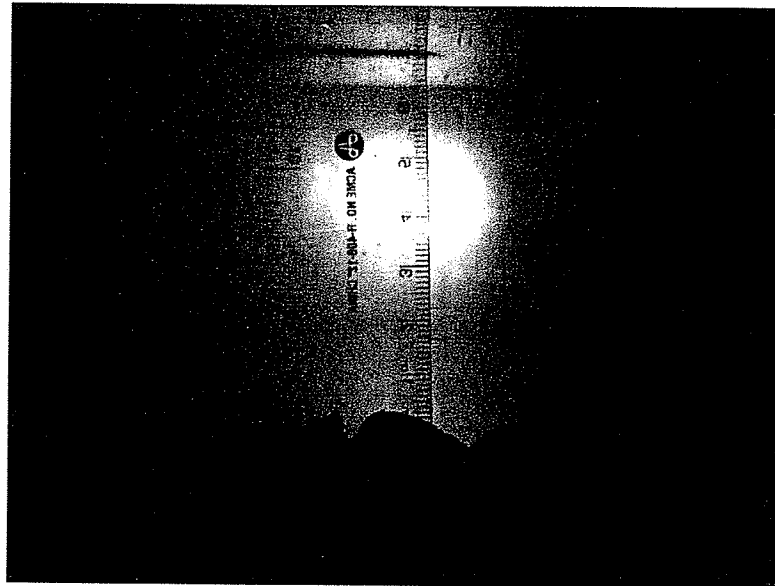


**Figure 2.13(c)** Conversion image when the roughness is 2 cm.

## *An Experimental Study of Anchor Ice Evolution Around Rocks and on Gravel Beds*

---

### **3.1 Introduction**

As previously mentioned, active frazil ice particles are highly adhesive and will easily stick to gravel and many other materials to form anchor ice. Experiments of anchor ice evolution around different arrangement of rocks and on gravel beds under different hydro-meteorological conditions were conducted. During these experiments, a detailed observation of frazil ice deposition and anchor ice evolution was carried out with a view to a better understanding of the mechanism of anchor ice growth.

### **3.2 Evolution of Anchor Ice around Rocks**

Different arrangements of rocks (diameter of 4 cm) were set on the flume bed for the purpose of studying the growth mechanism of anchor ice around rocks. Anchor ice appears to initiate from frazil ice attachment for all the tests as shown in Figure 3.1(a)-(d). When the water temperature drops below zero and the water becomes supercooled,

frazil ice starts to form. Throughout the supercooling process, more and more frazil ice particles are formed. It was found that during the peak amount of frazil ice formation, anchor ice appears in certain positions around the rocks and grows quickly.

Before each test, the cold room temperature was lowered to a specified value and the counter-rotating flume was started when the air temperature dropped below  $1^{\circ}\text{C}$ . The rotation rates of the bed and wall of the flume were set to the designed velocities, which were calibrated beforehand to achieve zero absolute velocity of the water. The two Hitachi cameras were set to take ten images every two minutes during the tests so that the complete growth process of anchor ice could be monitored in detail. The rotation rates and cold room temperature were maintained constant throughout the whole experimental process by the array of computer-based controllers described in chapter 2. Table 3.1 summarizes the experimental parameters of anchor ice evolution around the different arrangements of rocks.

**Table 3.1** Experimental parameters of anchor ice evolution around rocks.

Test Date.	$V$ [m/s]	$H$ [m]	$k_s$ [m]	$A_t$ [ $^{\circ}\text{C}$ ]	$F_r$	$R_e$
01/01/2005	0.38	0.1	0.01	-15 $^{\circ}\text{C}$	0.38	42200
01/08/2005	0.38	0.12	0.01	-15 $^{\circ}\text{C}$	0.35	46000
01/10/2005	0.38	0.12	0.01	-10 $^{\circ}\text{C}$	0.35	46000
01/15/2005	0.38	0.12	0.01	-20 $^{\circ}\text{C}$	0.35	46000
01/28/2005	0.38	0.1	0.01	-20 $^{\circ}\text{C}$	0.38	42200
01/31/2005	0.38	0.1	0.01	-15 $^{\circ}\text{C}$	0.38	42200
02/15/2005	0.38	0.1	0.01	-15 $^{\circ}\text{C}$	0.38	42200
02/16/2005	0.38	0.1	0.01	-10 $^{\circ}\text{C}$	0.38	42200
02/17/2005	0.38	0.1	0.01	-20 $^{\circ}\text{C}$	0.38	42200
02/18/2005	0.57	0.1	0.01	-15 $^{\circ}\text{C}$	0.57	63300

### 3.2.1 Evolution of Anchor Ice Around One Rock

Although the main focus of these experiments is to study the mechanism of anchor ice growth on gravel beds, the simplest case of anchor ice evolution around a single rock was considered first to look at the attachment pattern of frazil ice around a rock. Then additional rocks were added in the flow direction or across the flow direction and the evolution forms of anchor ice around different arrangements of rocks were monitored.

Starting with a single rock, it was observed that there are two locations around a rock where frazil ice starts accumulating. One is the front-face gap between the rock and flume bed and the other is the back-side gap. Frazil ice particles are entrained in a turbulent flow and some of them get trapped in the front or back-side gaps and then accumulate gradually. It was found that frazil ice accumulates faster in the front-face gap than in the back-side gap, and that it barely grows at the left and right sides of the rock. Once frazil ice attachment initiates (i.e., anchor ice growth begins) it grows upward towards the free surface and extends in the upstream (front-face) and downstream (back-side) direction. Eventually with further frazil ice accumulation and thermal growth, the two pieces of anchor ice will climb up the rock from both the front and back sides and join each other to cover the top of the rock. When the anchor ice growth protrudes above the rock, it is flattened in the direction of flow by hydrodynamic drag forces. Figures 3.2(a) – (f) show the complete process of anchor ice growth around a single rock when the velocity is 0.38 m/s, the water depth is 10 cm and the air temperature is -16°C. Figure 3.2(g) shows a sketch of the sequence of anchor ice development around this rock.

Note that the raw images are shown for clarity. The entrained frazil ice can be clearly seen in the flow.

Frazil ice attachment on top of the rock was also observed. Apparently the bonding force between these small anchor ice pieces and the gravel surface was too weak to resist the drag and lift forces of the flow and the small pieces of anchor ice were dragged away almost immediately by the flow. This phenomenon can be well observed from Figures 3.2(c) and (d).

Three air temperatures  $-10^{\circ}\text{C}$ ,  $-15^{\circ}\text{C}$ ,  $-20^{\circ}\text{C}$  were used in the tests and the evolution of anchor ice during different time periods under different air temperatures are shown in figures 3.3, 3.4 and 3.5. It can be seen that under the highest air temperature  $-12^{\circ}\text{C}$ , there were almost no anchor ice formed in the first 20 minutes of the test. While when the air temperature was  $-20^{\circ}\text{C}$ , there was an obvious amount of anchor ice formed around the rock. After two hours into the tests, for air temperature  $-12^{\circ}\text{C}$ , there was only a tiny amount of anchor ice formed around the corner of the rock. But for an air temperature  $-20^{\circ}\text{C}$ , the anchor ice had almost grown ovetop of the rock. As observed from experiments, air temperature has a significant effect on the evolution of anchor ice.

### **3.2.2 Evolution of Anchor Ice on a Row of Rocks**

After the experiments of anchor ice evolution around a single rock, additional rocks were added 2 cm apart to observe the evolution form of anchor ice around a row of rocks along the axis of the flume. Anchor ice first initiates in the front-face gap between the front

rock and the flume bed. Almost simultaneously it starts accumulating in the other four front-face gaps as well. Back-side accumulation is also observed, but it is not as significant as the front-face accumulation. With the production of large amounts of frazil ice particles during the supercooling process, anchor ice accumulates and fills in the gaps between the rocks quickly. Once the anchor ice grows over the tops of the rocks, they are flattened by the drag force of the flow as they continue to accumulate. With continued accumulation, anchor ice accumulates toward and eventually connects with adjacent ice to form a narrow layer of anchor ice. Figures 3.6(a) – (f) show the growth process of anchor ice for this case and Figure 3.6(g) shows a sketch of the sequence of anchor ice development around these five rocks. No obvious side growth was detected during these tests. A plan view of the accumulated anchor ice on these rocks is shown in Figure 3.7; note that this top view was obtained without polarized light making the low density anchor ice difficult to detect.

### **3.2.3 Evolution of Anchor Ice on Six Rocks in Two Rows**

Rocks were added across the flow direction after the tests of anchor ice evolution on a row of rocks to study the evolution form of anchor ice from both across the flow direction and along the flow direction. Six rocks (not contacting each other) were placed in two rows 3 cm apart across the flow direction. The growth mechanism of anchor ice on the two rows of rocks is basically the same as that of on the five rocks described above. Anchor ice starts accumulating mostly in the front-face gaps with a little in the back-side gaps. But since the rocks are arranged side by side across the flow direction, anchor ice also grows sideways around the rocks because of the effect of the flow around the

neighbouring rocks. As the process continues, back-side anchor ice on the front row connects with the front-face anchor ice on the second row and continuously grows upward and sideward. Gradually, all anchor ice located around the rocks connects with each other and form a solid anchor ice mesh around the rocks. As the anchor ice mesh grows, flattening and releasing happens because of the hydro-dynamic forces due to the flow. Eventually a complete anchor ice blanket is formed to cover the rocks. Figures 3.8(a) – (d) show the growth process of anchor ice on these six rocks; the plan view is shown in Figure 3.9.

### **3.3 Evolution of Anchor Ice on Gravel Beds**

Eventually experiments of anchor ice evolution on uniformed gravel beds were carried out. The preparation of the experiments was basically the same as introduced in Section 3.2. Once the water became supercooled, measurement of water temperature and the collection of anchor ice images were started. The forms of anchor ice observed in the present tests, when considering the effect of the Froude number, agree with Kerr et al.'s experimental results (Kerr et al., 2002). Froude numbers used in the tests ranged from 0.22 to 0.64. Froude numbers lower than 0.22 were tried, but because of the small associated velocities, the flow did not generate enough turbulence so surface ice formed first and there was barely any or no anchor ice formation.

#### **3.3.1 Scale Type of Anchor Ice**

Just as Kerr et al. (2002) noted in his experiments, when the Froude number is between 0.22 and 0.50, a scale type of anchor ice is observed after the initial frazil attachment.

Frazil ice first gets entrained in the gaps between the gravel and starts accumulating along the front face of the gravel. With increasing frazil ice production associated with additional supercooling, anchor ice grows quickly upward toward the free surface. When it protrudes above the crown of the gravel, it grows toward the downstream direction in a tail like shape due to the hydrodynamic drag of the flow. The short tail of this anchor ice growth is frequently broken off by the flow, which prevents the formation of long tails. This form of anchor ice is denoted by Kerr et al. (2002) as scales, as shown in Figure 3.10(a) – (d). Figure 3.10(e) shows a sketch of the development of scale type anchor ice. In addition to the growth in length, the scale shaped anchor ice also grows in width and thickness and eventually all the scale shaped anchor ice pieces join together to form a thin layer of anchor ice.

### **3.3.2 Ball Type of Anchor Ice**

When the Froude number is greater than 0.5, frazil ice accumulates on gravel beds in almost round lumps and it is called ball shaped anchor ice (Kerr et al., 2002). The ball shaped anchor ice grows not only in the downstream direction but also in the upstream direction. After it overgrows the gravel, it spreads over the top of the gravel and gradually connects with other anchor ice pieces to form a thin blanket of anchor ice. Figures 3.11(a) - (d) show the growth process of ball shaped anchor ice in the present tests while Figure 3.11(e) shows a sketch of the development of ball shaped anchor ice.

### **3.4 Release of Anchor Ice on Gravel Bed**

Three sets of bed plates, each with different roughness, were used in the tests as mentioned before and the effect of bed roughness on the release of anchor ice was observed and described hereinafter.

Test results reveal that the gravel roughness height does not have a significant effect on the growth forms of anchor ice, but that it does have an obvious effect on the release of anchor ice. It was found in experiments that when the gravel size is small (diameter of bed gravel is about 0.34 cm in the test), anchor ice is more easily dislodged by the flow than when the gravel roughness height is big (diameter of bed gravel is about 2 cm). It appears that when the roughness height is small, the bonding force between the anchor ice and the small sized bed gravel is not strong enough to hold the anchor ice to the bottom. Therefore, small pieces of anchor ice are frequently dragged away by the hydrodynamic action and big pieces of anchor ice are usually lifted up by the buoyant force. Figures 3.12(a) – (d) show the release process of an anchor ice blanket by the buoyant force during a test. Figure 3.13 shows a digital picture of anchor ice releasing and Figure 3.14 shows the floating anchor ice slush after the release.

### **3.5 In-situ Thermo Growth**

Thermal growth of the accumulated frazil ice was also observed in the present tests. According to the temperature curves recorded in the tests, a thermodynamic process exists and is explained as follows. When frazil ice forms and grows, it releases the latent heat of fusion. At first, the released heat is not sufficient to compensate for the heat loss from the water to the surrounding air due to the small number of ice particles formed.

Therefore, the water temperature continues to decrease. At the point where the latent heat of fusion is equal to the rate of heat loss to the air, the water no longer has a net heat loss and it reaches its minimum temperature. Large quantities of frazil ice form and grow quickly during this period and then because of the increase in the latent heat from the frazil ice growth, the water temperature slowly begins to increase, which defines the point of the minimum temperature. Figure 3.15 shows the schematic heat balance in a water body. For a unit volume of water the heat balance can be conceptualized as

$$Q_{aw} = Q_i \pm Q_w, \quad (3-1)$$

where  $Q_{aw}$  is heat exchange between cold air and water,  $Q_i$  is heat release due to ice formation,  $Q_w$  is heat exchange (release or absorption) due to water temperature variation.

During each peak of frazil ice formation, some particles collide with each other and agglomerate to form large flocs; some flocs float to the surface while others remain entrained and attach to the flume bottom to form anchor ice. Surface frazil was regularly skimmed off in order to keep the water surface clear of surface ice and slush, so that the heat transfer process between water and the cold air could continue. Each time the surface ice slush was skimmed out, there was not enough frazil ice in the flume to release heat to attain equilibrium, so the water temperature dropped and then with the production of more frazil ice, the water temperature increased again as shown in Figure 3.16. (For more temperature curves, see Appendix C). With the steady growth of anchor ice on the bottom, two hours after the beginning of the experiment, there was hardly any frazil ice visible in the water while the water temperature was almost constant. This is believed to

be due to the latent heat released from the accumulated anchor ice compensating for the heat loss from the flume water to the surrounding cold air until eventually a new dynamic equilibrium of heat transfer was reached. The heat transfer between the water and the overlying cold air was equal to the latent heat of fusion from the frazil ice that leads to the anchor ice. It is believed from these tests that in-situ thermal growth of anchor ice does exist, though it is hard to observe in the digital images.

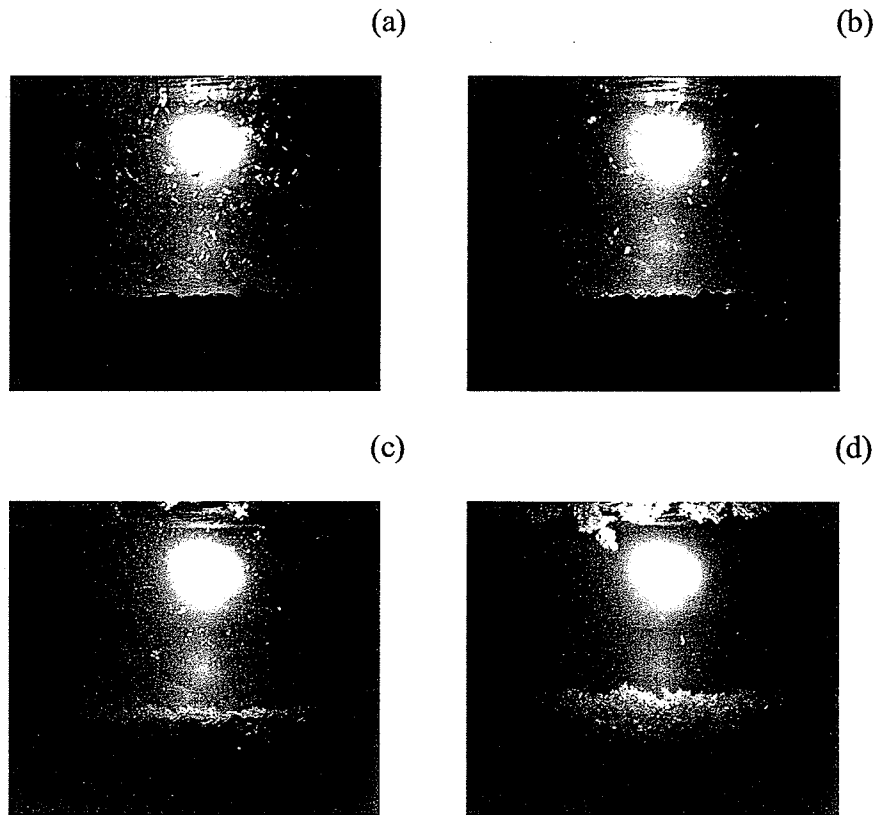


**Figure 3.1** (a)-(d) Attachment of frazil ice to the gravel bottom.

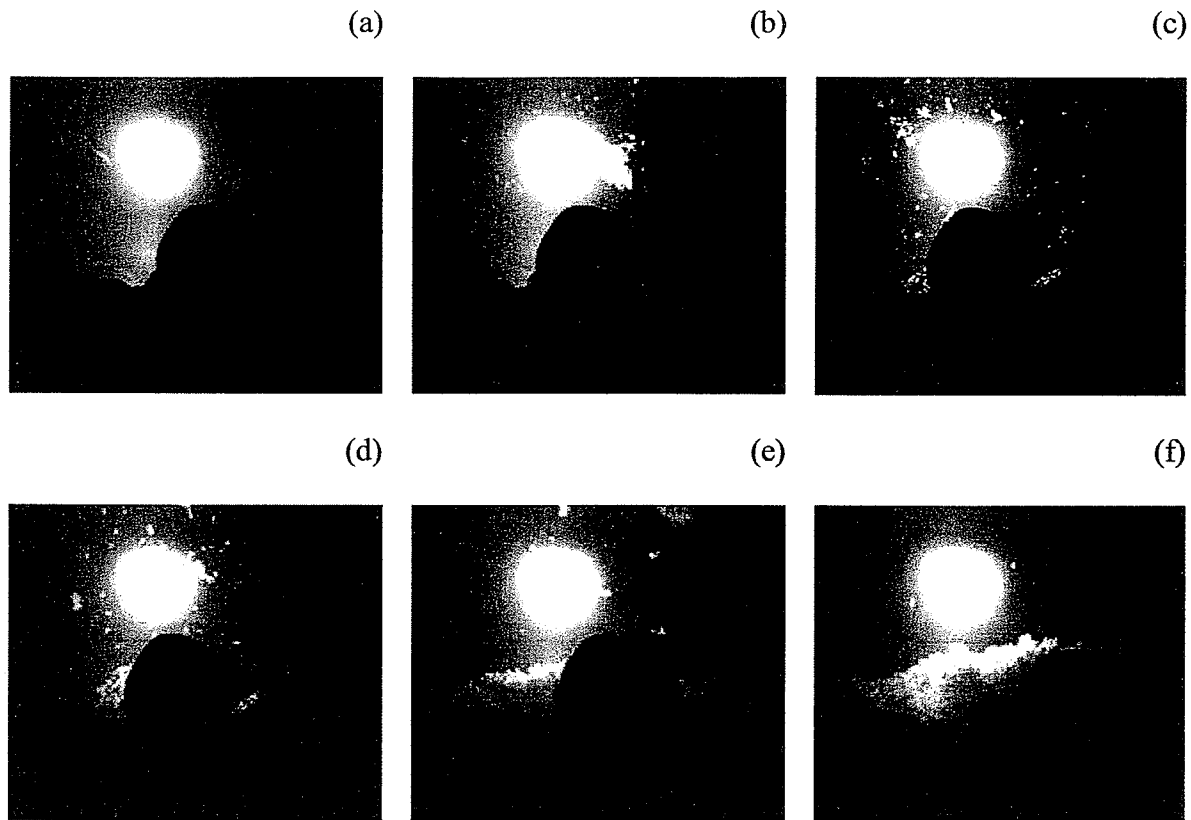


**Figure 3.2(a) - (f)** Anchor ice evolution around one rock when the bed velocity is 0.38 m/s, water depth is 10 cm and the air temperature is  $-16^{\circ}\text{C}$ .

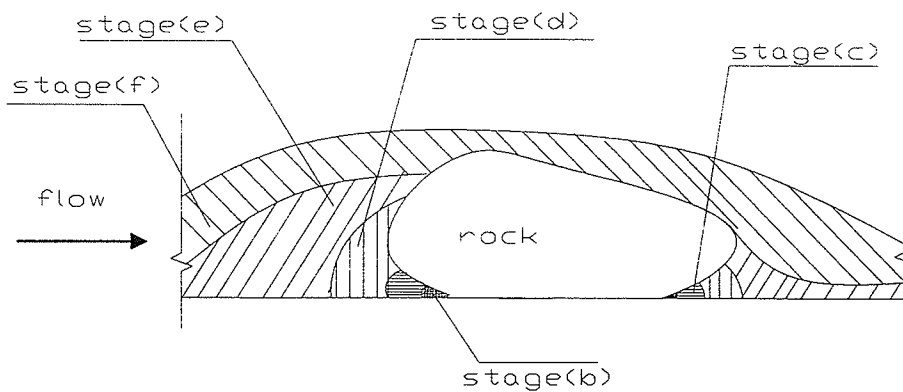


**Figure 3.2(g)** A sketch of the sequence of anchor ice development around one rock.

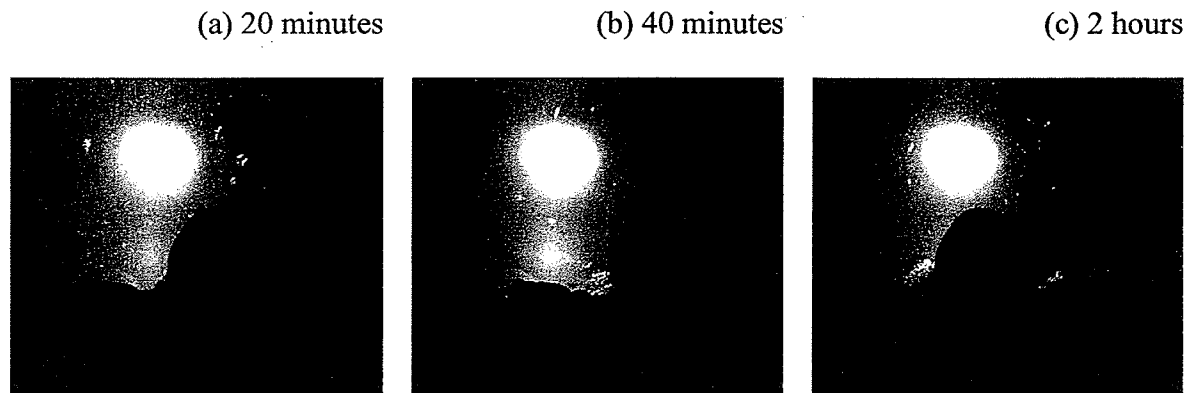


**Figure 3.3(a)-(c)** Anchor ice growth when the air temperature is  $-12^{\circ}\text{C}$ .

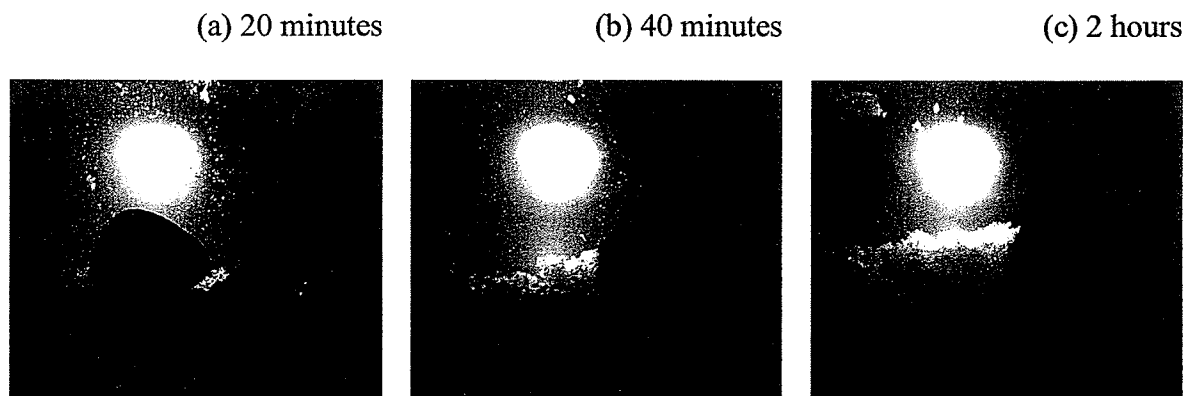


**Figure 3.4(a)-(c)** Anchor ice growth when the air temperature is  $-16^{\circ}\text{C}$ .

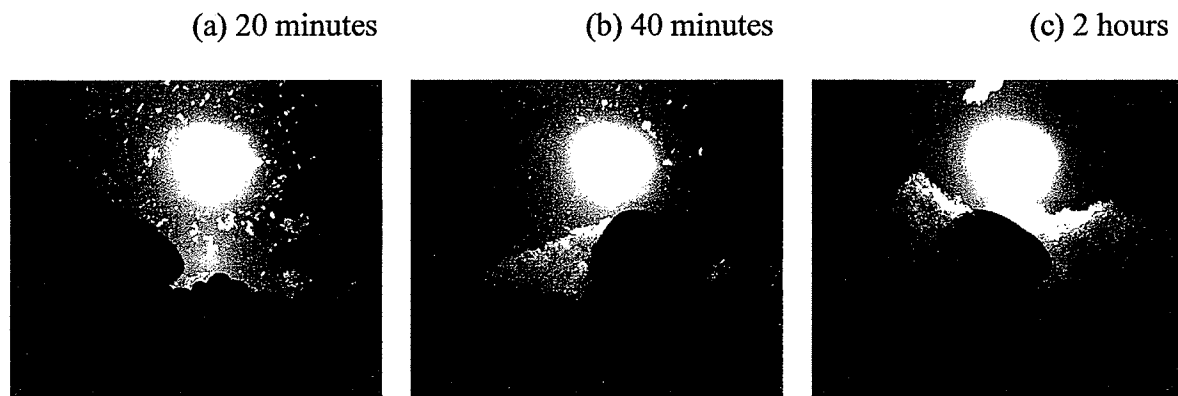


**Figure 3.5(a)-(c)** Anchor ice growth when the air temperature is  $-20^{\circ}\text{C}$ .

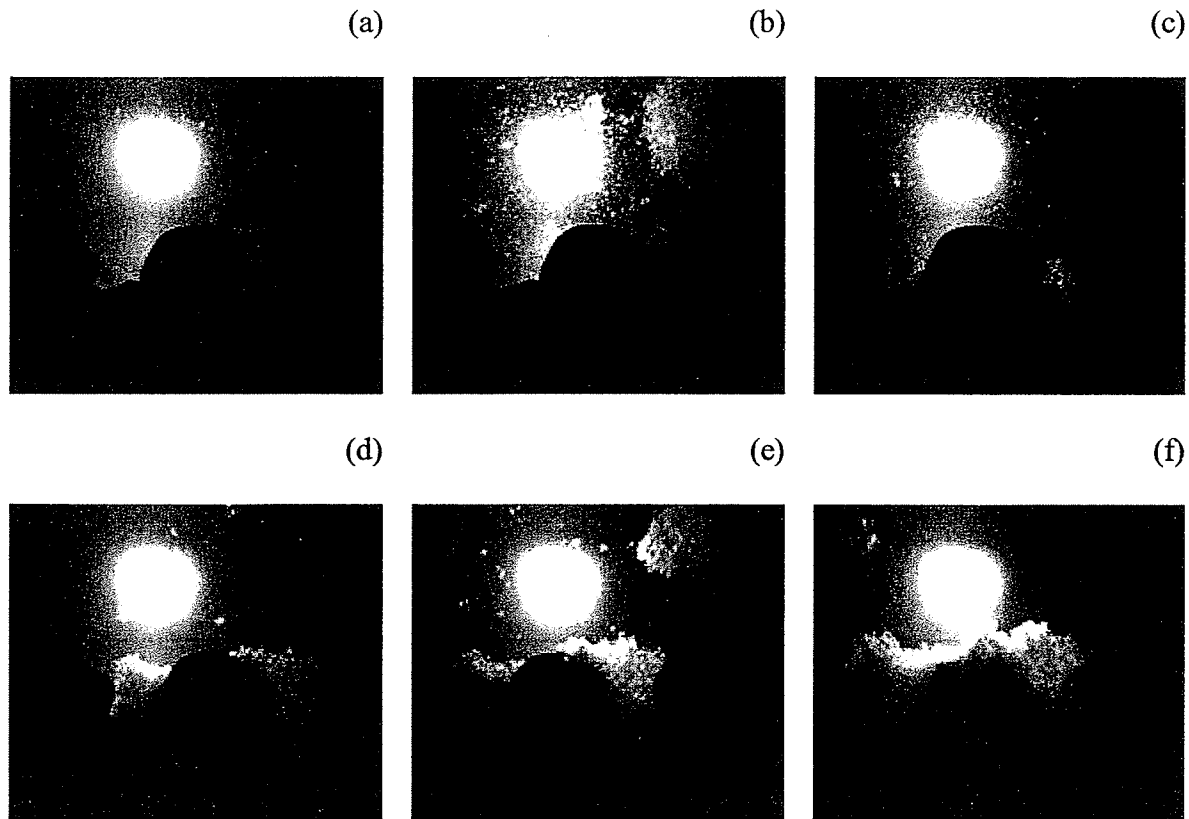


**Figure 3.6(a) - (f)** Anchor ice evolution around five rocks in a row when the velocity is 0.38 m/s, water depth is 10 cm and the air temperature is  $-16^{\circ}\text{C}$ .

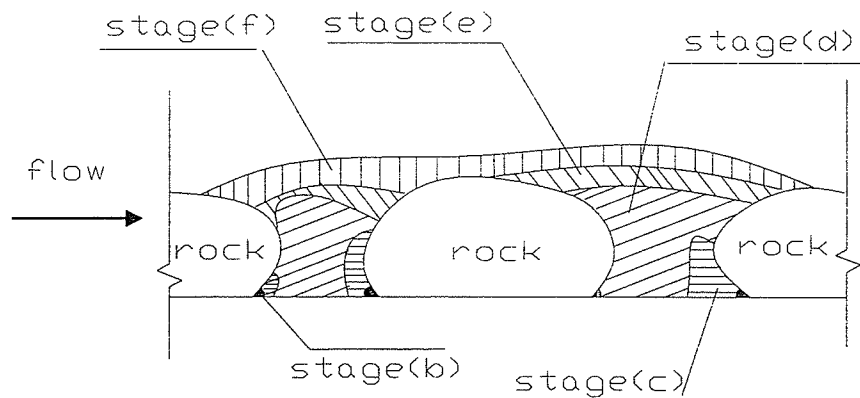


**Figure 3.6(g)** A sketch of the sequence of anchor ice development around the five rocks.

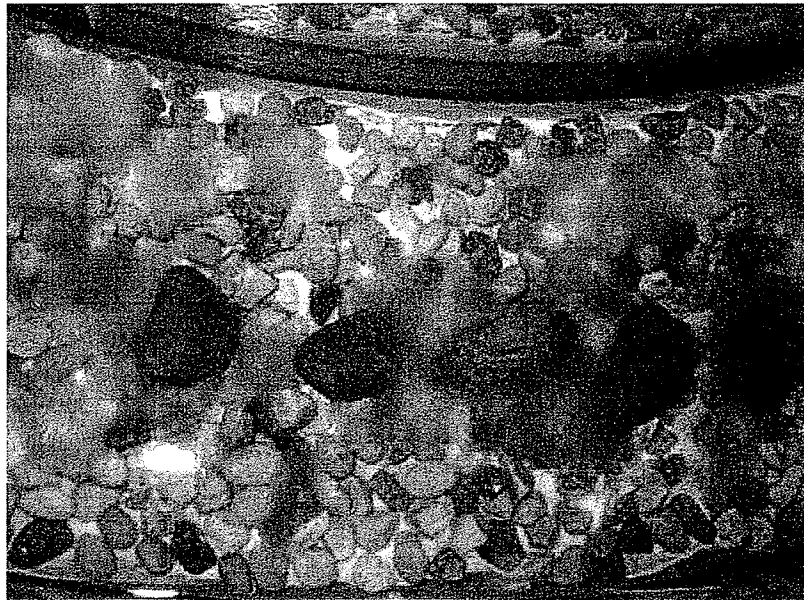


**Figure 3.7** A top view of anchor ice grown on a row of rocks.

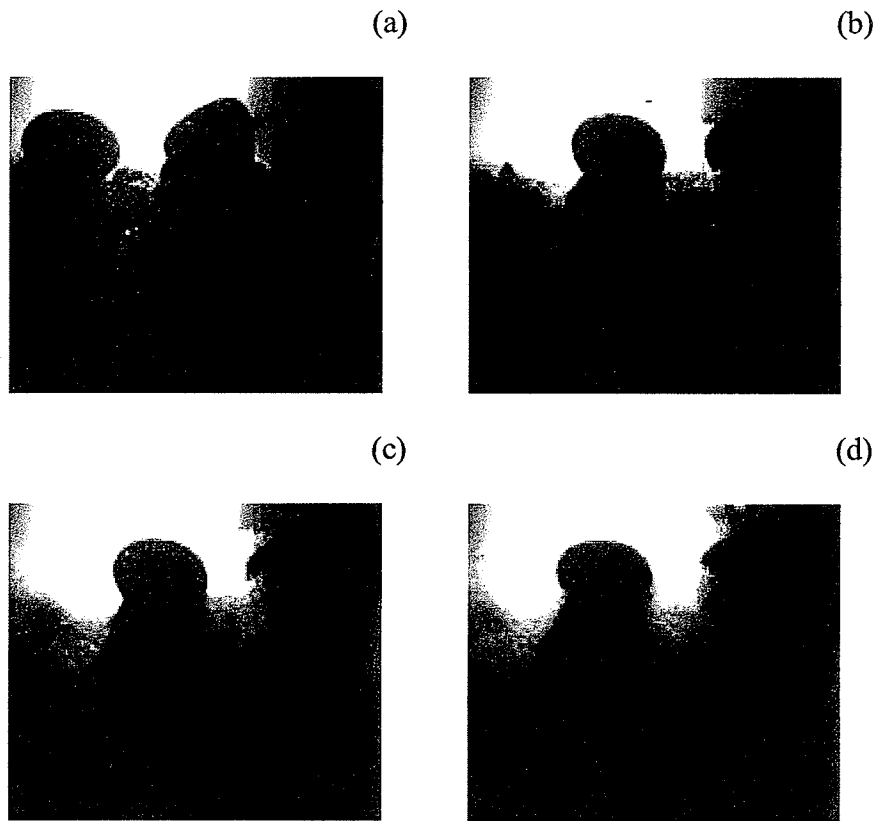


**Figure 3.8(a) – (d)** Anchor ice evolution on six rocks when the velocity is 0.38 m/s, water depth is 10 cm and the air temperature is  $-16^{\circ}\text{C}$ .



**Figure 3.9** A top view of anchor ice on six rocks.

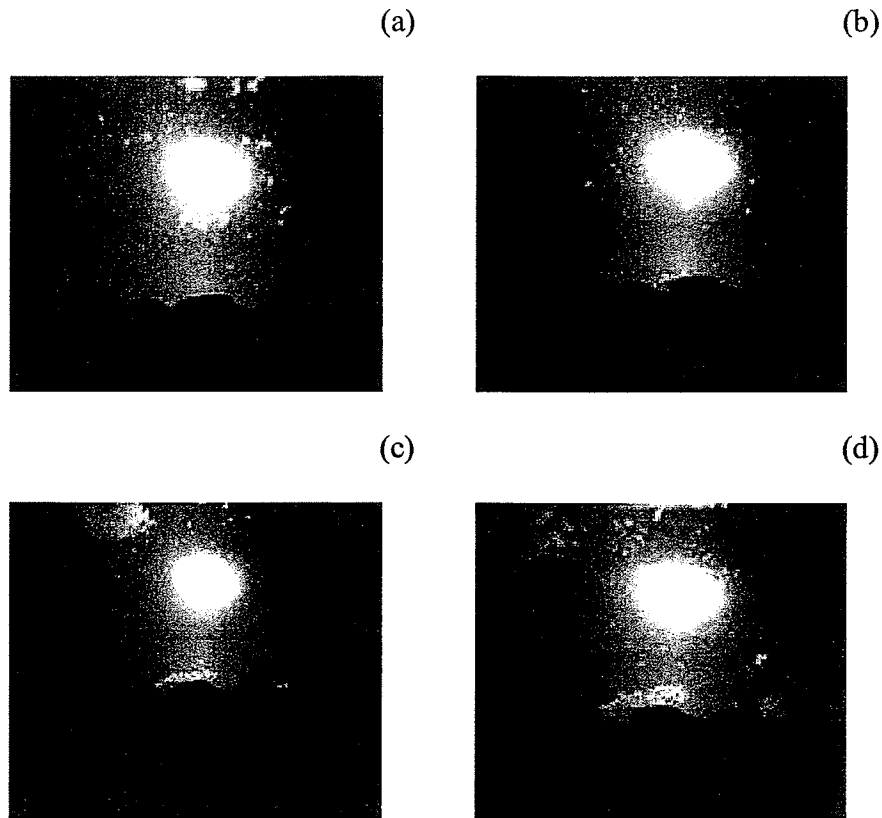


**Figure 3.10** (a) – (d) Evolution of scale shaped anchor ice when the velocity is 0.23 m/s, water depth is 10 cm, the air temperature is  $-16^{\circ}\text{C}$ , and the Froude number is 0.23.

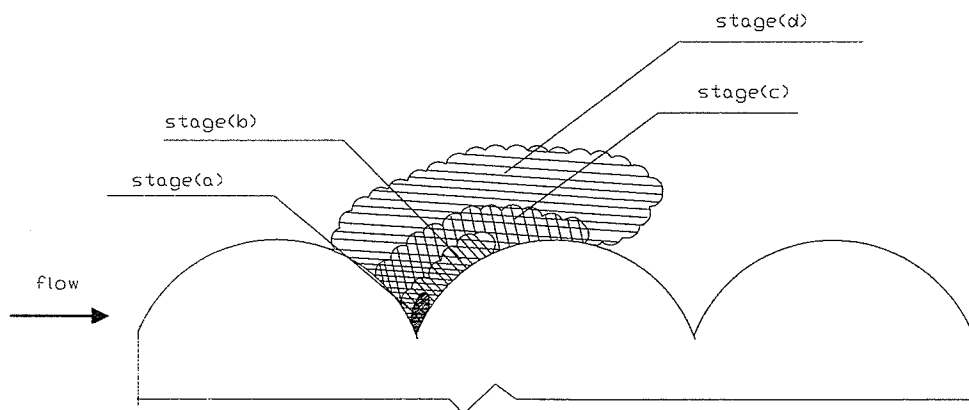


**Figure 3.10(e)** A sketch of the development of scale shaped anchor ice.

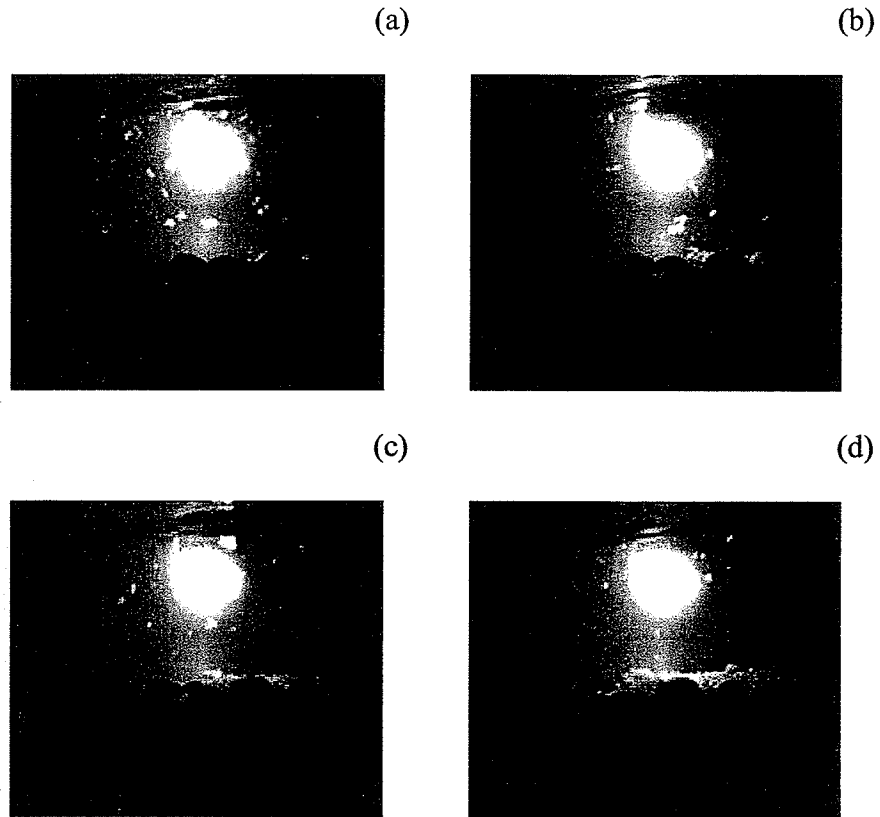


**Figure 3.11(a) – (d)** Evolution of ball shaped anchor ice when the velocity is 0.57 m/s, water depth is 8 cm, air temperature is  $-16^{\circ}\text{C}$ , and Froude number is 0.64.

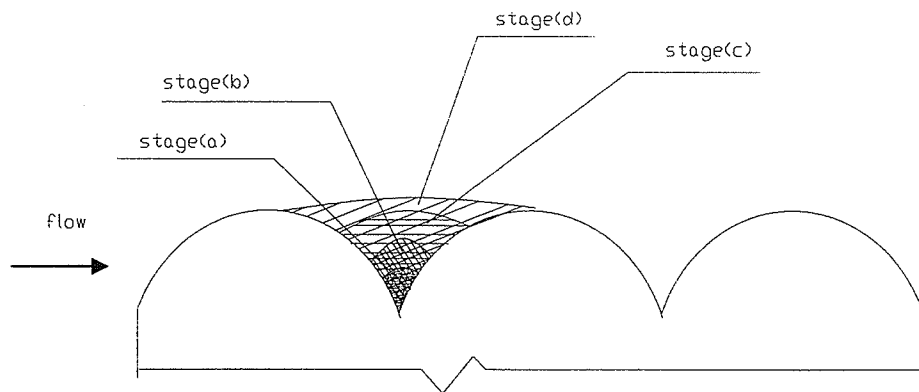


**Figure 3.11(e)** A sketch of the development of ball shaped anchor ice.

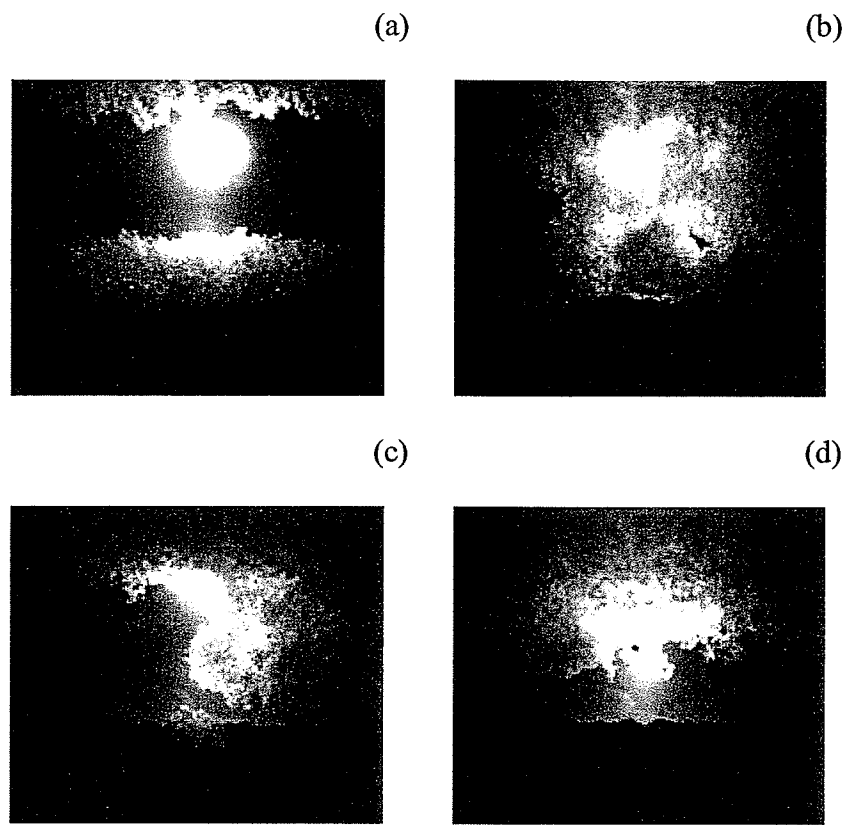


**Figure 3.12(a) – (d)** Release of anchor ice due to the buoyant force when the velocity is 0.38 m/s, water depth is 8 cm, air temperature is  $-16^{\circ}\text{C}$  and the gravel Reynold number is 56.



**Figure 3.13** Release of a big pieced of anchor ice.

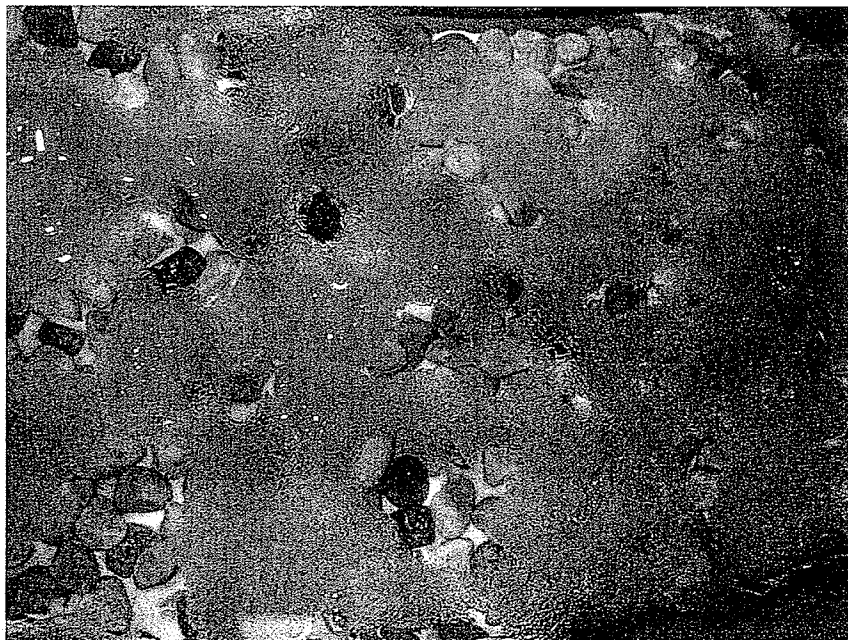


**Figure 3.14** Floating anchor ice slush after releasing.

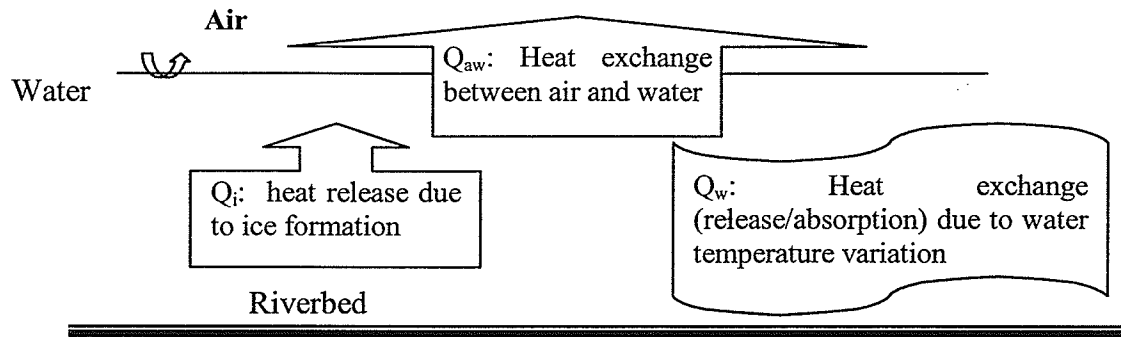


Figure 3.15 Schematic heat balance in a water body.

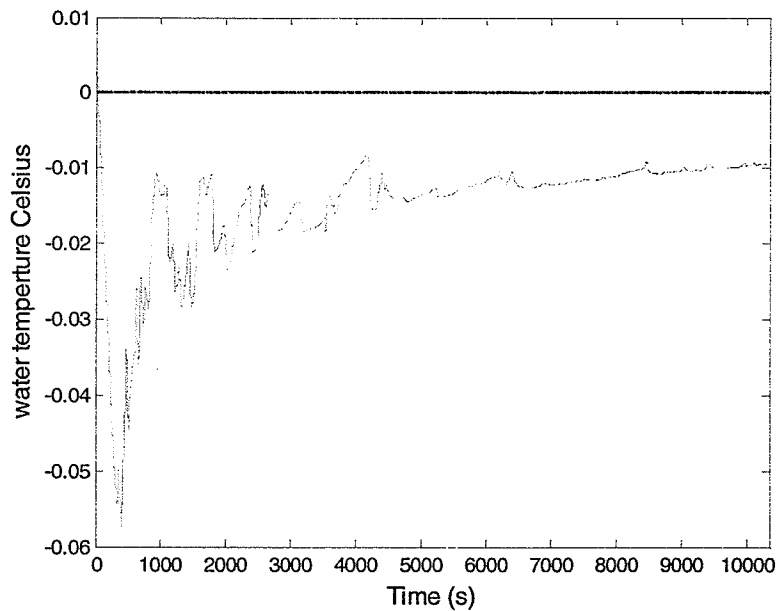


Figure 3.16 The temperature curve when the velocity is 0.38 m/s, water depth is 10 cm, and air temperature is  $-20^{\circ}\text{C}$ .

## *Anchor Ice Growth on Gravel Beds*

---

### **4.1 Introduction**

A series of laboratory studies of anchor ice growth on gravel beds under different hydro-meteorological conditions was carried out. The procedure of the experiments is shown in flow chart 4.1. The digital image processing program introduced in Chapter 2 was employed to analyze anchor ice images and to obtain the thickness of anchor ice during different growth periods. Anchor ice density, an important factor when studying anchor ice growth, was also estimated. The relationships between flow parameters, such as the Froude and Reynolds numbers are discussed. The thickness and growth rate of anchor ice are also analyzed and discussed under different air temperatures and flow parameters. In addition, the torque load signals returned from the GV6 servo motor controller are collected and analyzed to indicate the variation of the bed/ice surface roughness.

## 4.2 Anchor Ice Density and Porosity

### 4.2.1 Measurement of Anchor Ice Density

The density of anchor ice was measured in the present tests as an important factor in studying the mechanism of anchor ice growth. After each test was complete, newly formed anchor ice was brushed off the gravel bed and collected in a bucket and weighed. A sample of brushed off anchor slush is shown in Figure 4.2. The final thickness of the anchor ice at the end of each experiment can be determined through the anchor ice images taken during each experiment. Figure 4.3 (a) shows the original picture of anchor ice before digital image processing. Figure 4.3 (b) shows the binary images of anchor ice after digital image processing. The thickness of the anchor ice can then be calculated from the binary images in units of pixels, which are converted to units of centimeter as outlined in chapter 2.

As a result of the centrifugal force and the associated small residual secondary circulation in the counter-rotating flume, most of the anchor ice blanket was observed to form from the inward flume wall to two-thirds of the width across the flume. Therefore, it is assumed that the anchor ice blanket distributes evenly across two-thirds of the width and that the volume of anchor ice produced can be calculated from the area and the thickness of anchor ice. From the weight and volume of the anchor ice, its density is easily estimated. Table 4.1 summarizes the flow conditions and anchor ice densities of the tests.  $H$  is the flow depth,  $k_s$  is the roughness,  $C_R$  is the cooling rate, (the rate of water temperature decrease toward  $0^\circ\text{C}$ ), which is calculated by fitting a straight line through all the temperature data points before the lowest temperature data point.  $F_r$  is the Froude

number,  $R_e$  is the Reynolds number,  $R_e^*$  is the gravel Reynolds number expressed as  $R_e^* = u_* d_s / \nu$ ,  $u_*$  is the friction velocity,  $d_s$  is the gravel diameter and  $\nu$  is the kinematic viscosity of water.  $W_a$  is the weight of anchor ice and  $h_a$  is the thickness of the anchor ice. The densities found from the present tests range from 160 to 400 kg/m<sup>3</sup>, which is slightly less than the observed unit mass of 300 to 400 kg/m<sup>3</sup> for floating slush ice clusters from anchor ice release reported by Devik and Kanavin (1965). The average porosity of anchor ice in the present study was found to be about 73% which is close to the 75.9% that Parkinson (1984) reported from his field observations in Lake St. Louis at Montreal. However, based on the accuracy of the balance used to weigh the anchor ice and the resolution of digital image processing method, it is conservatively estimated that the error of the computed anchor ice densities are within  $\pm 10\%$ .

**Table 4.1** Summarization of flow parameters and anchor ice densities.

Test No.	$V$ [m/s]	$H$ [m]	$A_t$ [°C]	$C_R$ [°C/s]	$F_r$	$R_e$	$R_e^*$	$W_a$ [kg]	$h_a$ [m] ( $\times 10^{-2}$ )	Density [kg/m <sup>3</sup> ]	porosity
4-21	0.23	0.08	-16	-	0.26	22493	296	2.14	2.69	167	0.83
4-22	0.38	0.08	-12	-	0.43	37485	492	1.80	2.02	187	0.81
4-23	0.57	0.08	-16	-	0.64	56228	737	3.73	2.29	344	0.65
4-25	0.38	0.1	-20	-0.0002	0.38	42171	476	4.18	2.67	330	0.66
4-26	0.38	0.1	-16	-	0.38	42171	476	3.27	2.41	286	0.71
4-27	0.38	0.1	-12	-0.00009	0.38	42171	476	2.25	2.19	217	0.78
4-28	0.23	0.1	-16	-	0.23	25304	286	1.45	2.6	118	0.88
4-29	0.57	0.1	-16	-0.0001	0.57	63256	713	3.39	2.13	335	0.66
4-30	0.38	0.12	-20	-0.0001	0.35	46004	465	2.59	2.31	237	0.76
5-02	0.38	0.12	-16	-0.0001	0.35	46004	465	3.98	2.62	321	0.67
5-03	0.23	0.12	-16	-	0.21	27605	279	2.05	2.39	180	0.82
5-04	0.38	0.12	-12	-0.00005	0.35	46004	465	1.82	1.52	252	0.74
5-05	0.57	0.12	-16	-0.0001	0.52	69007	697	3.41	1.79	401	0.59
5-06	0.38	0.08	-16	-	0.43	37485	492	3.41	2.35	306	0.69

Note, - data not available due to intermittent submergence of the thermometer probe.

## **4.2.2 Effect of Flow Parameters on Anchor Ice Density**

**4.2.2.1 Effect of Froude Number.** An analysis of the relationship between the Froude number and anchor ice density reveals that anchor ice density increases with the Froude number, as shown in Figure 4.4. The experimental results agree well with field observations that indicate that anchor ice grows more densely and quickly in shallow rapids where the Froude number is larger than in deep rivers where the Froude number is smaller.

**4.2.2.2 Effect of gravel Reynolds number on anchor ice porosity.** From the anchor ice images taken during the tests it was observed that anchor ice porosity, just like anchor ice density, can be affected by air temperature and bottom roughness. It is hard to analyze the statistical effect of the air temperature on anchor ice porosity since only three air temperatures were used in the tests. Therefore, only the gravel Reynolds number is employed here to indicate the effect of bed roughness and velocity on anchor ice porosity. The anchor ice porosity, which is derived from anchor ice density, is listed in Table 4.1. Figure 4.5 shows the relationship between anchor ice porosity and the gravel Reynolds number when the air temperature is  $-16^{\circ}\text{C}$ . It can be seen that anchor ice porosity decreases with the increasing gravel Reynolds number, and while a straight line is shown, there is no obvious reason to expect this relationship to be linear.

## **4.3 Variation of the Bed/Ice Surface Roughness**

Experimental observations have shown that the bed/ice surface roughness can change with the growth of anchor ice. As described previously, a GV6 motor controller system

was used to return torque load signals from the encoder over a RS232 cable. A program was developed using Labview to collect the torque loads at a certain frequency. The torque load collected was then analyzed to indicate the change of the bed/ice surface roughness. The principle underlying this analysis is as follows: the drag force on the flume bottom will change with the growth of anchor ice, which in turn will be reflected in the variation of the torque load signals. Then by transferring torque load signals to Manning's  $n$  value, the variation of bed/ice surface roughness can be determined.

### **4.3.1 Analysis of the Torque Load Signals**

The torque load signals were collected during two periods of each test. The first torque loads, referred to as reference torque loads, were collected when the water temperature was between  $0.06^{\circ}\text{C}$  and  $0^{\circ}\text{C}$  and the water was still free of ice. The second set, known as ice torque loads, were collected after the water temperature dropped below zero and frazil ice started to form. The ice torque loads were collected until the test period was complete. Both the reference and ice torque load signals were analyzed for the present tests and were found to match well with normal distributions. Figures 4.6(a) and (b) show the original reference and ice torque load signal while Figures 4.6(c) and (d) show the distributions of the reference and ice torque load signals, respectively, for an air temperature of  $-16^{\circ}\text{C}$ , velocity of  $0.23\text{ m/s}$ , and bed roughness of  $2\text{ cm}$ .

### **4.3.2 Derivation of the Manning's $n$**

For each test, the water depth and the rotation rate of the counter-rotating flume were maintained constant, therefore, the assumption of uniform flow is employed and related

formula are used in the derivation of Manning's 'n'. The torque loads collected during the tests are converted to a corresponding Manning's 'n' as follows. Manning's 'n' is given by (Chow, 1959)

$$n = \frac{1}{V} R^{2/3} \sqrt{S_f}, \quad (4-1)$$

where  $V$  is the velocity,  $R$  is the hydraulic radius,  $n$  is the Manning's  $n$ , and  $S_f$  is the friction slope, which can be expressed by the hydraulic radius and the mean boundary shear stress in the flow direction as

$$S_f = \frac{\tau}{\gamma R}. \quad (4-2)$$

$\tau$  is the mean boundary shear stress and  $\gamma$  is the specific weight of the fluid.

By substituting equation (4-2) into equation (4-1), we have

$$n = \frac{1}{V} R^{2/3} \sqrt{\frac{\tau}{\gamma R}} \quad (4-3)$$

The bed torque load is given by

$$T_{torque} = \tau A_b r. \quad (4-4)$$

The mean boundary shear stress can therefore be expressed as a function of the torque load, i.e.,

$$\tau = \frac{T_{torque}}{A_b r}, \quad (4-5)$$

where,  $A_b$  is the area of the flume bed and  $r$  is the centerline radius of the flume bed.

Substituting equation (4-5) into equation (4-3), gives Manning's 'n' as a function of some constants of the measured torque load, viz.,

$$n = \frac{R^{2/3}}{V} \sqrt{\frac{T_{torque}}{\gamma A_b r}} \quad (4-6)$$

After simplification, we have

$$n = \frac{R^{1/6}}{V} \sqrt{\frac{T_{torque}}{\gamma A_b r}} \quad (4-7)$$

Therefore, Manning's 'n' can be calculated from the collected torque load data.

### 4.3.3 Analysis of Manning's 'n'

It was observed during each test that the torque load signals returned were affected by the air temperature, water depth and the bed velocity even without any ice production. For example, when the other conditions are the same, the torque load signals collected when the air temperature is  $-20^{\circ}\text{C}$  are greater than those when the air temperature is  $-12^{\circ}\text{C}$  with the water still free of ice. Therefore, during the process of analyzing torque load signals, the reference torque loads (collected before ice formed) were subtracted from the ice torque loads (collected after ice formed) in each test in order to eliminate the effects of other factors on the torque loads other than anchor ice. Therefore, there are two kinds of Manning's 'n' involved in the present paper. One is derived from the original ice torque loads (without subtracting the reference torque load) directly and it is called the absolute Manning's 'n'. The other is derived from the subtracted ice torque loads (after subtracting of the reference torque load) and it is called the relative Manning's 'n', which only indicates the change of the bed/ice surface roughness caused by the growth of anchor ice. Figures 4.7 (a) and (b) show the variations of the absolute and relative Manning's 'n' profiles with the growth of anchor ice when the gravel bed roughness is 2

cm, the cold room temperature is  $-16^{\circ}\text{C}$  and the velocity is 0.23 m/s. Table 4.2 lists the flow parameters and absolute Manning's 'n' of some tests.

Similar to what Kerr et al. (2002) observed from his tests, the variation of Manning's 'n' is divided into three different stages as shown in Figure 4.7(b). Figures 4.8(a) - (c) show the actual anchor ice images corresponding to these three different stages. It can be seen from Figures 4.7 and 4.8 that 'n' increases at the beginning of a test when anchor ice was randomly spread over the gravel bed (stage a). As a test progressed, the roughness value reached a peak; during this time the gaps between the gravel particles were gradually being filled in by frazil ice accumulation (stage b). The actual gravel bed was then raised and smoothed by continued frazil ice adhesion to the bottom and the roughness gradually decreased as the test progressed (stage c). The duration of the above process varied from test to test, depending on the actual test conditions. It was observed in the present experiments that some of the roughness curves showed the complete process in the three hour experimental period while others only captured the ascending portion or the beginning of the descending part of the curves because of the inadequate testing period.

**Table 4.2** Summary of flow parameters and Manning's 'n'.

Test No.	Exp. Duration [mins]	$V$ [m/s]	$H$ [m]	$k_s$ [m]	$A_t$ [°C]	Cooling Rate [°C/s]	$F_r$	$R_e$	Mean absolute 'n'	Mean relative 'n'
2-23	211	0.38	0.1	0.01	-16	-	0.38	42171	0.021	0.0068
3-9	173	0.38	0.12	0.01	-16	-0.0001	0.35	46004	0.021	0.0045
3-12	179	0.57	0.12	0.01	-16	-0.00008	0.52	69007	0.014	0.0018
3-18	174	0.38	0.08	0.01	-16	-	0.43	37485	0.019	0.0045
3-19	172	0.38	0.08	0.01	-20	-	0.43	37485	0.020	0.0054
3-25	187	0.23	0.08	0.01	-16	-	0.26	22493	0.035	0.0095
3-26	169	0.23	0.1	0.01	-16	-	0.23	25304	0.034	0.0094
3-31	156	0.38	0.08	0.0034	-16	-	0.43	37485	0.020	0.0033
4-2	155	0.57	0.08	0.0034	-16	-	0.64	56228	0.013	0.0010
4-4	161	0.23	0.08	0.0034	-16	-	0.26	22493	0.033	0.0074
4-5	129	0.38	0.1	0.0034	-20	-0.0001	0.38	42171	0.021	0.0041
4-8	107	0.23	0.1	0.0034	-16	-	0.23	25304	0.033	0.0084
4-9	157	0.38	0.1	0.0034	-12	-0.00008	0.38	42171	0.019	0.0026
4-12	145	0.38	0.12	0.0034	-16	-0.0001	0.35	46004	0.021	0.0030
4-14	146	0.57	0.12	0.0034	-16	-0.00009	0.52	69007	0.014	0.0008
4-21	182	0.23	0.08	0.02	-16	-	0.26	22493	0.034	0.0063
4-26	164	0.38	0.1	0.02	-16	-	0.38	42171	0.021	0.0039
4-28	174	0.23	0.1	0.02	-16	-	0.23	25304	0.035	0.0065
4-29	171	0.57	0.1	0.02	-16	-0.0001	0.57	63256	0.013	0.0006

Note, - data not available due to intermittent submergence of the thermometer probe.

### 4.3.4 Effect of Air Temperature and Flow Parameters on Manning's 'n'

**4.3.4.1 Effect of air temperature.** Air temperature has a significant effect on the variation of the bed/ice surface roughness. Three different air temperatures ( $-20^{\circ}\text{C}$ ,  $-16^{\circ}\text{C}$  and  $-12^{\circ}\text{C}$ ) were applied during the tests. The effects of air temperature on the

change in Manning's 'n' due to the growth of anchor ice are discussed. Figures 4.9 and 4.10 below show the relative and absolute Manning's 'n' under different air temperatures. It can be seen that only the ascending parts of the curves are shown in the figures because the tests were not long enough to record the complete process. The figures also show that the rate of change in roughness decreases gradually as the tests continue. In Figure 4.10 the descending limbs of the curves and reduction in Manning's 'n' are obvious by the end of the tests. It is also clear that the rate of change in Manning's 'n' increases with a decrease in air temperature. When the air temperature is  $-20^{\circ}\text{C}$ , the slope of the roughness curve is steeper than when the air temperature is  $-12^{\circ}\text{C}$  and the mean relative Manning's 'n' is also greater when the air temperature is  $-20^{\circ}\text{C}$  than that when the air temperature is  $-12^{\circ}\text{C}$ . This can be explained by the fact that when the air temperature is lower, more frazil ice particles form in a shorter period of time and anchor ice forms on the flume bed more quickly. Therefore, both the absolute and relative values and rate of change of Manning's 'n' is greater when the air temperature is colder.

**4.3.4.2 Effect of velocity.** Three different velocities were employed during the tests and the effects of the velocities on the change in bed/ice surface roughness were also explored. Figure 4.11 shows the curve of the relative Manning's 'n' when the gravel bed roughness is 1 cm, the air temperature is  $-16^{\circ}\text{C}$  and the water depth is 8 cm. Figure 4.12 shows the relative Manning's 'n' when the gravel bed roughness is 2 cm, the air temperature is  $-16^{\circ}\text{C}$  and the water depth is 10 cm. It can be seen from these figures that both the rate of change in Manning's 'n' and the mean relative Manning's 'n' increase

with a decrease in the velocity. In addition, it is also clear that it takes less time to reach the peak roughness when the velocity is lower.

**4.3.4.3 Effect of Froude and Reynolds numbers.** The variations of the relative Manning's 'n' with the growth of anchor ice under different Froude numbers are shown in Figure 4.13. Figures 4.14 and 4.15 show the effects of Froude and Reynolds numbers on the mean relative Manning's 'n' when the gravel bed roughness is 0.34 cm, 1 cm and 2 cm, respectively. It can be seen from these figures that an increase in the Froude and Reynolds numbers leads to a decrease in the mean relative Manning's 'n'. This matches well with the experimental images that indicate when the flow is more turbulent, frazil ice fills in the gaps between the gravel particles more quickly and evenly, which causes a smaller change in the bed/ice surface roughness than when the flow is less turbulent.

## **4.4 Anchor Ice Growth Rate**

### **4.4.1 Analysis of the Growth Rate of Anchor Ice**

It was observed that anchor ice grew the quickest during the peak production of frazil ice particles, which occurred usually during the first hour of the tests as shown in Figure 4.16. Therefore, the thickness and growth rate of anchor ice were analyzed every 5 minutes in the first hour of each test and after that, they were analyzed every 15 or 30 minutes by the image processing program.

Figures 4.17(a) and (b) show the thickness and corresponding growth rate curves of anchor ice when the water depth is 10 cm, the roughness height is 0.34 cm, the flow

velocity is 0.38 m/s and the air temperature is  $-16^{\circ}\text{C}$ . It can be seen that at the initial growth stage, anchor ice grew fast and that the growth rate reached its peak in about 18 minutes. After the peak, the growth rate decreased quickly; from Figure 4.17(a) we can see that the slope of the anchor ice thickness curve is much flatter than that at the beginning, and anchor ice grew slowly during this period. Figures 4.18(a) and (b) show the thickness and growth rate curves of anchor ice when the water depth is 8 cm, the roughness height is 0.34 cm, the flow velocity is 0.23 m/s and the air temperature is  $-16^{\circ}\text{C}$ . It is seen from Figure 4.18(a) that the thickness of anchor ice did not increase constantly and there are setbacks shown in the growth process. As a result, the growth rate curve of anchor ice shown in Figure 4.18(b) had more than one peak and it took 26 minutes to reach the first peak. From the observations of the corresponding test, it was found that anchor ice release occurred frequently during the test period; this is believed to be the main cause for the fluctuation of the anchor ice thickness and growth rate curves. (See appendix C for more anchor ice thickness and growth rate curves). Table 4.3 summarizes the flow parameters and experimental results for the growth rate of anchor ice on gravel beds.

During each test, the time it took from the first appearance of frazil ice to the peak accumulation of anchor ice varied according to the actual experimental conditions and their effect will be discussed in the following paragraphs.

**Table 4.3** Summary of flow parameters and experimental growth rate of anchor ice.

Test No.	Exp. duration [mins]	$V$ [m/s]	$H$ [m]	$k_s$ [m]	$A_t$ [°C]	Cooling rate [°C/s]	$F_r$	$R_e$	$h_a$ [m] ( $\times 10^{-2}$ )	$G_{re}$ [m/s] ( $\times E(-6)$ )
2-23	211	0.38	0.1	0.01	-16	-	0.38	42171	2.24	1.77
3-3	163	0.57	0.1	0.01	-16	-0.0001	0.57	63257	1.71	1.75
3-9	173	0.38	0.12	0.01	-16	-0.0001	0.35	46004	2.15	2.1
3-12	179	0.57	0.12	0.01	-16	-0.00008	0.52	69007	1.69	1.75
3-18	174	0.38	0.08	0.01	-16	-	0.43	37485	2.61	2.5
3-22	173	0.57	0.08	0.01	-16	-	0.64	56228	2.23	2.15
3-25	187	0.23	0.08	0.01	-16	-	0.26	22493	3.36	3
3-26	169	0.23	0.1	0.01	-16	-	0.23	25304	2.93	2.9
3-31	156	0.38	0.08	0.0034	-16	-	0.43	37485	2.12	2.27
4-2	155	0.57	0.08	0.0034	-16	-	0.64	56228	1.88	2.02
4-6	158	0.38	0.1	0.0034	-16	-0.0001	0.38	42171	2.08	2.18
4-7	172	0.57	0.1	0.0034	-16	-0.0001	0.57	63257	1.91	1.85
4-21	182	0.23	0.08	0.02	-16	-	0.26	22493	2.78	2.55
4-23	162	0.57	0.08	0.02	-16	-	0.64	56228	2.12	2.12
4-26	164	0.38	0.01	0.02	-16	-	0.38	42171	2.29	2.33
4-28	174	0.23	0.01	0.02	-16	-	0.23	25304	2.49	2.38
4-29	171	0.57	0.01	0.02	-16	-0.0001	0.57	63256	2.16	2.1
5-2	175	0.38	0.12	0.02	-16	-0.0001	0.35	46004	2.57	2.45
5-3	176	0.23	0.12	0.02	-16	-0.00006	0.21	27605	2.42	2.3

Note, - data not available due to intermittent submergence of the thermometer probe.

#### 4.4.2 Effect of the air temperature and flow parameters

**4.4.2.1 Effect of the air temperature.** As observed in the tests, air temperature has a significant effect on the growth of anchor ice. Figure 4.19 (a) and (b) show the thickness and growth rate of anchor ice under different air temperatures (-20°C, -16°C and -12°C) while the other conditions are held the same. It can be seen from the figures that when the air temperature is lower, anchor ice grows quicker and it takes less time to reach the

peak growth rate. This can be explained by the fact that when the air temperature decreases, the supercooling rate of the water increases and there are more frazil ice particles produced in the supercooled water. As a result, more frazil ice will be entrained and carried to the flume bed by turbulence to accumulate as anchor ice. The thickness of anchor ice increases rapidly as more and more frazil ice attaches to the flume bed and soon the peak growth rate is reached. In contrast to the above, when the air temperature is relatively warmer, there is not as much frazil ice produced as when the air temperature is colder, so anchor ice grows more slowly as there is not as much frazil ice entrained in the flow and it takes more time (as shown in Figure 4-19(b)) to reach the peak growth rate.

**4.4.2.2 Effect of gravel bed roughness height.** Three sets of gravel beds with different roughness heights (0.34 cm, 1 cm, 2 cm) were used to test the effect of the bed roughness on the thickness and growth rate of anchor ice. As shown in Figure 4.20(a), at the initial growth stage, anchor ice on a gravel bed with relatively small roughness grew the quickest. Figures 4.21(a) and (b) show the images of anchor ice thickness 30 minutes after the first appearance of frazil ice when the roughness is 0.34 cm and 2 cm, respectively, and all other conditions are the same. But as the process continued, the anchor ice on the gravel bed with relatively large roughness eventually outgrew the anchor ice with smaller roughness as shown in the later portion of the Figure 4.20(a). It can also be seen from Figure 4.20(b) that with an increase in gravel bed roughness, the time from the first appearance of frazil ice particles to the peak of the growth rate is prolonged.

**4.4.2.3 Effect of Froude number.** The effect of Froude number on the thickness and growth rate of anchor ice is shown in Figures 4.22(a) and (b). Seven tests with different Froude numbers are illustrated in these figures. There is not enough turbulence in the water to entrain and carry frazil ice to the flume bed because of the low velocity associated with a low Froude number, so anchor ice grows more slowly than when the Froude number is high, as shown in Figure 4.22(a). It can also be clearly seen that at a later stage of the test, anchor ice formed with conditions that produce small Froude numbers outgrows the anchor ice produced for greater Froude numbers. But from the density analysis shown in Figure 4.4, it is clear that although the anchor ice is eventually thicker under a small Froude number, its density is relatively low. Frazil ice does not attach to itself tightly and the bonding forces between anchor ice and the gravel bed is not strong, therefore, release of anchor ice was observed often during the tests when the Froude number was small. In addition, it is observed from Figure 4.22(b) that it takes less time to reach the peak growth rate of anchor ice with increasing Froude numbers. The time when the peak growth rate occurred under each Froude number is shown in Figure 4.23.

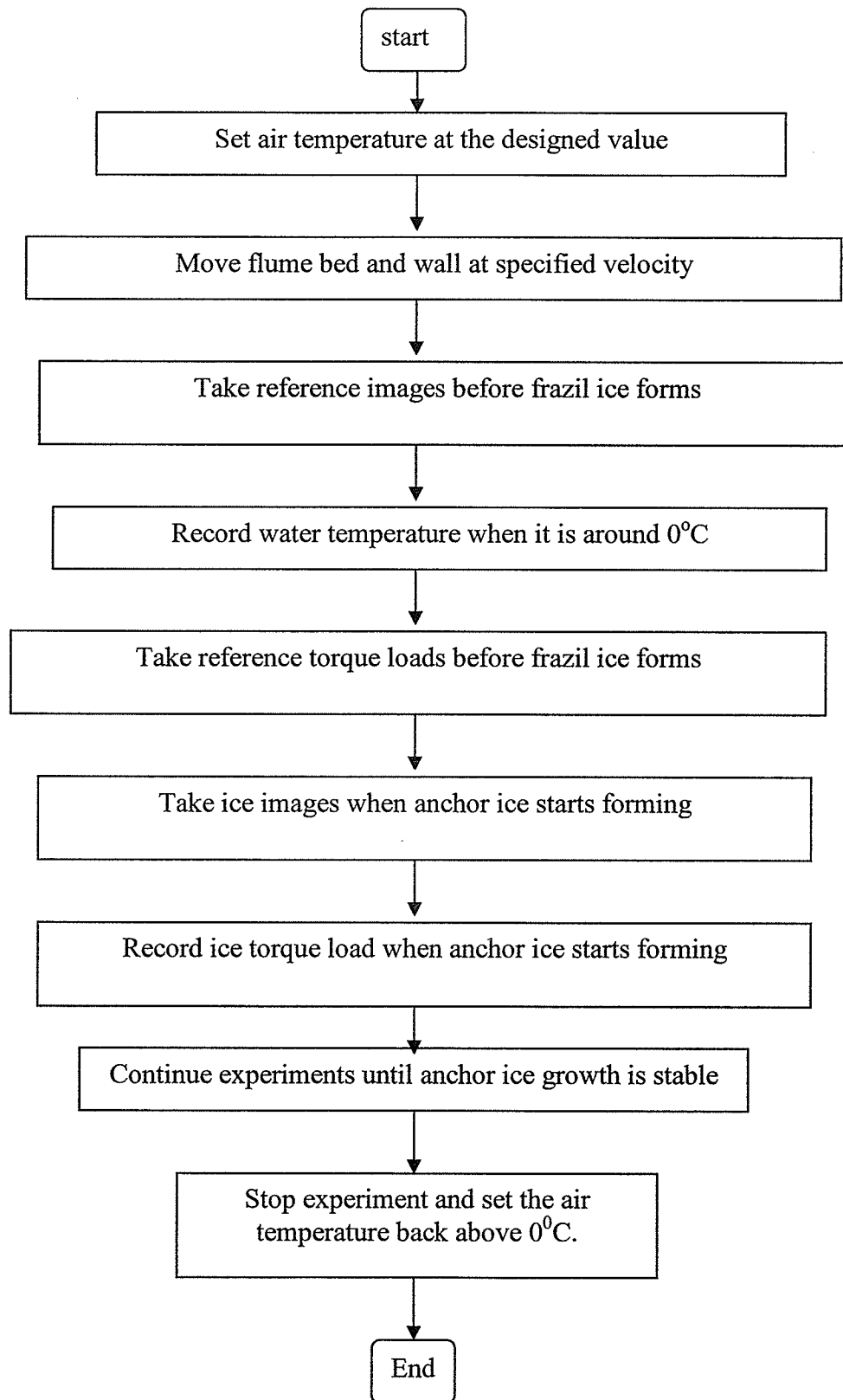
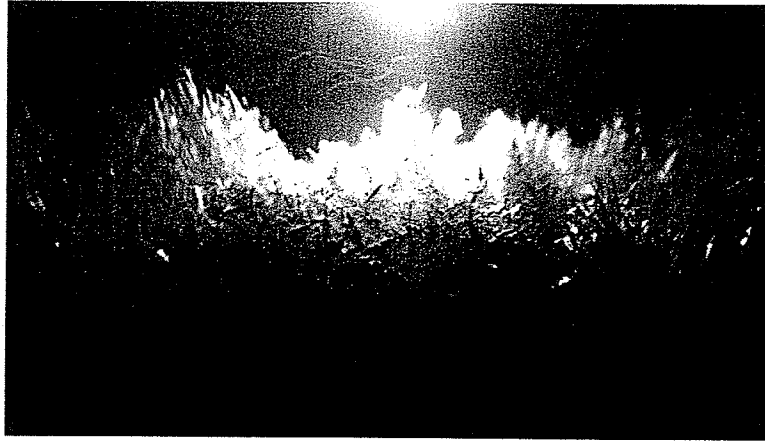


Figure 4.1 Procedure of the experiments.



**Figure 4.2** Removal of anchor ice “blanket”.



**Figure 4.3(a)** Anchor ice image before digital image processing.

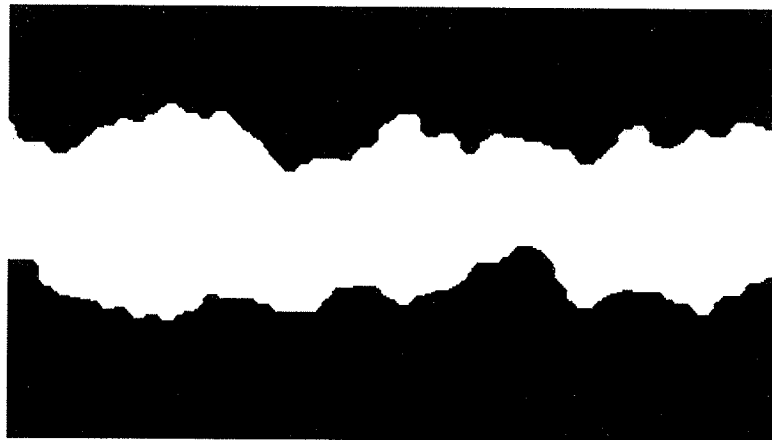


**Figure 4.3(b)** Anchor ice image after digital image processing.

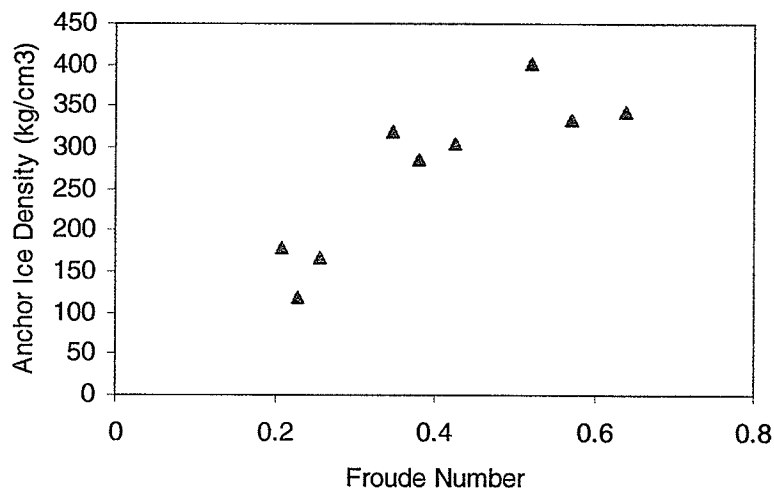


**Figure 4.4** Effect of Froude number on anchor ice densities when the air temperature is  $-16^{\circ}\text{C}$ .

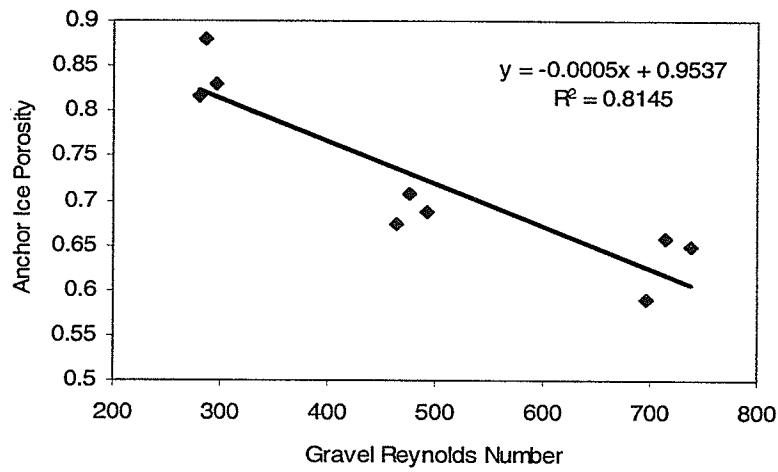
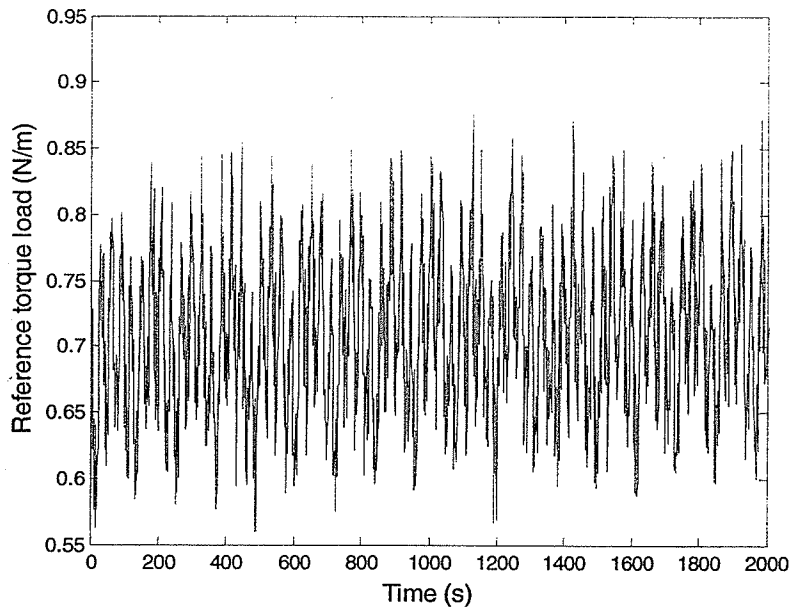
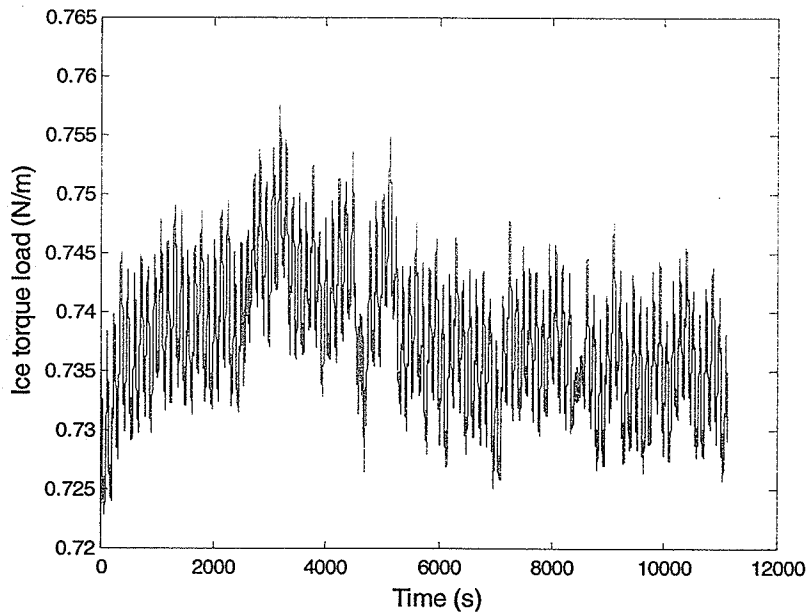


**Figure 4.5** Linear regression between anchor ice porosity and gravel Reynolds number.

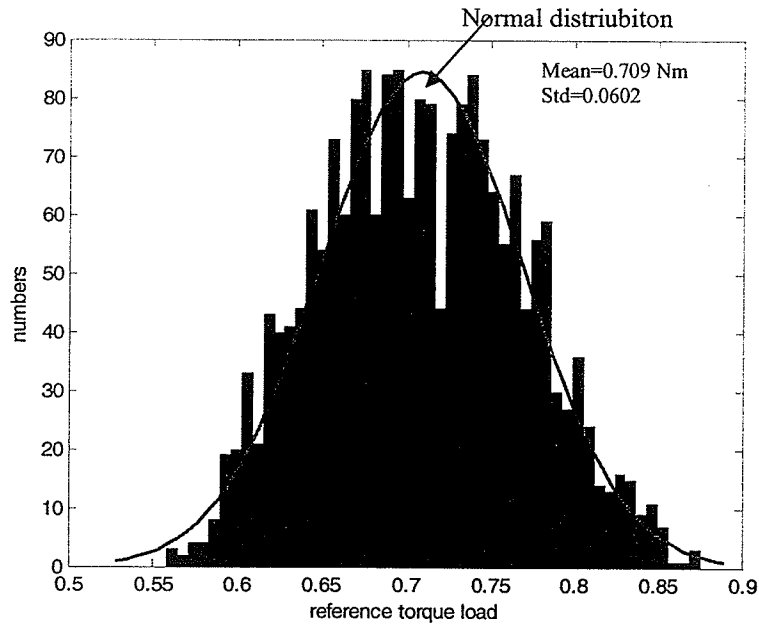


(a)

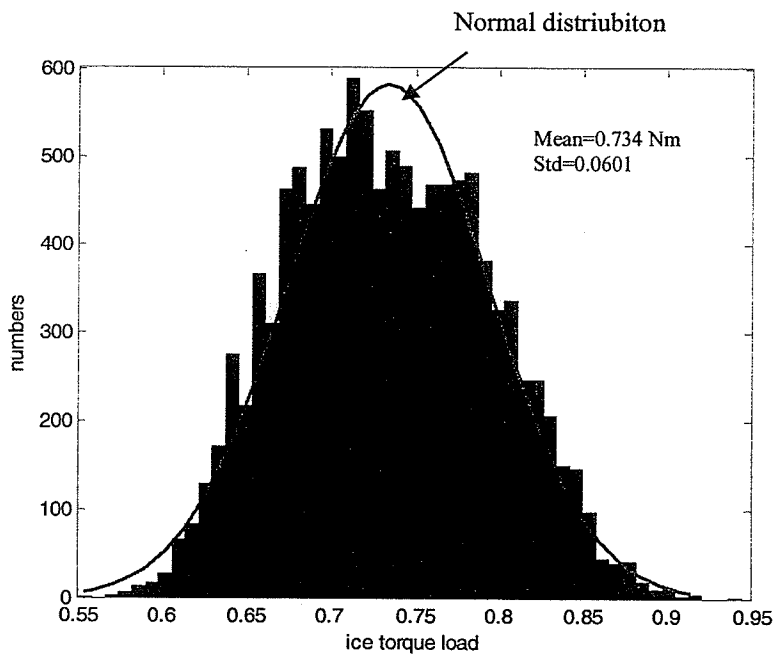


(b)

**Figure 4.6(a)** The original reference torque load signals, and **(b)** the original ice torque load signals when the air temperature is  $-16^{\circ}\text{C}$ , the velocity is  $0.23\text{ m/s}$  and the gravel bed roughness is  $2\text{ cm}$ .

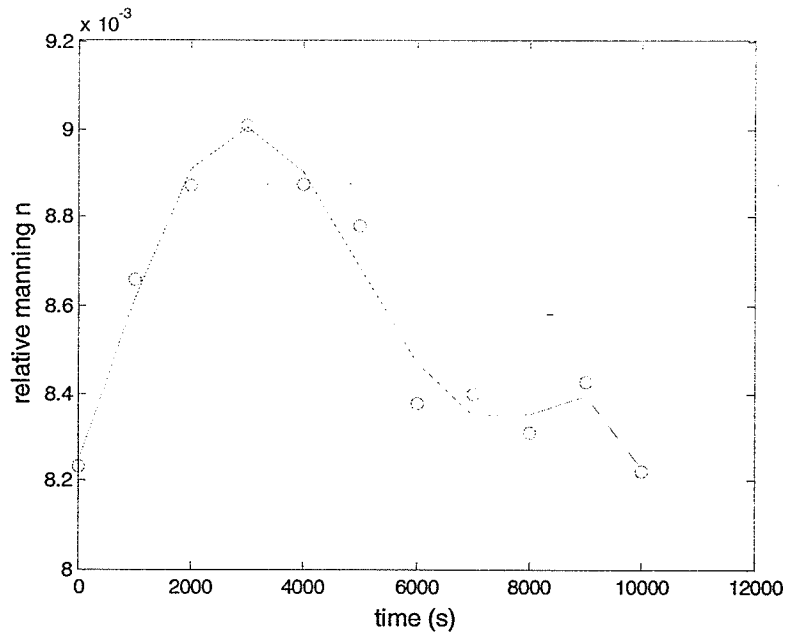


(c)

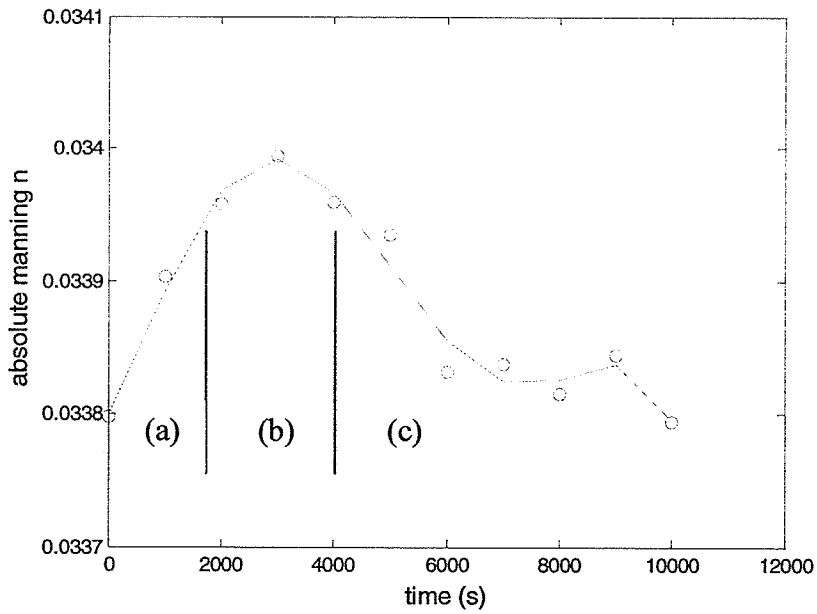


(d)

**Figure 4.6**(c) The distribution of reference torque load signals; and (d) the distribution of ice torque load data when the air temperature is  $-16^{\circ}\text{C}$ , the velocity is  $0.23\text{ m/s}$  and the gravel bed roughness is  $2\text{ cm}$ .



(a)

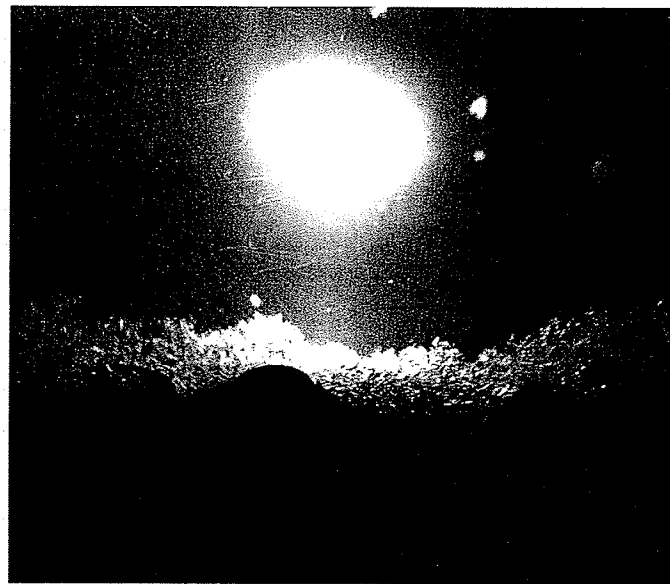


(b)

**Figure 4.7(a)** The change of relative Manning's  $n$  with the growth of anchor ice and **(b)** the change of absolute Manning's  $n$  with the growth of anchor ice when the water temperature is  $-16^{\circ}\text{C}$ , the velocity is  $0.23\text{ m/s}$  and the gravel roughness is  $2\text{ cm}$ .

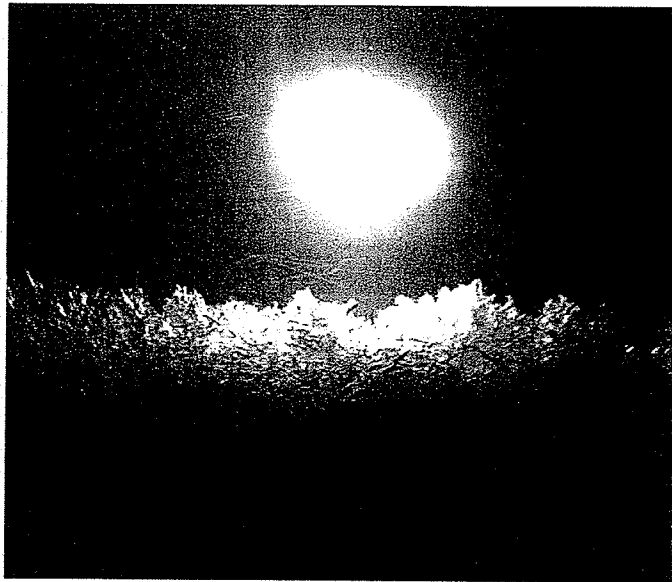


(a)



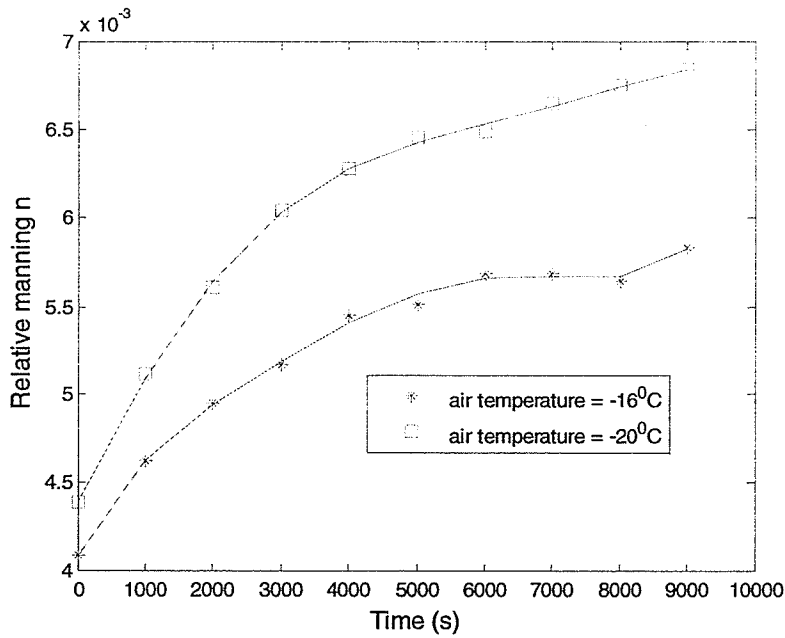
(b)

**Figure 4.8(a)–(b)** Actual anchor ice images corresponding to different stages of bed/ice surface roughness change.

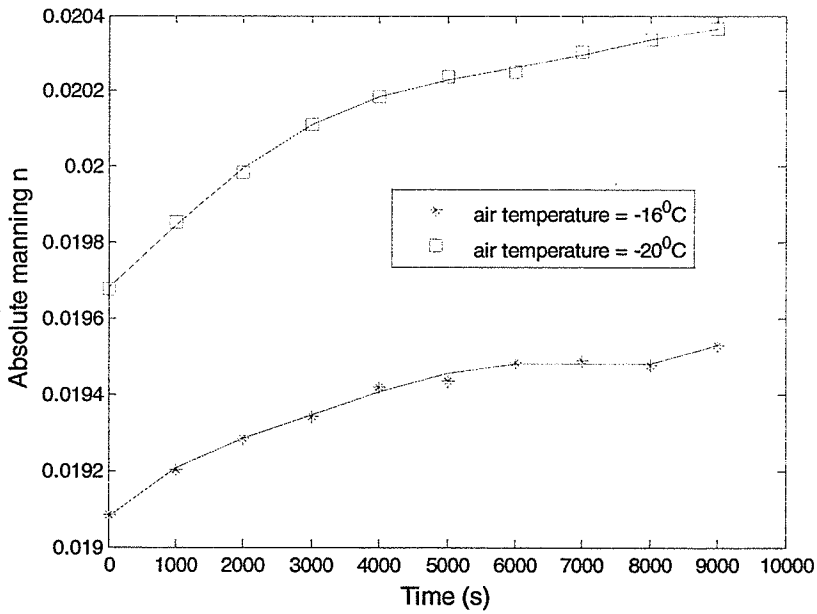


(c)

**Figure 4.8(c)** Actual anchor ice images corresponding to different stages of bed/ice surface roughness change.

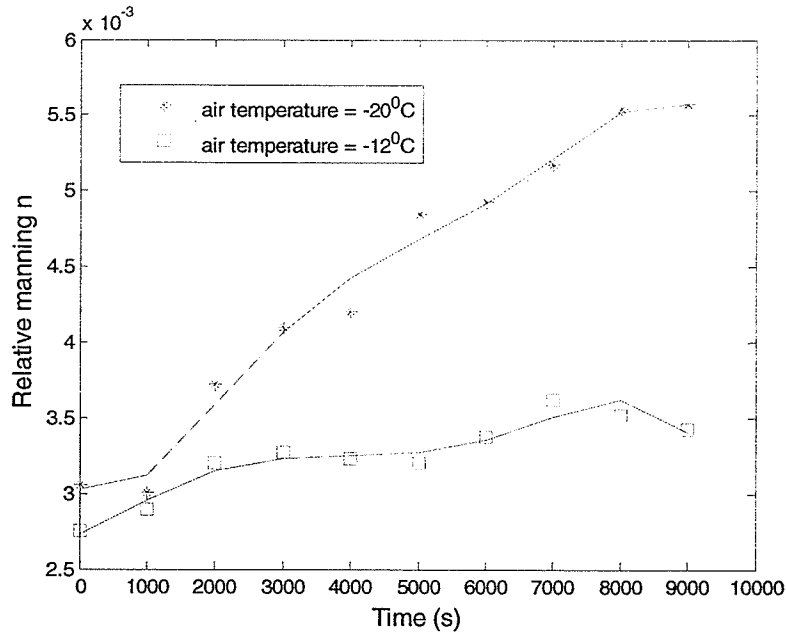


(a)

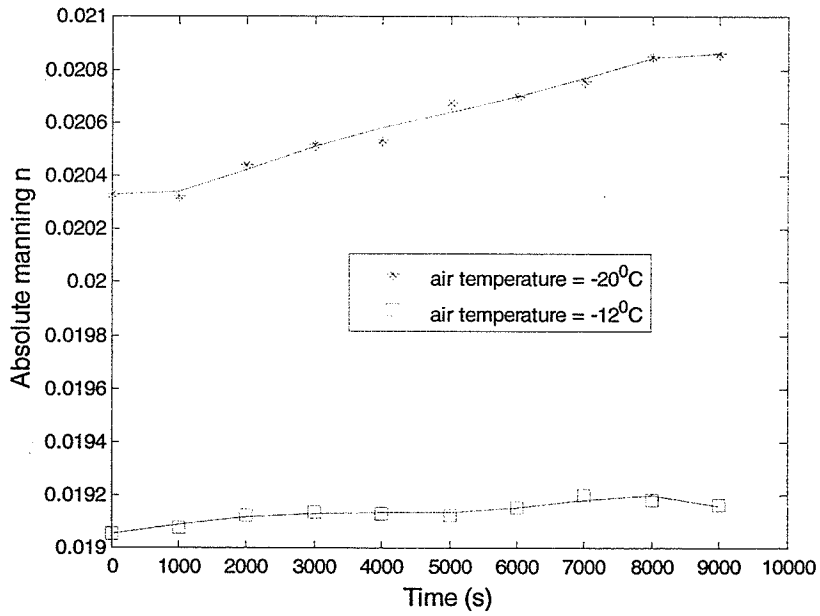


(b)

**Figure 4.9(a)** The relative Manning's 'n', and **(b)** The absolute Manning's 'n' under different air temperature when the water depth is 8 cm, the gravel bed roughness is 1 cm, and the velocity is 0.38 m/s.



(a)



(b)

**Figure 4.10(a)** The relative Manning's 'n', and **(b)** The absolute Manning's 'n' under different air temperature when the water depth is 10 cm, the gravel bed roughness is 0.34 cm, and the velocity is 0.38 m/s.

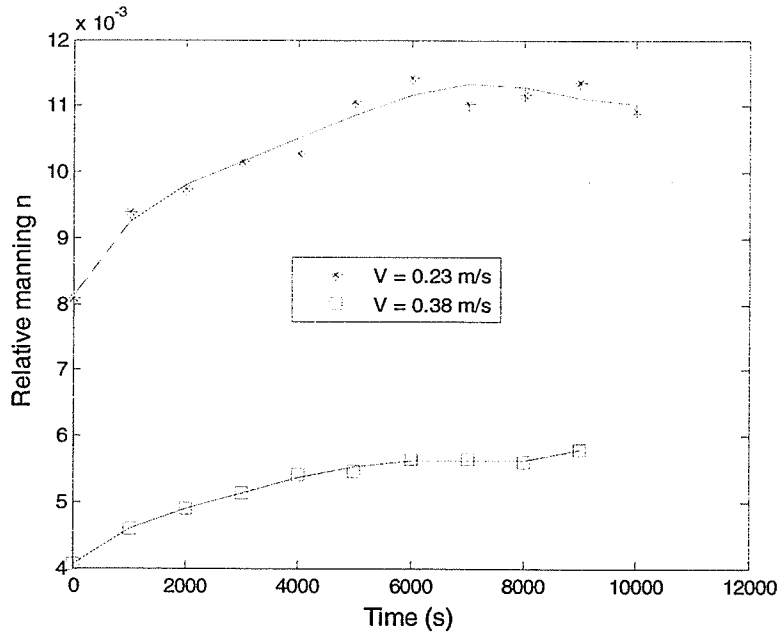


**Figure 4.11** The variation of the relative Manning's 'n' with the growth of anchor ice when the gravel bed roughness is 1 cm, the air temperature is -16°C and water depth is 8 cm.

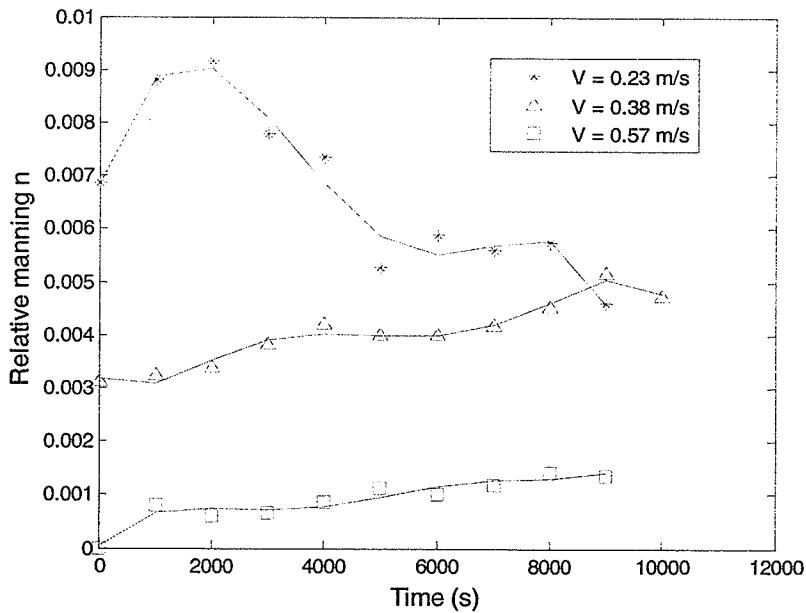


**Figure 4.12** The change of the relative Manning's 'n' with the growth of anchor ice when gravel bed roughness is 2 cm, the air temperature is -16°C and water depth is 10 cm.

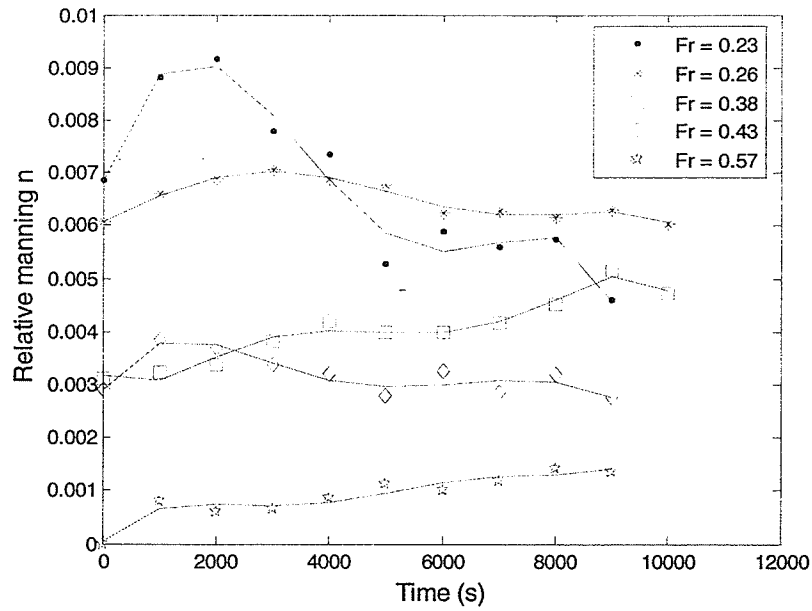


Figure 4.13 The effect of Froude number on the variation of the relative Manning's 'n'.

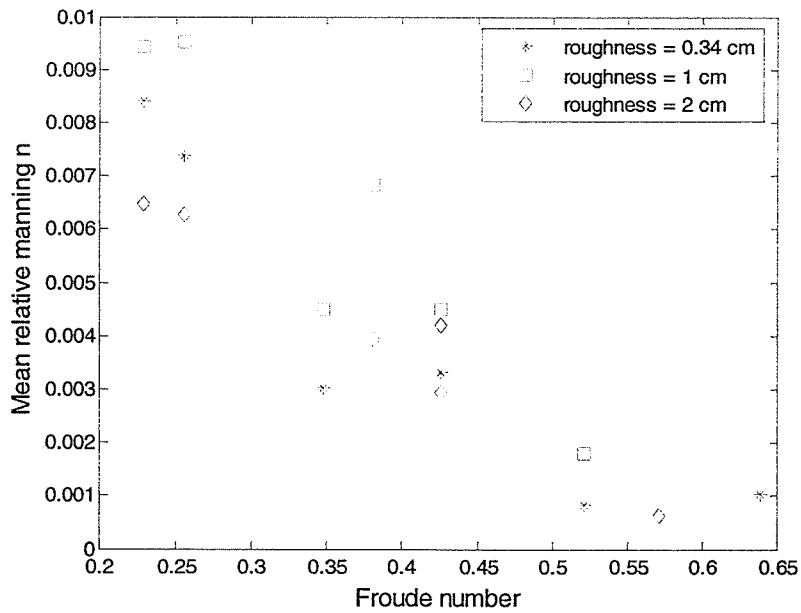


Figure 4.14 The effect of Froude number on the mean relative Manning's 'n'.

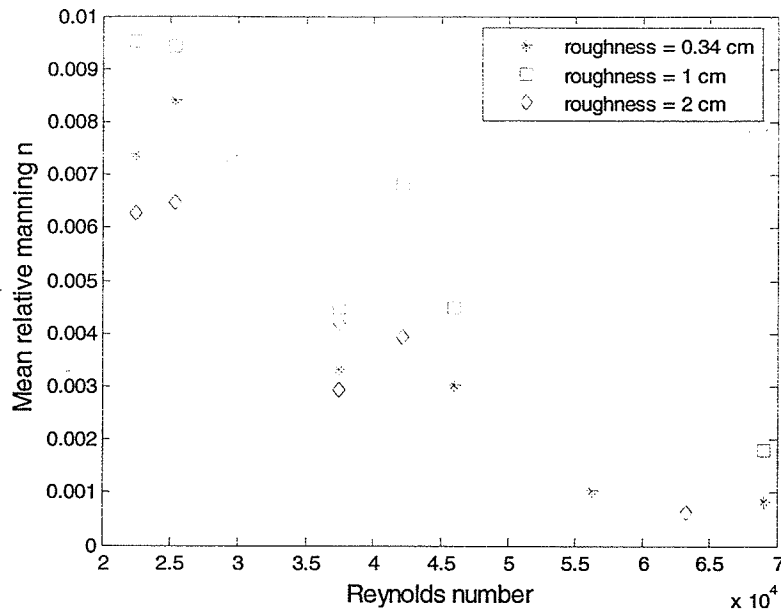


Figure 4.15 The effect of Reynolds number on the mean relative Manning's 'n'.

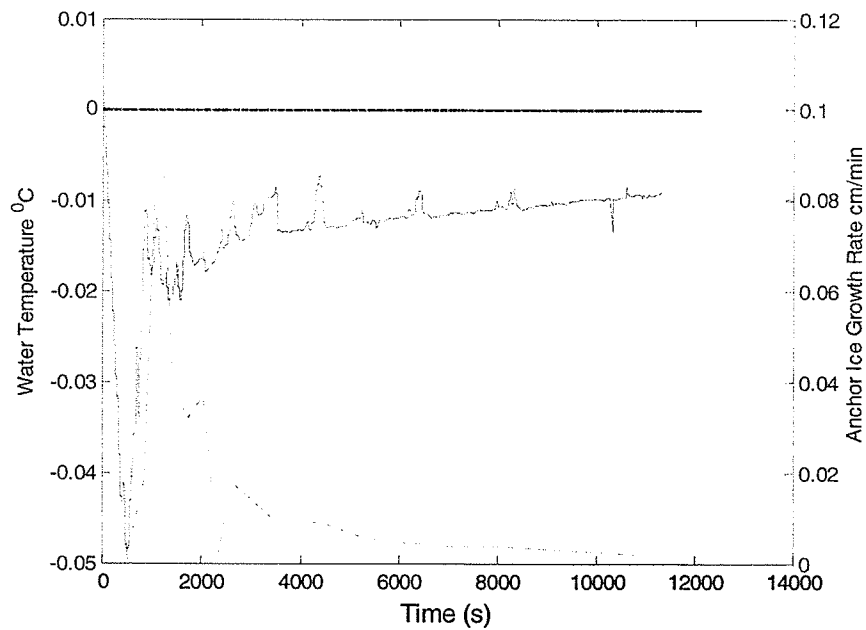
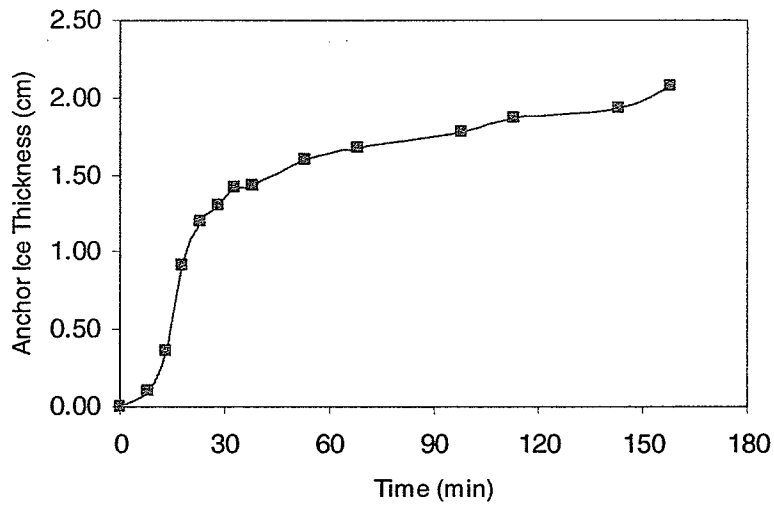
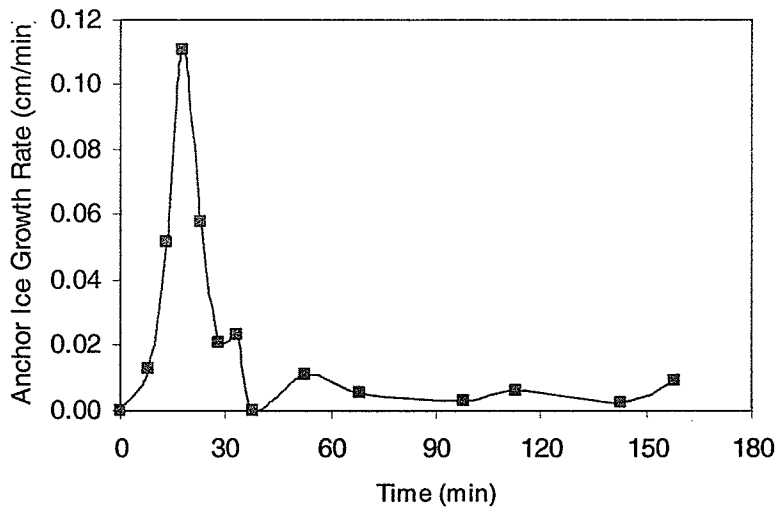


Figure 4.16 Supercooling curve with superimposed growth rate of anchor ice.

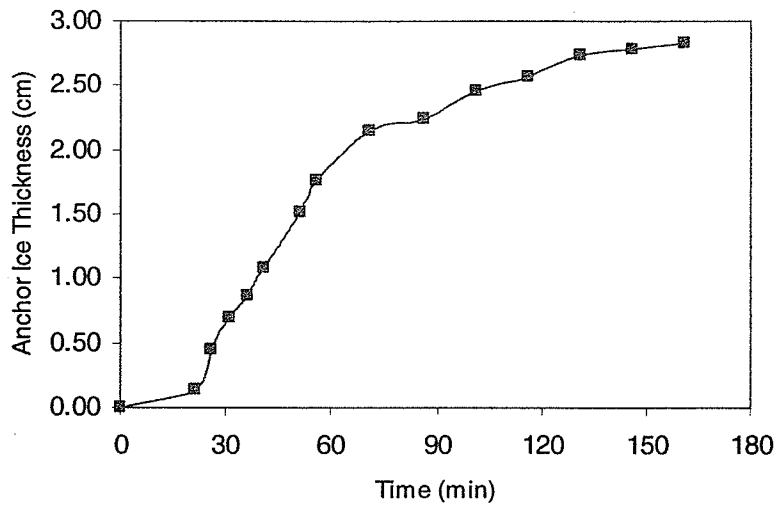


(a)

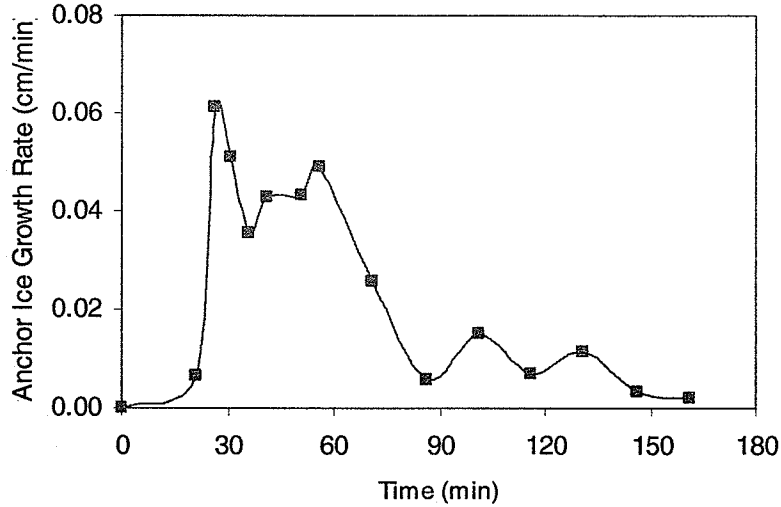


(b)

**Figure 4.17(a), (b)** Anchor ice thickness and growth rate when the water depth is 10 cm, the roughness height is 0.34 cm, the flow velocity is 0.38 m/s and the air temperature is  $-16^{\circ}\text{C}$ .

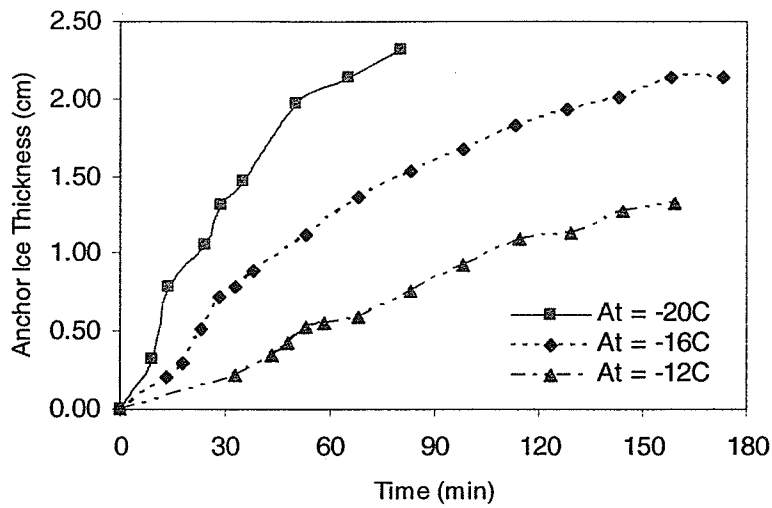


(a)

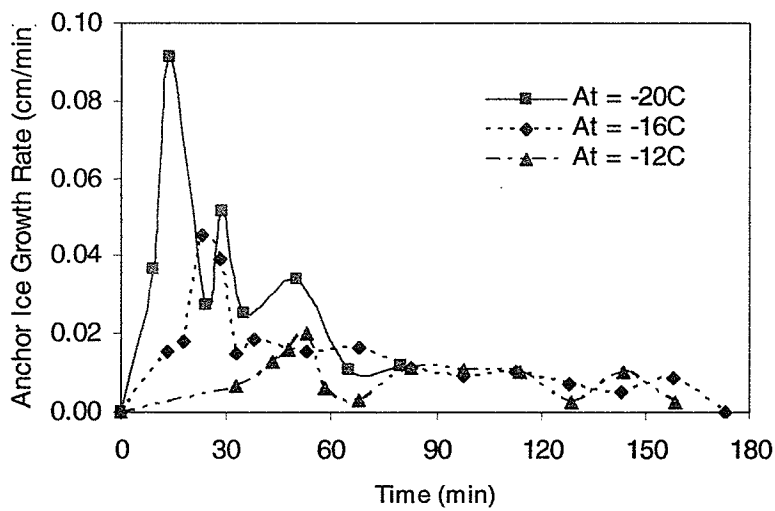


(b)

**Figure 4.18(a), (b)** Anchor ice thickness and growth rate when the water depth is 8 cm, the roughness height is 0.34 cm, the flow velocity is 0.23 m/s and the air temperature is  $-16^{\circ}\text{C}$ .



(a)



(b)

**Figure 4.19(a) and (b)** The thickness and growth rate of anchor ice under different air temperatures.

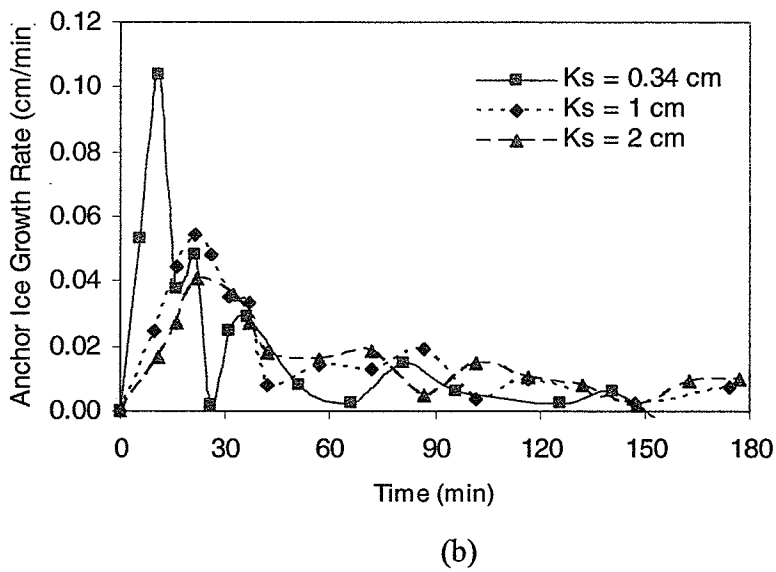
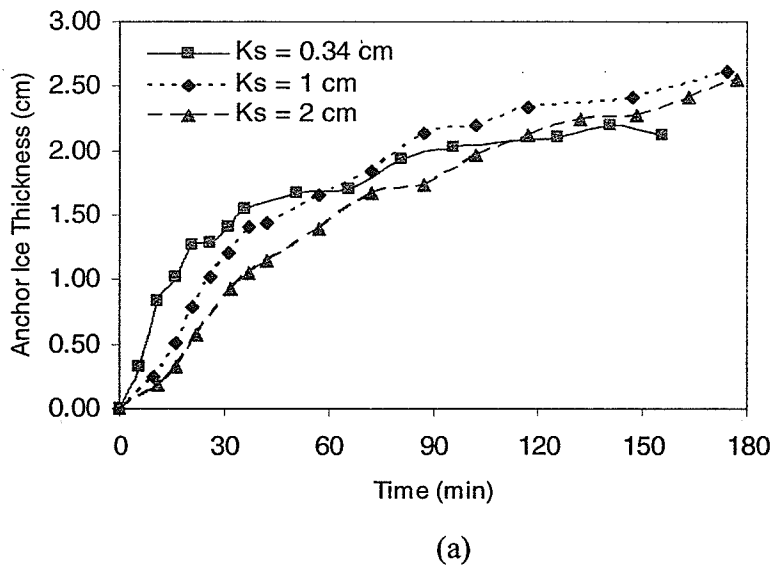


**Figure 4.20(a) and (b)** The thickness and growth rate of anchor ice under different roughness heights.



**Figure 4.21(a)** 30 minute after the appearance of frazil ice, the roughness height is 2 cm, the velocity is 0.38 m/s and the water depth is 0.08 m.

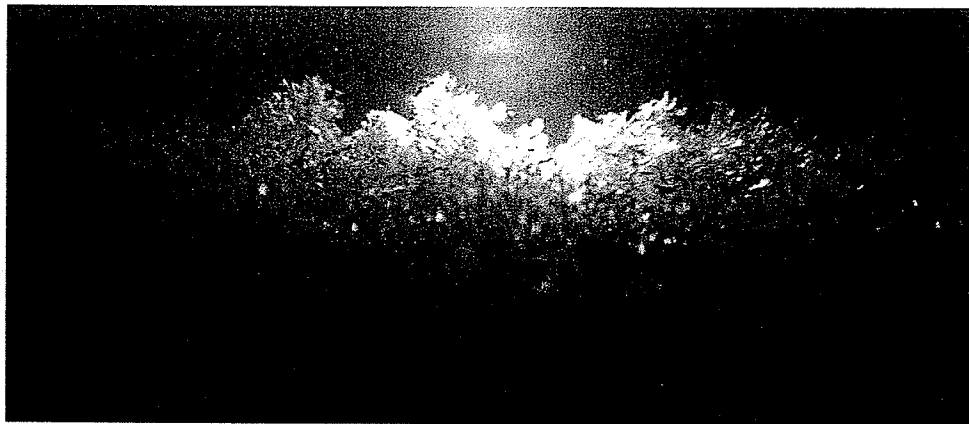
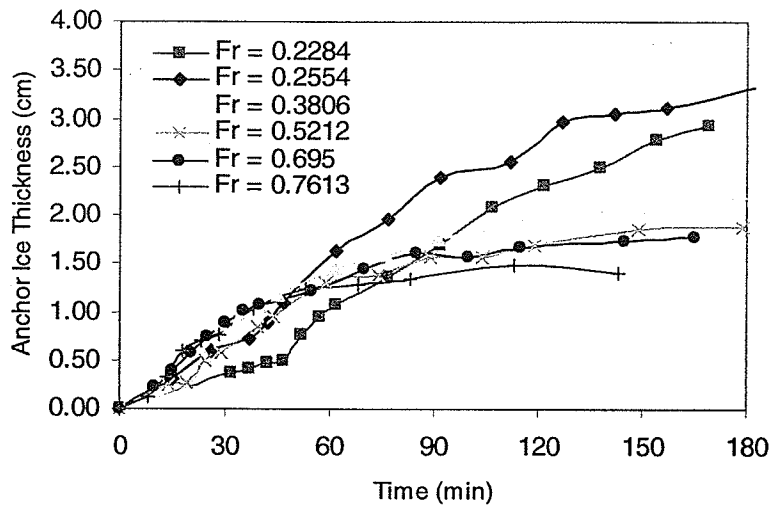
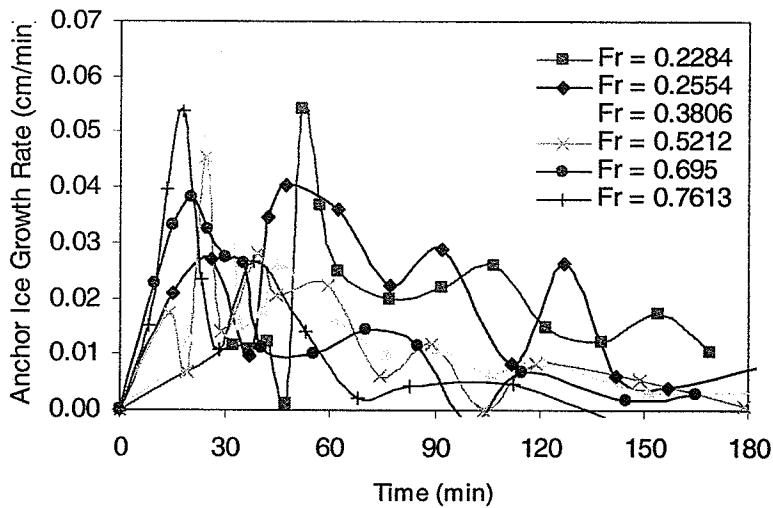


**Figure 4.21(b)** 30 minute after the appearance of frazil ice, roughness height is 0.34 cm, the velocity is 0.38 m/s and the water depth is 0.08 m.



(a)



(b)

Figure 4.22(a) and (b) The thickness and growth rate of anchor ice under different Froude numbers.

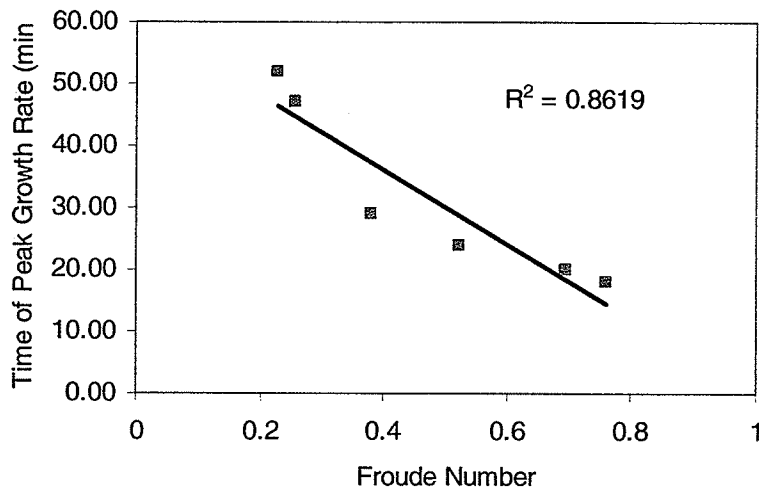


**Figure 4.23** Time of the peak growth rate of anchor ice under different Froude numbers.

# *Turbulence, Frazil ice Transport, and Deposition Theory*

---

Turbulence plays an important role in the process of frazil ice transport, anchor ice formation and growth. Therefore, it is necessary to introduce some important turbulence characteristics, turbulent structure and intensity, as well as the effect of roughness. In addition, frazil ice transport and deposition theories, which are the basis of the mathematical model formulated in chapter 6, are elaborated later in this chapter.

## **5.1 Turbulent Characteristics**

Turbulence is defined as irregular conditions of flow in which the various quantities show a random variation in time and space, so that statistically distinct average values can be observed. A central characteristic of turbulent motion is its ability to transport kinetic energy and contaminants such as heat and particles. This characteristic ensures that turbulence plays an important role in the formation and transport of frazil ice as well as in the growth of anchor ice.

Two important properties of turbulence, viz., shear velocity and eddy viscosity, which are related closely to frazil ice transport and deposition theory, are introduced hereinafter. In addition, the marked differences between the characteristics of turbulence on rough and smooth surfaces are discussed. The understanding of these differences is important, since field observations show that anchor ice formation is strongly related to bottom conditions.

### 5.1.1 Shear Velocity of Turbulent Flow

Shear velocity is considered to be the most fundamental velocity scale to normalize mean velocity and turbulence. Therefore, an accurate evaluation of the shear velocity is critical. It can be expressed by a measure of the shear stress and the velocity gradient near the boundary (Chanson, 1999)

$$u_* = \sqrt{\frac{\tau_0}{\rho}}, \quad (5-1)$$

where  $\rho$  is the fluid density and  $\tau_0$  is the boundary shear stress, which can be written as

$$\tau_0 = \frac{1}{2} C_d \rho U^2. \quad (5-2)$$

$C_d$  is the drag coefficient and  $U$  is the mean flow velocity. It is common practice to use Darcy's friction factor,  $f$ , which is related to the drag coefficient by  $f = 4C_d$ . This yields

$$\tau_0 = \frac{f}{8} \rho U^2. \quad (5-3)$$

Substituting  $\tau_0$  into equation (5-3), the shear velocity can be written as

$$u_* = \sqrt{\frac{f}{8}} U. \quad (5-4)$$

According to the Colebrook-White equation (Colebrook, 1939), the Darcy friction factor  $f$ , can be estimated as

$$\frac{1}{\sqrt{f}} = -2.0 * \log_{10} \left( \frac{k_s}{3.71 D_H} + \frac{2.51}{R_e \sqrt{f}} \right), \quad (5-5)$$

where  $k_s$  is a representative roughness height, and  $R_e$  is the Reynolds number.  $D_H$  is the hydraulic diameter, which for non-circular cross section channels can be defined as

$$D_H = \frac{4A_c}{P}, \quad (5-6)$$

where  $A_c$  is cross sectional area of the flow and  $P$  is the wetted perimeter.

### 5.1.2 Eddy Diffusivity of Turbulence

In most cases, for practical applications, it is useful to introduce an effective viscosity aimed at simulating the small scale dynamics of large scale flows. The eddy viscosity accounts for this affect and expresses the transfer of momentum from points where the momentum per unit volume is high to points where it is low. The eddy viscosity is given by

$$\nu_T = C_\mu \frac{k^2}{\varepsilon} = \kappa u_* (H - y) \frac{y}{H}, \quad (5-7)$$

where  $\kappa$  is the Karman constant,  $C_\mu$  is constant,  $\varepsilon$  is the turbulence dissipation rate,  $k$  is the turbulent kinetic energy,  $y$  is the vertical distance measured from the river bed and  $H$  is the water depth.

The expression above leads to  $v_T = 0$  at the free surface. However, due to surface renewal, one could reason that a non-zero downward mixing should exist at the free surface. According to Coleman (1970), eddy viscosity is better estimated by a semi-parabolic profile. When  $y/H < 0.5$ , the eddy viscosity is expressed as,

$$v_T = \kappa u_* (H - y) \frac{y}{H}. \quad (5-8)$$

When  $y/H > 0.5$ ,  $v_T \approx 0.01$ .

It is important to consider the difference between the fluid eddy viscosity and the particle eddy viscosity, which would account for the effect of particle inertia. This effect is very pronounced for relatively large particles in close proximity to the wall. The particle eddy viscosity,  $v_p$ , can be determined from the fluid eddy viscosity and the particle Schmidt number

$$v_p = \frac{v_T}{S_{cp}}, \quad (5-9)$$

where  $S_{cp}$  is the Schmidt number, which can be written as (Im and Chung, 1983)

$$S_{cp}^{-1} = 1 + \frac{\exp\left(-\frac{\tau_f}{\tau_p} + 1\right) - 1}{1.72 \left[ \left( \frac{\tau_f}{\tau_p} \right)^2 - 1 \right]}. \quad (5-10)$$

$\tau_f$  is the turbulence time scale defined as

$$\tau_f = \frac{24\nu}{0.4u_*^2}. \quad (5-11)$$

$\tau_p$  is the relaxation time introduced when the particle is not small and does not immediately react to flow field fluctuations, i.e.,

$$\tau_p = \frac{\rho_p d_p^2}{18\mu}, \quad (5-12)$$

where  $\nu$  is the fluid kinematic viscosity,  $\mu$  is the fluid dynamic viscosity,  $\rho_p$  and  $d_p$  are the density and diameter of the particle, respectively.

### 5.1.3 Problems with Rough Surface

For a turbulent flow along a smooth boundary, the velocity distribution follows (Schlichting, 1979):

$$\text{i) viscous sublayer: } \frac{u}{u_*} = \frac{u_* y}{\nu}, \quad \frac{u_* y}{\nu} < 5 \quad (5-13)$$

$$\text{ii) turbulent zone: } \frac{u}{u_*} = \frac{1}{\kappa} \ln\left(\frac{u_* y}{\nu}\right) + D_1, \quad 30 \text{ to } 70 < \frac{u_* y}{\nu} \text{ and } \frac{y}{\delta_b} < 0.1 \text{ to } 0.15 \quad (5-14)$$

$$\text{iii) outer region: } \frac{u_{\max} - u}{u_*} = -\frac{1}{\kappa} \ln\left(\frac{y}{\delta_b}\right), \quad \frac{y}{\delta_b} > 0.1 \text{ to } 0.15 \quad (5-15)$$

where  $u$  is the velocity at a distance  $y$  measured normal to the boundary,  $\delta_b$  is the boundary layer thickness,  $u_{\max}$  is the maximum velocity at the outer edge of the boundary

layer,  $\kappa$  is the von Karman constant ( $\kappa=0.4$ ) and  $D_1$  is a constant ( $D_1=5.5$ ; Schlichting, 1979).

In the case of rough beds, however, the turbulent structure is quite different and there are two questions that need to be addressed: one is the equivalent sand roughness  $k_s$  and the other is the theoretical wall level, i.e., where is the effective location of  $y=0$ ?

Starting with the question of the equivalent sand roughness, for a rough bed composed of uniform sand grains attached densely to the wall, it is found that the sand diameter itself can be used as an equivalent sand roughness  $k_s$ . For most roughness, the equivalent sand roughness  $k_s$  can be determined from the friction law derived from the log-law of velocity. For other roughness elements, the value of  $k_s$  can be determined from the mean velocity distribution in the region where it coincides with the log-law of the wall region.

The effects of roughness elements are usually classified in three categories (Nezu, 1993):

- a) hydraulically smooth bed ( $k_s^+ < 5$ ),
- b) incompletely rough bed ( $5 \leq k_s^+ \leq 70$ ), and
- c) completely rough bed ( $k_s^+ > 70$ ),

where

$$k_s^+ = k_s / (v/u_*). \quad (5-16)$$

If the bed is hydraulically smooth, the roughness effects will be insignificant because of the viscous sublayer. In contrast, on a completely rough bed, the viscous effects will disappear because the roughness elements penetrate the fully turbulent logarithmic layer

and the effect of roughness is significant. An incompletely rough bed will be affected by both viscosity and roughness.

As for the second question about the theoretical wall level, there is no widely accepted standard yet. The theoretical wall level can be set at a  $\delta$ -position that is below the top of the roughness elements (see Figure 5.1). In physical applications, the value of  $\delta$  should be at some intermediate point in the range of  $0 < \delta < d_s$ . The experimental data pertaining to  $\delta/d_s$  leads to slightly different results depending on the researchers. For example,  $\delta/d_s = 0.18$  (Grass, 1971),  $\delta/d_s = 0.27$  (Blinco and Partheniades, 1971),  $\delta/d_s = 0.25$  (Nakagawa et al., 1975) and  $\delta/d_s = 0.45$  (Wood, 1981). Therefore, the range of  $\delta/d_s$  is about 0.15-0.45, which is a gross standard for sand-grain roughness.

#### **5.1.4 Effect of Roughness on Turbulent Intensity**

There are limited data of turbulence intensity for rough beds compared to that for smooth beds. Grass (1971) measured the effect of roughness on the turbulence intensities using a hydrogen-bubble technique, and the results show that when  $y/H > 0.3$ , the roughness has almost no effect on turbulence intensities. Near the bottom where  $y/H \leq 0.3$ , the effect of roughness is clearly discernible. Raupach (1981) indicated that the effect of roughness elements on turbulence occurs primarily near the wall for boundary-layer flows and he called this region the 'roughness layer'. It is concluded that the value of  $u'/u_*$  decreases gradually with increasing roughness, while  $v'/u_*$  increases a bit as the roughness size increases although the tendency is not so strong.  $u'$ ,  $v'$  and  $w'$  are the

universal expressions of the three components of turbulence intensities, which are commonly normalized by the friction velocity (i.e.,  $u'/u_*$ ,  $v'/u_*$  and  $w'/u_*$ ) and are expressed as a function of  $y^+$ . Note that  $y^+$  is a function of  $y/H$ .

## 5.2 Frazil Ice Transport and Deposition Theory

Transport and deposition theories are the most useful tools in dealing with frazil and anchor ice problems. As with many cases of sediment transport, which have been studied widely, frazil ice transport and deposition are closely connected to turbulence.

### 5.2.1 Basic Principle

It is well-known that turbulence is generated at the boundaries, either at the free surface or the bottom or both. An important property of turbulence is it can be diffused. As it diffuses from the boundaries, energy is dissipated in overcoming viscosity according to the theory of turbulent diffusion.

For a river, if surface wind drag is negligible, turbulence is only produced at the bottom. As the turbulence diffuses upward towards the surface, it is dissipated. For a deep river, a vertical velocity fluctuation  $v'$  could be reduced to a negligible value before reaching the surface. In such a case, the supercooled water will not be brought down to the lower layers and the ice formed will only be that of a surface ice. On the other hand, if the river is sufficiently shallow so that the value of  $v'$  is still appreciable at the river's surface, then eddies at the surface will bring supercooled water down and so the whole river is capable of producing frazil ice. Frazil particles tend to float to the surface because of buoyancy, but turbulence can entrain them near the bottom. Thus a certain frazil

distribution will be established at equilibrium with the concentration of frazil ice decreasing in the downward direction. Furthermore, the highly adhesive frazil ice near the bottom may also stick to the bed material and form anchor ice.

### 5.2.2 Introduction of Transport Equation

The transport equation in turbulent flows is of fundamental importance in many disciplines. The transport of frazil ice suspended or entrained in supercooled water is similar to the transport of sediment in alluvial rivers except that the density of frazil ice is less than that of water. Hence, frazil ice particles have a significant rise velocity, although they can also be transported to a considerable depth in the river because of the effects of eddy mixing associated with turbulence. The transport mechanism is explained hereinafter.

Consider a small control volume as shown in Figure 5.2. The three sides have lengths  $dx$ ,  $dy$  and  $dz$ , respectively. The area of the face normal to the  $x$ -axis is  $dydz$ ; the area of the face normal to the  $z$ -axis is  $dx dy$ ; and the area of the face normal to the  $y$ -axis is  $dx dz$ .

According to Fick's law, the flux  $Q$  across a membrane of unit area, of a component of concentration  $C$ , is proportional to the concentration differential across that plane and is expressed as

$$Q = -v_p \frac{\partial C}{\partial x}. \quad (5-17)$$

In a period of time,  $dt$ , the convection and diffusion flux into the control volume along the  $x$ -axis and are written, respectively, as

$$Cudydzdt, \tag{5-18}$$

and

$$-v_p \frac{\partial C}{\partial x} dydzdt. \tag{5-19}$$

The convection and diffusion flux out of the control volume can be expressed as

$$\left( Cu + \frac{\partial Cu}{\partial x} dx \right) dydzdt, \tag{5-20}$$

and

$$-\left\{ \left( v_p \frac{\partial C}{\partial x} + \frac{\partial}{\partial x} \left( v_p \frac{\partial C}{\partial x} \right) dx \right) \right\} dydzdt. \tag{5-21}$$

The net accumulation in the control volume due to movement parallel to the  $x$ -axis is equal to the difference of the inflow and the outflow, expressed as

$$\frac{\partial}{\partial x} \left( Cu - v_p \frac{\partial C}{\partial x} \right) dx dydzdt. \tag{5-22}$$

Since there are flow components along all three axes, similar terms can be determined for the other two directions, i.e.,

$$\frac{\partial}{\partial y} \left( Cv - v_p \frac{\partial C}{\partial y} \right) dx dydzdt, \tag{5-23}$$

and

$$\frac{\partial}{\partial z} \left( Cw - v_p \frac{\partial C}{\partial z} \right) dx dydzdt. \tag{5-24}$$

Then the change of concentration  $C$  during a period  $dt$  can be written as

$$\left( \frac{\partial C}{\partial t} \right) dx dydzdt. \tag{5-25}$$

Let the increment due to physical and chemical change in the control volume be expressed by a source term  $\Gamma_r$ .

From conservation, the concentration change in the control volume is equal to the sum of the difference between the inflow and outflow and any incremental effect due to physical and chemical change. So the transport equation can be written (in tensor form) as

$$\frac{\partial C}{\partial t} + \frac{\partial}{\partial x_i} (Cu_i) = v_p \frac{\partial^2 C}{\partial x_i^2} + \Gamma_r \quad \text{where } i = 1, 2, 3. \quad (5-26)$$

Substituting a general physical item  $\bar{\Gamma}$  with concentration  $C$ , the general form of the transport equation is expressed as

$$\frac{\partial \bar{\Gamma}}{\partial t} + \bar{u}_j \frac{\partial \bar{\Gamma}}{\partial x_j} = \frac{\partial}{\partial x_j} \left( v_p \frac{\partial \bar{\Gamma}}{\partial x_j} \right) + \Gamma_r. \quad (5-27)$$

### 5.2.3 Rise Velocity of Frazil Ice

The rise velocity of frazil ice is an important parameter that has to be considered in frazil ice transport and deposition processes. In water at rest, a suspended frazil ice particle will rise because of its lighter density. The terminal rise velocity is the particle velocity at equilibrium, i.e., the sum of the gravity, buoyancy, and fluid drag forces equals zero.

The buoyant force  $F_b$  of a frazil disc can be expressed as

$$F_b = \rho_w g V_i = \rho_w g \frac{\pi d_f^2}{4} d_e, \quad (5-28)$$

and the gravity force on the disc is

$$\rho_i g V_i = \rho_i g \frac{\pi d_f^2}{4} d_e. \quad (5-29)$$

If it is assumed that the frazil discs have a preferred orientation in the flow (i.e., in a plane normal to the flow), the drag force can be described as

$$f_d = 0.5 C_d \rho_w w_b^2 A_p, \quad (5-30)$$

where  $V_i$  is the volume of frazil disc,  $d_f$  is the frazil disc diameter,  $d_e$  is the frazil disc thickness, and  $A_p$  is the projected area of a frazil disc. By equating the buoyancy force to the gravity and drag forces, we get

$$0.5 C_d \rho_w w_b^2 A_p + \rho_i g V_i = \rho g V_i. \quad (5-31)$$

If the Reynolds number is above  $10^3$ , the drag coefficient will reach a limiting value of about 1.1. Rearranging equation (5-31), taking into account the assumption that the aspect ratios (ratio of diameter and thickness) for frazil discs is about 1:10, the rise velocity can be written as

$$w_b^2 = \frac{2g(1 - \frac{\rho_i}{\rho})d_e}{C_d} = \frac{g(1 - \frac{\rho_i}{\rho})d_f}{5C_d}. \quad (5-32)$$

$d_f$  is the mean face diameter of frazil particles and  $t$  is the thickness of ice disc.

In addition, laboratory tests have been conducted to examine the rise velocity of frazil ice particles. On the basis of a force balance, Gosink and Osterkamp (1982) gave the terminal velocity,  $w_b$ , as

$$w_b = \left[ \frac{2g'd_e}{C_d} \right]^{1/2}, \quad (5-33)$$

where  $g' = g(1 - \rho_i / \rho)$ ,  $g$  is acceleration due to gravity, and  $C_d$  is the drag coefficient. The data they presented included both quiescent laboratory water columns and agitated water columns in the field. All of these data are comparable.

Andreasson (1998) gave the rise velocity for a spherical ice particle of diameter  $d_f$  as

$$w_b = 0.2g(1 - \rho_i / \rho)^{0.72} \frac{d_f^{1.18}}{\nu^{0.45}}. \quad (5-34)$$

Daly (1984) reviewed the rise velocity of frazil ice discs and noted the following:

In the Stoke's range of flow,  $r_f < 0.03$  cm

$$w_b = 0.08(g'\nu^{-1}r_f^2), \quad (5-37)$$

whereas for intermediate range,  $0.03 < r_f < 0.14$  cm

$$w_b = 0.16(g'^{0.715} \nu^{-0.428} r_f^{1.14}), \quad (5-38)$$

In fully turbulent flow,  $r_f > 0.14$  cm,

$$w_b = 0.707(g'r_f)^{1/2}, \quad (5-38)$$

where  $r_f$  is the radius of a frazil ice particle, and  $g'$  is the reduced gravity taken as  $133.7$  cm/s<sup>2</sup>. The rise velocity was estimated by assuming that a frazil disk rises steadily with its axis perpendicular to the vertical. This may be an overestimation of the rise velocity.

## 5.2.4 Deposition Theory

Understanding the mechanisms by which dispersed particles in a turbulent stream of fluid are transported towards the solid walls forming the flow passage, and predicting the rate

of deposition are both scientifically interesting and of engineering importance. When a turbulent flow with solid particles takes place near a solid wall, turbulence is the most important mechanism of particle deposition. Of course, there are also some additional mechanisms involved in the deposition process, such as Brownian diffusion (in the case of submicron particles) and gravitational settling (in the case of heavy particles deposited on horizontal surfaces). Furthermore, when the boundary is rough, the rough elements provide an additional mechanism for removal of particles from the turbulent stream.

There are two main approaches to the problem of particle deposition onto a rough surface. One approach is based on the derivation of the 'effective stopping distance', defined by Friedlander and Johnstone (1957) as the distance a particle travels in free flight through a fluid due to its initial velocity until stopping. The other approach is defined as a two-stage process for particle deposition, which consists of turbulent diffusion from the turbulent core to the roughness layer and that of deposition inside it; this will be used in the present model, and will be introduced later in chapter 6.

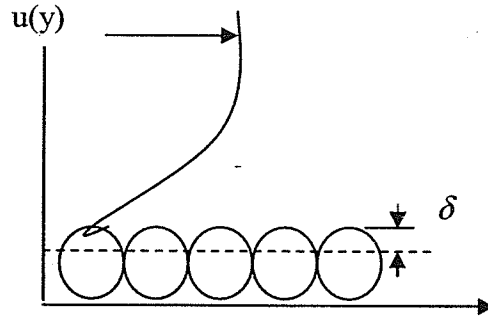


**Figure 5.1** Schematic description of turbulent flow on roughness surface.

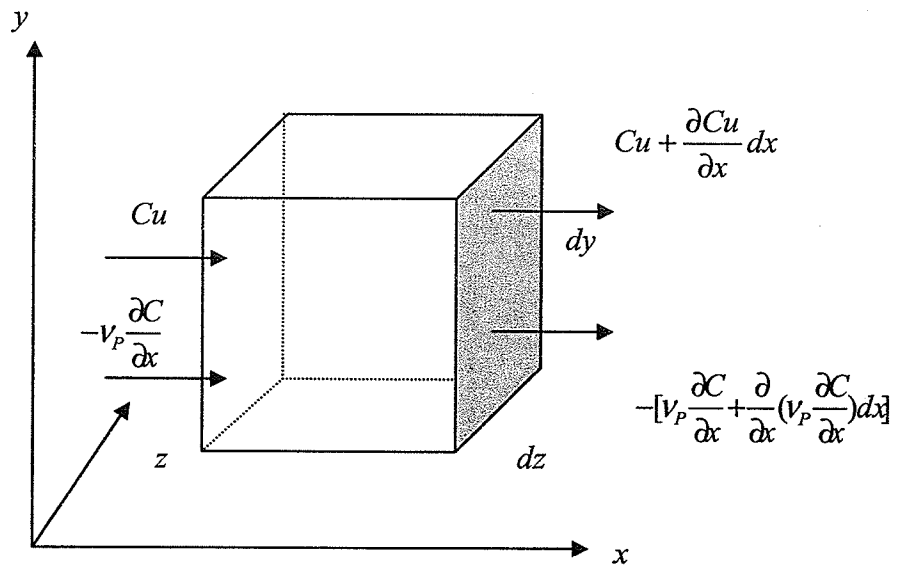


**Figure 5.2** The control volume of water body.

A mathematical model using the two-stage method (mentioned in Chapter 5) was developed to simulate the process of frazil ice transport and deposition to form anchor ice. As we observed in the experiments, anchor ice is mainly formed by frazil ice attachment. Heat transfer between supercooled water and ice crystals also exists according to the analysis of the measured water temperature curves. Therefore, both frazil ice attachment and heat transfer were considered in the model. Four governing equations were formulated and solved by a fourth-order Runge-Kutta numerical method. The vertical distribution of frazil ice and the growth rate of anchor ice under different hydro-meteorological conditions can be obtained by solving the governing equations. In addition, the different release mechanisms of anchor ice are introduced at the end of this chapter.

## **6.1 Heat Exchange Between Ice and Supercooled Water**

It is important to consider the thermal growth of frazil ice and anchor ice in the numerical simulation of frazil ice transport and deposition. Under the conditions that anchor ice

forms, there are two types of heat exchange between the ice crystals and the surrounding supercooled water: one is between the suspended frazil ice and the surrounding supercooled water and the other is between the anchor ice and the supercooled water.

### 6.1.1 Heat Transfer between Frazil Ice and Supercooled Water

In this section, expressions regarding the heat transfer between suspended ice crystals and the surrounding supercooled water will be formulated. The heat transfer between river water and suspended frazil ice depends on the water temperature and flow conditions, it can be written as (Omstedt, 1985)

$$q = \bar{h}(T_i - T_w), \quad (6-1)$$

where  $T_i$  is the ice surface temperature, taken as the freezing temperature,  $T_w$  is the water temperature,  $\bar{h}$  is the average convection heat transfer coefficient, which is defined as

$$\bar{h} = \frac{N_u k_w}{l}, \quad (6-2)$$

where  $l$  is a characteristic length. The ice particle thickness  $d_c$  is assumed to be the characteristic length, because ice particles grow mainly along the axial direction and thus forms discs.  $k_w$  is the thermal conductivity of water,  $N_u$  is the Nusselt number, which is defined by the turbulent Nusselt number,  $N_{uT}$ , multiplied by the term  $m^* = r/\eta$ , i.e.,  $N_u = N_{uT} m^*$  (Daly, 1984), where  $\hat{r}$  is the major linear dimension of frazil crystals, taken as the average radius,  $\eta$  is the dissipation length scale which is described as

$$\eta \approx (v^3/\varepsilon)^{1/4}, \quad (6-3)$$

$\varepsilon$  is the dissipation rate. The depth-averaged value is taken and expressed as (Mercier, 1984)

$$\bar{\varepsilon} \cong \frac{u_*^3}{\kappa H} \left( \ln \frac{u_* H}{\nu} - 1 \right), \quad (6-4)$$

where  $H$  is the water depth and  $\kappa$  is the von - Karman constant. Daly (1984) summarized the following relationships

$$N_{uT} = \left( \frac{1}{m^*} \right) + 0.17 P_r^{1/2} \quad \text{for} \quad m^* < \frac{1}{P_r^{1/2}}, \quad (6-5)$$

and

$$N_{uT} = \left( \frac{1}{m^*} \right) + 0.55 \left( \frac{P_r}{m^*} \right)^{1/3} \quad \text{for} \quad \frac{1}{P_r^{1/2}} < m^* < 10, \quad (6-6)$$

where  $P_r$  is the Prandtl number.

$$N_{uT} = 1.1 \left[ \left( \frac{1}{m^*} \right) + 0.8 \alpha_T^{0.035} \left( \frac{P_r}{m^*} \right)^{1/3} \right], \quad (6-7)$$

for  $m^* > 1$  and with a low intensity  $\alpha_T m^{*4/3} < 1000$ ,

and

$$N_{uT} = 1.1 \left[ \left( \frac{1}{m^*} \right) + 0.80 \alpha_T^{0.24} (P_r)^{1/3} \right], \quad (6-8)$$

for  $m^* > 1$  and with a high intensity  $\alpha_T m^{*4/3} \geq 1000$ ,

where  $\alpha_T = \sqrt{(2k/U^2)}$  is the turbulence intensity (Hammer and Shen, 1995).  $U$  is the mean flow velocity and  $k$  is the turbulent kinetic energy, which is taken as the depth-averaged value here and is determined in a way similar to that of  $\bar{\varepsilon}$

$$\bar{k} = \frac{1}{H} \int_0^H k(y) dy = 1.67 u_*^2. \quad (6-9)$$

Eventually the convection heat transfer per unit ice area can be finally written as

$$q = \frac{N_u k_w}{d_e} (T_i - T_w). \quad (6-10)$$

### 6.1.2 Heat Exchange Between Anchor Ice and Supercooled Water

The heat exchange between anchor ice and supercooled water is different from that of frazil ice. The heat flux from anchor ice to channel flow is expressed as  $q_a$  (Wang, 1993)

$$q_a = h_{awi} (T_i - T_w), \quad (6-11)$$

where  $T_i$  and  $T_w$  are the parameters as introduced in equation (6-1). For fully-developed turbulent flow,

$$R_e = \frac{UD_H}{\nu} > 2200. \quad (6-12)$$

The heat transfer coefficient for flow in non-circular (cross-section) channels are based on the hydraulic diameter, expressed as (Wang, 1993)

$$h_{awi} = 1118 \frac{u_*^{0.8}}{D_H^{0.2}}, \quad \text{for } T_w \leq 0^\circ C, \quad (6-13)$$

and

$$h_{awi} = 1448 \frac{u_*^{0.8}}{D_H^{0.2}}, \quad \text{for } T_w \geq 0^\circ C. \quad (6-14)$$

## 6.2 Model Formulation

According to the two-stage theory mentioned in Chapter 5, a numerical model of frazil ice transport and deposition on a rough bottom is developed in this section. The velocity distribution and frazil ice transport and deposition inside and outside the roughness layer can be simulated using the model. To obtain meaningful results it is very important to set

up appropriate assumptions when building a mathematical model. The assumptions used in the present model are as follows:

- i) the concentration of the frazil ice is low enough so as not to affect the flow field;
- ii) the interaction between frazil particles is negligible; and
- iii) the roughness elements penetrate the fully turbulent logarithmic layer, so that the viscous sublayer is negligible.

### 6.2.1 Velocity Distribution Outside the Roughness Layer

According to the results of Jackson (1981) the mean velocity distribution in the region outside the roughness layer is given by

$$\frac{u}{u_*} = \frac{1}{\kappa} \ln \frac{y-d}{y_0}, \quad (6-15)$$

where  $u$  is the velocity at a distance  $y$  from the boundary,  $d$  is the displacement height,  $y_0$  is the roughness length, and  $\kappa$  is the von Karman constant. The displacement height  $d$  and the roughness length  $y_0$  are related to the geometry of the bed roughness (Jackson 1981) by

$$d = k_s [1 - (1 - e^{-2\alpha}) / 2\alpha], \quad (6-16)$$

and

$$y_0 = k_s [(1 - e^{-2\alpha}) / 2\alpha e^{1/\alpha}], \quad (6-17)$$

in which  $\alpha$  is an attenuation coefficient.

### 6.2.2 Frazil Ice Transport Outside the Roughness Layer

According to the general transport equation derived in Chapter 5, the one-dimensional transport equation of frazil ice in the vertical direction can be written as

$$\frac{\partial C}{\partial t} + \frac{\partial}{\partial y} \left( v_p \frac{\partial C}{\partial y} \right) - w_b \frac{\partial C}{\partial y} + S_c = 0. \quad (6-18)$$

where  $C$  is the mean volumetric concentration of frazil particles,  $w_b$  is the buoyant velocity, and  $v_p$  is the turbulent diffusivity of the particles.  $S_c$  is the source term due to the thermal growth of frazil ice, which is derived by considering a unit volume with a mixture of water and frazil ice

$$S_c = 4Cq(d_f \rho_i L)^{-1}, \quad (6-19)$$

where  $d_f$  is the mean face diameter and  $L$  is the latent heat of ice.

In an area where anchor ice forms, there is no surface ice cover so the water remains supercooled. Eventually, a dynamic equilibrium condition will be reached. Experimental observations show that anchor ice is mainly formed during the dynamic equilibrium period. Therefore, an assumption that the concentration transport of frazil ice is time independent is made and so the time dependent term in the above equation vanishes. The transport equation of frazil ice outside the roughness layer can then be rewritten as

$$\frac{d}{dy} \left( v_p \frac{dC}{dy} \right) - w_b \frac{dC}{dy} + S_c = 0. \quad (6-20)$$

### 6.2.3 Velocity Distribution Inside the Roughness Layer

The commonly used logarithmic velocity profile inside the roughness layer is limited to the conditions where the bed roughness height is relatively small compared with the flow depth. However, for conditions where anchor ice forms, the flow depth is usually shallow with large roughness elements, so the logarithmic profile can not be simply used. Assuming homogeneity in the  $x$  and  $z$  directions in the flow field, the one-dimensional time-averaged Navier-Stokes equation for the  $u$  component can be expressed as

$$\frac{\partial}{\partial y}(-u'v') + \nu \frac{\partial^2 \bar{u}}{\partial y^2} = \frac{1}{\rho_w} \frac{\partial \bar{P}}{\partial x}, \quad (6-21)$$

where  $y$  is the vertical space coordinate positive upwards,  $\bar{P}$  is the average pressure,  $\bar{u}$  is the time-averaged velocity components of  $u$ , and  $u'$  and  $v'$  are the turbulent fluctuations.  $\rho_w$  is the fluid density.

The left-hand side of the above equation can be identified as  $\frac{\partial \tau}{\partial y}$  and the right-hand side as the total drag force per unit volume of the water  $f_D$ , where  $\tau$  is the local shear stress.

Hence, the equation can be written as

$$\frac{\partial \tau}{\partial y} = \frac{1}{2} \rho C_d u^2 / k_s, \quad (6-22)$$

where  $k_s$  is roughness height and  $C_d$  is the drag coefficient.

The shear stress  $\tau$  can be expressed in terms of an eddy viscosity, namely,

$$\tau = \rho \left( \nu \frac{du}{dy} + \nu_T \frac{du}{dy} \right). \quad (6-23)$$

From boundary layer theory, the thickness of the viscous sublayer is

$$\delta_1 = 11.6 \frac{\nu}{u_*} \quad (6-24)$$

For large roughness elements  $\delta_1 < k_s$ , the viscous sublayer is considered to be pierced through by the roughness elements and so the effect of the viscous sublayer is negligible. Under the conditions for which anchor ice forms, the roughness elements are typically much higher than the viscous layer, so the viscous term can be ignored in equation (6-23) and the shear stress  $\tau$  may be considered to be composed only of the Reynold stress term, i.e.,

$$\tau = \rho \nu_T \frac{du}{dy} \quad (6-25)$$

So, equation (6-22) can be rewritten as

$$\frac{\partial}{\partial y} \left( \nu_T \frac{\partial u}{\partial y} \right) = \frac{1}{2} C_d u^2 / k_s \quad (6-26)$$

The boundary conditions are as follows:

when  $y = k_s$ ,  $u = u_{k_s}$ , and when  $y = 0$ ,  $u = 0$ .

$u_{k_s}$  is the velocity at the edge of the roughness layer and can be determined by the logarithmic velocity distribution outside the roughness layer.

## 6.2.4 Transport and Deposition Inside the Roughness Layer

Anchor ice grows as a result of the deposition of frazil ice inside the roughness layer and the growth of deposited ice particles due to heat exchange. So inside the roughness layer

the situation is more complicated. The deposition item and the heat exchange item have to be taken into account in a traditional transport equation.

The transport equation inside the roughness layer is thus transformed to

$$\frac{d}{dy} \left( v_p \frac{dC}{dy} \right) - w_b \frac{dC}{dy} + S_c - S_y = 0. \quad (6-27)$$

Assuming the removal rate of frazil ice particles by the roughness elements is proportional to the local particle concentration, then the deposition term  $S_y$  is written as

$$S_y = \beta C(y)u(y) / D_x, \quad (6-28)$$

where  $D_x$  is the bed gravel diameter in the stream-wise direction. Substituting  $S_y$  and  $S_c$  into equation (6-27), we have

$$\frac{d}{dy} \left( v_p \frac{dC}{dy} \right) - w_b \frac{dC}{dy} + \left( \frac{4q}{d_f \rho_i L} - \frac{\beta u}{D_x} \right) C = 0. \quad (6-29)$$

The deposition coefficient  $\beta$  is related to the size, density and removal efficiency of the roughness elements. It also varies with the growth and release of anchor ice. Currently, no theoretical method exists to accurately evaluate  $\beta$ . It is quantified by well-planned laboratory experiments in the present model.

### 6.2.5 Boundary Conditions

The boundary conditions for the frazil ice concentration transport equations outside and inside the roughness layer are as follows. The frazil ice concentration is zero at the river

bottom (Hammar et al., 1996), and at the surface the frazil ice concentration is a function of Reynolds number (Ye et al., 2004). Mathematically this is represented by

$$C = 0 \quad \text{at } y = 0 \quad \text{and} \quad C = C(R_e) \quad \text{at } y = H.$$

### 6.2.6 Average Growth Rate of Anchor Ice

The frazil ice concentration inside the roughness layer actually governs the deposition rate. The total deposition rate over the depth of the roughness layer is written as

$$S_* = \int_{0.55k_s}^{k_s} S_y = \int_{0.55k_s}^{k_s} \beta C(y) u(y) dy / D_x. \quad (6-30)$$

Considering both the deposition of frazil ice and the turbulent heat exchange between the supercooled water and the existing anchor ice, the growth rate of anchor ice thickness can be expressed as

$$\frac{dh_a}{dt} = \frac{1}{1 - e_a} \left[ S_* + \frac{q_a}{\rho_i L} \right], \quad (6-31)$$

where  $dh_a/dt$  is the growth rate of anchor ice, and  $e_a$  is the porosity of anchor ice which has already been determined by experimental data.  $q_a$  is the heat flux from the ice to channel flow (see Section 6.1.2), and  $L$  is the latent heat of ice.

All of the governing equations were solved by a fourth-order Runge-Kutta numerical method (see appendix A for details). Different numbers of elements were tried to divide the flow depth. In order to get the most accurate results while using the least nodes possible, 19 elements (20 nodes) were chosen to divide the flow depth. The flow chart of the process is shown in Figure 6.1.

### 6.3 Result Discussion

Table 6.1 summarizes the flow conditions and the average growth rate of anchor ice from physical tests and numerical models. Here,  $G_{re}$  is the experimental results of the average anchor ice growth rate,  $G_{rt}$  is the theoretical results of anchor ice growth rate and the other symbols are the same as introduced previously.

**Table 6.1** Summary of the flow conditions and anchor ice growth rate.

Test No.	$V$ [m/s]	$H$ [m]	$k_s$ [m]	$A_t$ [°C]	Cooling rate [°C/s]	$F_t$	$R_e$	$G_{re}$ [m/s] $\times E(-6)$	$G_{rt}$ [m/s] $\times E(-6)$	%Diff.
2-23	0.38	0.1	0.01	-16	-	0.38	42171	1.77	2.17	23
3-3	0.57	0.1	0.01	-16	-0.0001	0.57	63257	1.75	1.43	18
3-9	0.38	0.12	0.01	-16	-0.0001	0.35	46004	2.1	1.44	31
3-12	0.57	0.12	0.01	-16	-0.00008	0.52	69007	1.75	0.88	50
3-18	0.38	0.08	0.01	-16	-0.0001	0.43	37485	2.5	3.06	22
3-22	0.57	0.08	0.01	-16	-	0.64	56228	2.15	2.34	9
3-25	0.23	0.08	0.01	-16	-	0.26	22493	3	2.45	18
3-26	0.23	0.1	0.01	-16	-	0.23	25304	2.9	1.67	42
3-31	0.38	0.08	0.0034	-16	-	0.43	37485	2.27	2.15	5
4-2	0.57	0.08	0.0034	-16	-	0.64	56228	2.02	1.97	2
4-6	0.38	0.1	0.0034	-16	-0.0001	0.38	42171	2.18	1.41	35
4-7	0.57	0.1	0.0034	-16	-0.0001	0.57	63257	1.85	1.23	34
4-21	0.23	0.08	0.02	-16	-	0.26	22493	2.55	2.88	13
4-23	0.57	0.08	0.02	-16	-	0.64	56228	2.12	2.1	1
4-26	0.38	0.1	0.02	-16	-	0.38	42171	2.33	2.18	6
4-28	0.23	0.1	0.02	-16	-	0.23	25304	2.38	2.01	16
4-29	0.57	0.1	0.02	-16	-0.0001	0.57	63256	2.1	1.23	41
5-2	0.38	0.12	0.02	-16	-0.0001	0.35	46004	2.45	1.49	39
5-3	0.23	0.12	0.02	-16	-0.00006	0.21	27605	2.3	1.44	37

Note, - data not available due to intermittent submergence of the thermometer probe.

Table 6.2 lists the parameters and numerical results from Hammar and Shen's numerical model (1994). The air temperature and flow parameters were not explicitly given in their model, therefore, it is difficult to compare the present numerical results with Hammar and Shen's (1994) results. But it can still be seen that the growth rates of anchor ice from both numerical models are of the same order of magnitude for comparable Froude numbers.

**Table 6.2** Parameters and numerical results of Hammar and Shen's (1994) model

Flow depth [m]	Roughness [m]	Mean velocity [m/s]	Mean concentration	Surface eddy diffusivity	Ice growth rate [m/s] (E-6) (Hammar)
1	0.1	1.3	0.01	0.15	5.4
1	0.1	1.3	0.01	0.015	5.4
1	0.1	1.3	0.01	0.0015	5.4
1	0.1	1.3	0.01	0.15	4.7
1	0.1	0.69	0.01	0.15	1.56
1	0.1	0.69	0.01	0.15	0.83

### 6.3.1 Deposition Coefficient

The deposition coefficient is a complicated factor and can only be determined by well designed experiments. It has long been determined that the deposition coefficient has a close connection with flow parameters and the bottom roughness (Hammar and Shen, 1994). Since there were not enough data to statistically reflect the effect of bottom roughness on the deposition coefficient, only the relationship between the deposition coefficient and the flow Reynolds number is explored at different bottom roughness by

analyzing numerical results with corresponding experimental results. Figures 6.2(a) and (b) show the regression between the deposition coefficient and the flow Reynolds number when the bottom roughness is 1 cm and 2 cm, respectively. A linear fit with regression coefficients ( $R^2$ ) of 0.83 and 0.78 for bottom roughnesses of 1 cm and 2 cm, respectively.

### **6.3.2 Comparison of the experimental and theoretical results**

Once the anchor ice porosity (see chapter 4) and frazil ice deposition coefficient are determined, they were employed herein into the numerical model. Figures 6.3 and 6.4 show a simulated velocity and frazil ice concentration distribution, respectively, along the flow depth obtained from the numerical simulation.

The simulated average growth rates of anchor ice under different conditions are shown in Table 6.1 along with experimental results. The percent differences were calculated as well and listed in Table 6.1. The numerical and experimental results are shown according to the bottom roughness because the frazil ice deposition coefficient was determined for a different bottom roughness. Figure 6.5(a) shows the numerical and experimental results when the bottom roughness is 1 cm. Through statistical analysis, the coefficient of determination between the numerical and experimental results is about 0.61. The solid line in this figure indicates the 45 degree line where the numerical and experimental results would be coincident. For a roughness of 2 cm, the results are shown in Figure 6.5(b) and the coefficient of determination is about 0.73. It can be seen from the figures that the majority of results are under the 45 degree line, which means that for most of the tests, the numerical model slightly underestimates the average growth rate of anchor ice.

This might be explained by the following two reasons: first, the removal of surface ice during the physical tests could stimulate the formation of frazil ice, therefore, more frazil ice would be deposited to the flume bottom to increase the growth rate of anchor ice; second, the mathematical model developed was only a one-dimensional and time independent model and can only simulate the growth rate in one direction during the dynamic equilibrium period.

## **6.4 Release Theory of Anchor Ice**

Anchor ice release is a common phenomenon in nature. During a “warm” day or in a river with coarse sandy bottom, anchor ice is often seen floating on the surface. The release of anchor ice can be caused by several reasons as described in chapter 1 and different release mechanism have different numerical formulations.

### **6.4.1 Melting Release of Anchor Ice**

When anchor ice is initially formed, the bond between the anchor ice and the river bed material is quite strong because of the negative heat gain of the water. However, the bond is easily affected by the heat balance in the water. When it is sunny and the water is warmed above 0°C, the bond will be weakened by the positive heat gain to the water such that anchor ice can be easily dislodged.

It is assumed that the melting of the bond between the anchor ice and the bed material occurs when the water temperature rises above 0°C. The melting rate at the bottom surface of anchor ice can be expressed as (Wang, 1993)

$$\frac{dh_{mh}}{dt} = \frac{1}{(1 - e_a)\rho_i L} [h_{awi}(T_w - T_i) + \Phi_R], \quad (6-32)$$

where  $h_{mh}$  is the melting thickness, and  $\Phi_R$  is the short wave radiation at the bottom.

Under a clear sky  $\Phi_R = a - b(\phi - 50)$ , where  $a$  and  $b$  are constants and  $\phi$  is the latitude in degrees. When the water temperature is above  $0^\circ\text{C}$ , the heat transfer  $h_{awi}$  between water and anchor ice is defined by equation (6-14).

It is also assumed when  $h_{mh} > \delta_c$ , anchor ice will be released;  $\delta_c$  is the critical height at which anchor ice will be released.

#### 6.4.2 Buoyancy Release of Anchor Ice

Some anchor ice is released continuously even during the night time when the water is still supercooled. Released pieces often carry sediments because the buoyant force of the anchor ice overcomes the submerged weight of the bed particles and the anchor ice itself. This mostly happens in areas where the bed material is sand or light gravel. But it also has long been observed that large boulders can be easily floated by big pieces of released anchor ice.

According to the force balance, the expression of anchor ice released by buoyancy is written as

$$V_s(\rho_s - \rho) = (1 - e_a)(\rho - \rho_i)V_{ai}, \quad (6-33)$$

where  $V_s$  and  $\rho_s$  are the volume and density of bed materials respectively, and  $V_{ai}$  and  $\rho_i$  are the volume and density of anchor ice.

Assuming that the river bed is covered with a layer of round sediment particles of diameter  $d_s$ , and the particles are assumed to be non-cohesive, the valid area (shown by the shaded area in Figure 6.6) for anchor ice can be calculated as  $d_s^2$ . Then the expression above can be rewritten as

$$h_a < \frac{\pi}{6} \left[ \frac{\rho_s - \rho_i}{\rho - \rho_i} \right] \frac{d_s}{1 - e_a}, \quad (6-34)$$

where  $h_a$  is the thickness of anchor ice.

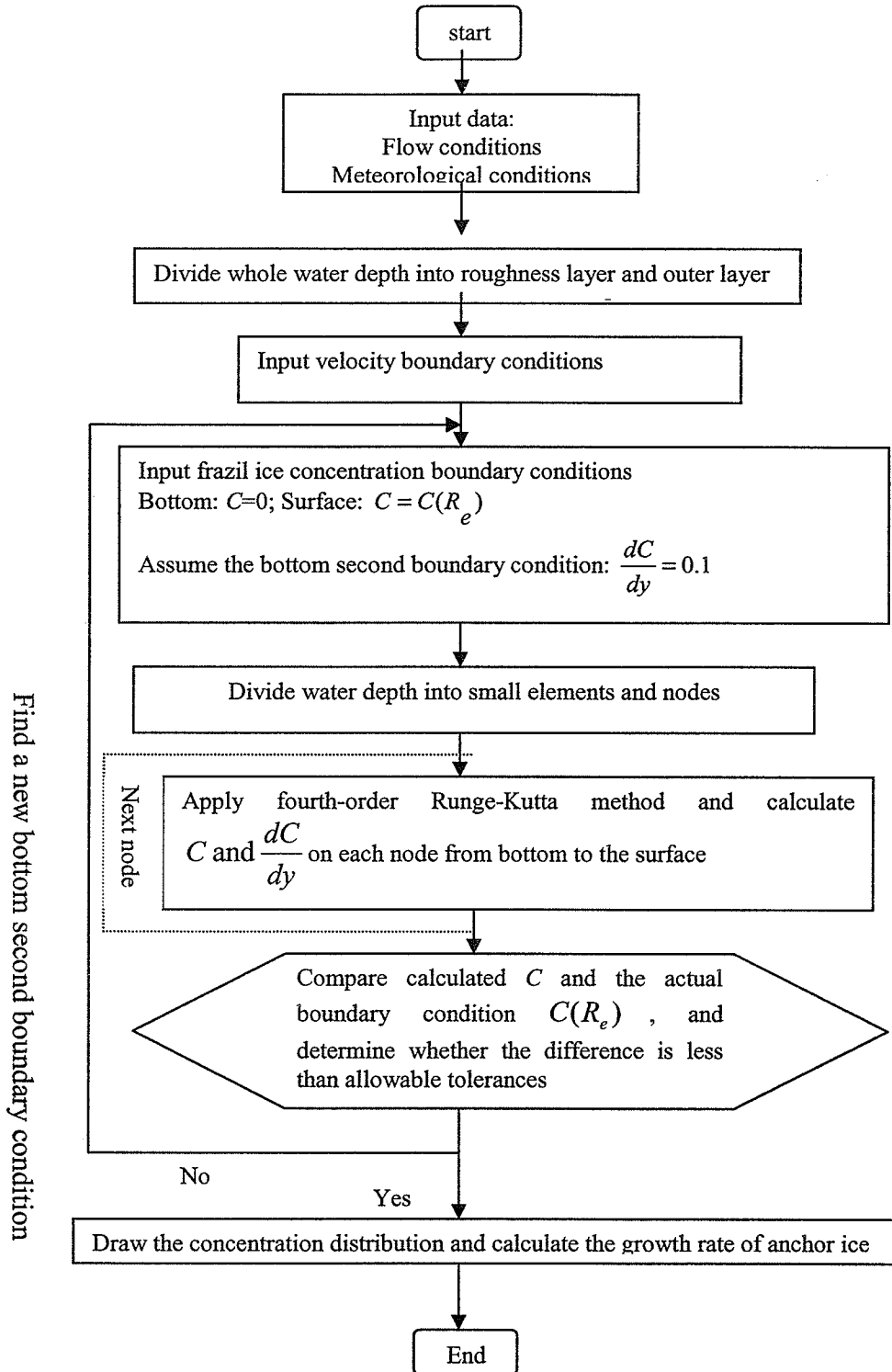
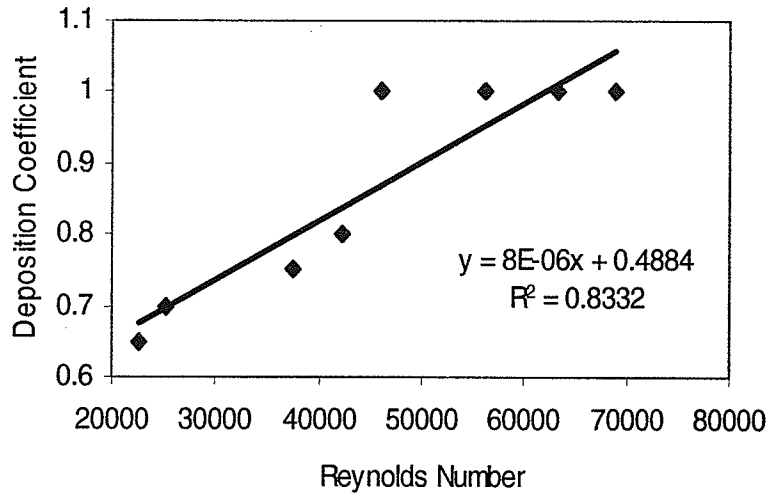
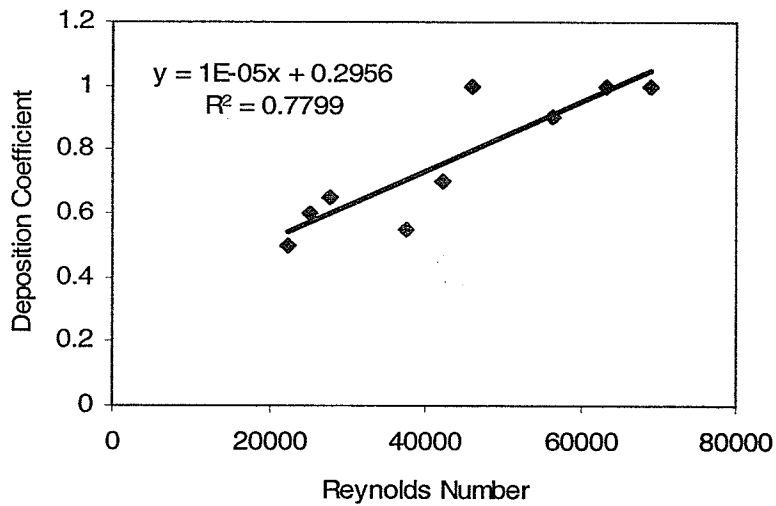


Figure 6.1 The flow chart of the process of solving the governing equations.

(a)



(b)



**Figure 6.2(a) and (b)** Relationship between the deposition coefficient and Reynolds Number when Roughness is 1 cm and 2 cm, respectively.

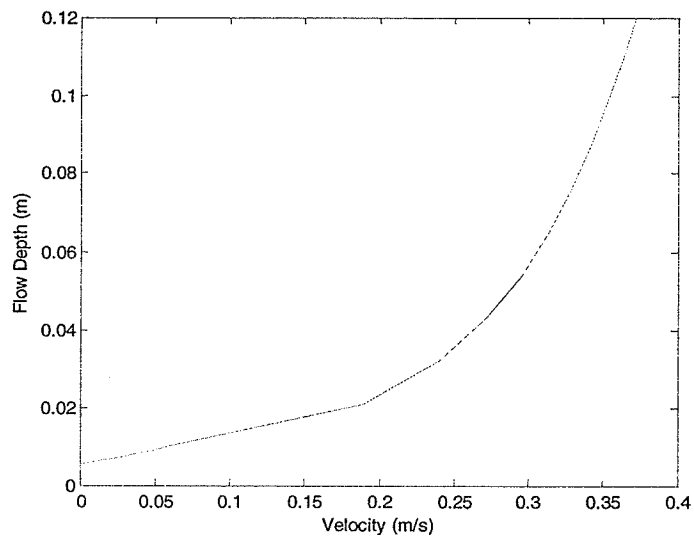


**Figure 6.3** Velocity distribution along the flow depth from the numerical model.

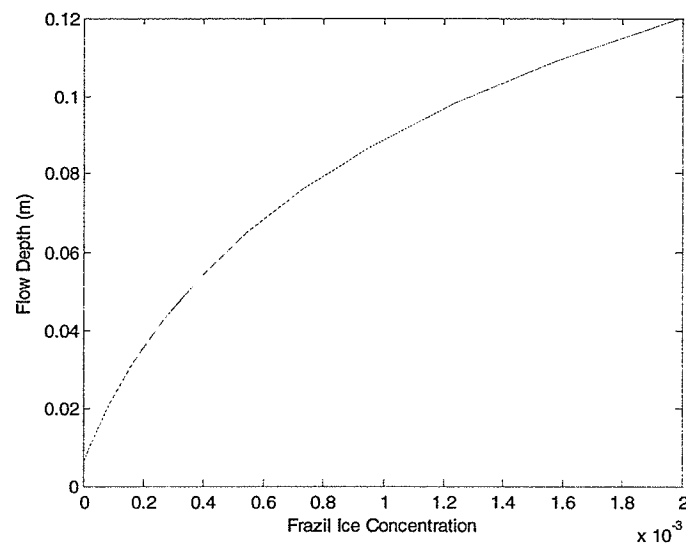


**Figure 6.4** Frazil ice concentration along the flow depth from the numerical model.

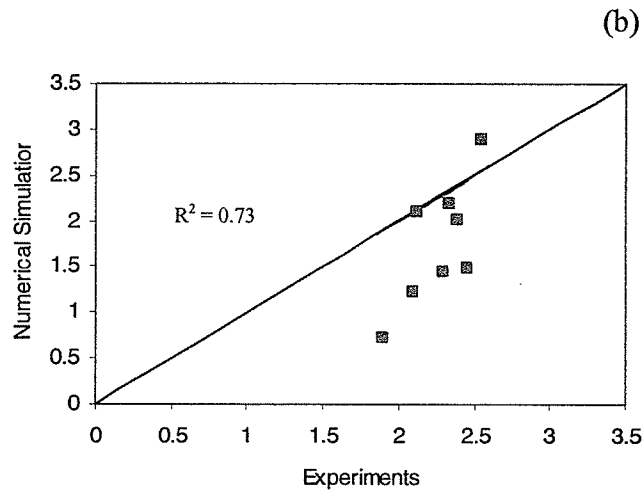
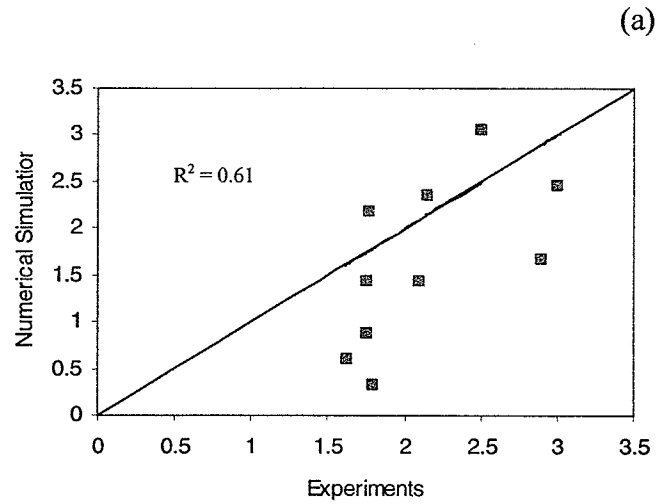


**Figure 6.5(a) and (b)** Comparison between experimental and numerical results for roughnesses of 1 cm and 2 cm, respectively.

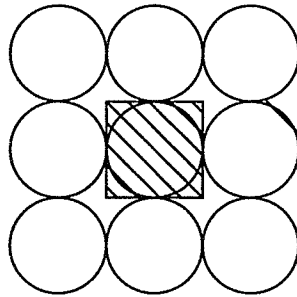


**Figure 6.6** Determination of valid area.

---

## **7.1 Introduction**

Anchor ice is a form of ice that attaches to the bed of a river, stream, or ocean. It has been observed in all types of rivers and in nearly all countries where surface river ice is formed. The formation of anchor ice can have serious physical as well as biological implications. It can cause significant discharge and water level changes, since it raises the effective bed elevation and alters the bed roughness. A local growth can choke off a large part of a discharge and resulting in financial losses for a hydro-power industry dependent on the flow. Anchor ice can also have serious effects on invertebrates and fish, since it can block the supply of oxygen into the sediments and dislodge fish eggs from spawning beds by scouring action during its release.

In spite of these significant effects, our knowledge of anchor ice processes is still quite limited; consequently, more study is needed. For the present study of anchor ice, laboratory experiments were conducted and a numerical model was developed to elucidate the mechanism of anchor ice formation and model its growth, respectively.

This study will help to develop better management strategies to mitigate anchor ice related complications that affect the operation of hydraulic structures in cold regions.

## 7.2 Summary

A series of experiments to investigate the mechanisms of anchor ice growth were carried out for different hydro-meteorological conditions. Different arrangements of rocks were setup on the bed of a counter-rotating flume to investigate the evolution of anchor ice growth around individual rocks before experiments of anchor ice growth on gravel beds were conducted. Experiments of anchor ice evolution around one rock (simplest case) were conducted first. Additional rocks were then added in the flow direction and across the flow direction to examine the evolution of anchor ice around these different arrangements. Eventually, and an essential part of this study, experiments of anchor ice evolution on uniformly distributed gravel beds were conducted. Three sets of uniformly distributed gravel beds of different roughness heights were used to investigate the growth mechanism of anchor ice on a gravel bed. Two digital cameras were used to monitor the evolution forms of anchor ice around the rocks and on gravel beds under different conditions. It was observed during the tests that anchor ice growth occurred mainly by frazil ice attachment.

A program coded in Matlab<sup>®</sup> was developed and employed to analyze the digital images of anchor ice collected during the tests. The digital image processing program used edge detection and morphological image processing techniques. The thickness of anchor ice was calculated as part of the image processing program.

The observed growth phenomenon of anchor ice around rocks was as follows. Starting with a single rock, there were two locations around a rock where frazil ice accumulation started. One was the front-face gap between the rock and flume bed and the other was the back-side gap. It was found that frazil ice accumulates faster in the front-face gap than in the back-side gap, and that virtually no growth occurred at the left and right sides of the rock. Once frazil ice attachment was initiated, it grew upward towards the free surface and extended in the upstream (front-face) and downstream (back-side) directions. Eventually with further frazil ice accumulation, the two growths of anchor ice grew up around the rock from both the front and back sides and joined each other to cover the top of the rock.

For a row of rocks along the axis of the flume, anchor ice first initiated in the front-face gap between the front rock and the flume bed. Almost simultaneously it started accumulating in the other four front-face gaps as well. Back-side accumulation was also observed, but it was not as significant as front-face accumulation. With the production of large amounts of frazil ice particles during the supercooling process, anchor ice accumulated and filled in the gaps between the rocks quickly. Once the anchor ice grew over the tops of the rocks, it was flattened by the drag force of the flow as it continued to accumulate. With continued accumulation, the anchor ice crept towards and eventually connected with the adjacent ice to form a narrow layer of anchor ice.

The growth mechanism of anchor ice on two rows of rocks across the flow direction (not contacting each other) was basically the same as that of the five rocks described above, namely, anchor ice started accumulating mostly in the front-face gaps but with a little accumulation in the back-side gaps. However, since the rocks were arranged side by side across the flow direction, anchor ice also grew sideways around the rocks because of the effect of the rock configuration on the flow field around the neighboring rocks. Thermal growth was also detected through the analysis of temperature curves recorded during the experiments, although it was not readily discerned from the digital images.

Anchor ice growth on uniformly distributed gravel beds was tested under different Froude numbers ranging from 0.22 to 0.64. The evolution forms were found to agree well with the study of Kerr et al. (2002). When the Froude number was between 0.22 and 0.5, a 'scale' type of anchor ice was observed after the initial frazil attachment. When anchor ice protruded above the crown of the gravel, it grew towards the downstream direction in a tail like shape due to the hydrodynamic drag of the flow. The short tail of this anchor ice growth was frequently broken off by the flow, which prevented the formation of long tails. When the Froude number was over 0.5, frazil ice accumulated on gravel beds in round lumps and is called ball shaped anchor ice. The ball shaped anchor ice grew not only in the downstream direction but also in the upstream direction. After it overgrew the gravel, it spread over the top of the gravel and gradually connected with other anchor ice pieces to form a thin blanket of anchor ice.

The effects of the gravel Reynolds number on the release and growth of anchor ice were also explored during the tests. It was observed that the gravel Reynolds number did not have a significant effect on the growth forms of anchor ice, but that it did have an obvious effect on the release of anchor ice. For experiments where the gravel Reynolds number was small, anchor ice was more easily dislodged by the flow than when the gravel Reynolds number was big. It appears that when the gravel Reynolds number was small, the bonding force between the anchor ice and the small sized bed gravel was not strong enough to hold the anchor ice to the bottom. Therefore, small pieces of anchor ice were frequently dragged away by the hydrodynamic action while big pieces of anchor ice were usually lifted up by the buoyant force.

Anchor ice density, an important parameter when studying anchor ice growth, was estimated by measuring the weight and volume of anchor ice during the tests. The densities found from the present tests ranged from 160 to 400 kg/m<sup>3</sup> and the average porosity of anchor ice was found to be about 73%, which is close to the 75.9% that Parkinson (1984) reported from his field observations in Lake St. Louis at Montreal. The relationship between the gravel Reynolds number and anchor ice porosity was explored and a best-fit linear regression was obtained with a regression coefficient ( $R^2$ ) of 0.81. As expected from experimental observation, the results show that anchor ice porosity decreases with increasing gravel Reynolds number. An analysis of the relationship between the Froude number and anchor ice density reveals that anchor ice density increases with increasing Froude number. The experimental results agree well with field observations, which indicate that anchor ice grows more densely and quickly in shallow

rapids where the Froude number is larger than in deep rivers where the Froude number is smaller.

It was observed that anchor ice grew the quickest during the peak production of frazil ice particles, which usually occurred during the first hour of each test. Therefore, in addition to the final thickness and growth rate of anchor ice, the periodical growth rate and the corresponding thickness of anchor ice were also calculated through the digital image processing program. The effects of air temperature, roughness height, and flow parameters on the growth of anchor ice were examined herein. The observations indicate that air temperature has a significant effect on the growth of anchor ice. When the air temperature was colder, anchor ice grew quicker and it took less time to reach the peak of the growth rate. This is consistent with the fact that when the air temperature decreases, the supercooling rate of the water increases and there are more frazil ice particles produced in supercooled water. As a result, more frazil ice will be entrained and carried to the flume bed by turbulence to accumulate as anchor ice. The thickness of anchor ice increased rapidly as more and more frazil ice attached to the flume bed and the peak growth rate was reached.

Three sets of gravel beds with different roughness heights (*i.e.*, 0.34 cm, 1 cm, and 2 cm) were used to test the effect of the bed roughness on the thickness and growth rate of anchor ice during the tests. It was observed that anchor ice on a gravel bed with small roughness grew the quickest at the initial growth stage. But as the process continued, the anchor ice on a gravel bed with larger roughness would eventually outgrow the anchor

ice with smaller roughness. It was also observed that with an increase in gravel bed roughness, the time from the first appearance of frazil ice particles to the peak of the growth rate was prolonged. In addition, different Froude numbers were used during the tests to explore the effect of Froude number on the growth of anchor ice. The results revealed that anchor ice grew more slowly when the Froude number was low than when the Froude number was higher, presumably because there is not enough turbulence in the water to entrain and carry frazil ice to the flume bed due to the low velocity associated with a low Froude number. It was also observed that at a later stage of a test, anchor ice subjected to a small Froude number environment outgrew that subjected to greater Froude numbers.

The effect of anchor ice growth on the gravel bed/ice surface roughness under different hydro-meteorological conditions was explored by using a pair of servo-motor systems that were capable of returning the torque load signals as a percentage of a full-scale torque load. The torque load signals collected during the tests were analyzed in the present tests and were found to match well with normal distributions. The Manning's 'n' was derived from the ice torque loads to indicate the change of bed/ice surface roughness. Similar to what Kerr et al. (2002) observed during his tests, the variation of Manning's 'n' was divided into three different stages. It was observed that 'n' increases at the beginning of a test when anchor ice was randomly spread over the gravel bed (the first stage). As the test progressed, the roughness value reached a peak; during this time the gaps between the gravel particles were gradually being filled in by frazil ice accumulation (the second stage). The actual gravel bed was then raised and smoothed by

continued frazil ice adhesion to the bottom, resulting in a gradual decrease in the roughness as the test progressed (the third stage).

The effects of air temperature, flow velocity, Froude number and Reynolds number on the bed/ice surface roughness were also examined. Three different air temperatures (-20°C, -16°C and -12°C) were applied during the tests. It was clear that the rate of change in Manning's 'n' increased with a decrease in air temperature. When the air temperature was -20°C, the slope of the roughness curve was steeper than when the air temperature was -12°C; the mean relative Manning's 'n' was also greater when the air temperature was -20°C than when the air temperature was -12°C.

Three different velocities were employed during the tests to explore the effect of flow velocities. It was observed that both the rate of change of Manning's 'n' and the mean relative Manning's 'n' increased for a decrease in the flow velocity. It was also clear that it took less time to reach the peak roughness when the velocity was lower. The variations of the relative Manning's 'n' with the growth of anchor ice under different Froude and Reynolds numbers were also examined in this study. It can be seen that with an increase in the Froude and Reynolds numbers, the mean relative Manning's 'n' decreases. This is consistent with the experimental images that indicate when the flow is more turbulent, frazil ice fills in the gaps between the gravel particles more quickly and evenly, which causes a smaller change in the bed/ice surface roughness..

A numerical model, based on mass conservation and a two-stage deposition theory, was developed to predict the growth rate of anchor ice. The model considered the growth of anchor ice as a combined process of frazil ice attachment to gravel beds as well as heat transfer between existing anchor ice and the surrounding supercooled water. Four governing equations related to the distribution of velocity and frazil ice transport and deposition inside and outside the roughness layers were built. A fourth-order Runge-Kutta numerical method was used and programmed in Matlab to solve the governing equations. The velocity and frazil ice concentration distributions inside and outside roughness layers were obtained by solving the governing equations. The average growth rates of anchor ice under different hydro-meteorological conditions were simulated by integration along the roughness layer. The numerical results of Hammer and Shen's model (1994) were introduced as a reference to the current model. The results showed that the growth rates of anchor ice from both models are of the same order of magnitude for comparable Froude numbers. A comparison of the experimental observations and numerical predictions yields coefficients of determination of 0.61 and 0.73 for bottom roughnesses of 1 and 2 cm, respectively.

An empirical formula for the deposition coefficient of frazil ice was developed during the tests. The (regression) relationship between the deposition coefficient and the flow Reynolds number for different bed roughnesses was examined by comparing the numerical and experimental results of anchor ice growth rates. A best-fit linear regression with an  $R^2$  of 0.83 and 0.78 was obtained for bed roughnesses of 1 and 2 cm, respectively.

### 7.3 Conclusions

The following conclusions can be drawn from this study.

- i) Anchor ice attachment to a single rock occurs (predominantly) in the front- and back-face gaps; front and back-face growth continues until the anchor joins on the top of the rock.
- ii) Anchor ice growth around a row of rocks (in the along or cross flow directions) occurs by attachment in the between rock gaps and proceeds up the front and back faces of the rocks until it joins on the top of the rocks. Further growth leads to a flattening of the anchor ice in the direction of flow.
- iii) Anchor ice growth over a uniform gravel bed leads to “ball” and “scale” formations. The type of formation depends on the Froude number of the flow.
- iv) The gravel Reynolds number is related to the release of anchor ice from a gravel bed. The larger the gravel Reynolds number the more difficult it is for anchor ice to release.
- v) Anchor ice densities in the tests ranged from 160 to 400 kg/m<sup>3</sup>. Anchor ice densities increase for an increase in Froude numbers.
- vi) Anchor ice porosity, which is strongly correlated with the gravel Reynolds number, decreases with increasing gravel Reynolds number. An average anchor porosity of 73% was observed.

- vii) Air temperature has a significant effect on the growth rate of anchor ice. Anchor ice growth is quicker for colder temperatures and takes less time to reach its peak growth rate.
- viii) Anchor ice grows faster, initially, on a “smooth” gravel bed than a “rough” gravel bed. Eventually the growth on the “rough” bed surpasses that of a smoother bed. Larger Froude numbers produce larger average growth rates.
- ix) The rate of change in Manning’s ‘n’ increased with a decrease in air temperature.
- x) Both the rate of change of Manning’s ‘n’ and the mean relative Manning’s ‘n’ increased for a decrease in the flow velocity. The mean relative Manning’s ‘n’ decreases with an increase in the Froude and Reynolds numbers.
- xi) The numerical model developed was able to reasonably predict the average growth rates of anchor ice under different hydro-meteorological conditions.
- xii) An empirical formula for the deposition coefficient of frazil ice was developed from the experimental and theoretical results.

## **7.4 Future Work**

The study of frazil ice distribution and anchor ice growth is a fairly new and undeveloped topic. Hereafter is some work that should be done for future research.

- i) The mathematical model is a one-dimensional model and only simulates the growth rate in one direction (vertical). The development of a two or three-

dimensional model is possible and would be important due to its ability to simulate the growth of anchor ice in the other two dimensions as well.

- ii) The mathematical model was not time dependent and only simulated the average growth rate during the dynamic equilibrium. The development of a model that predicts the complete growth process and as a function of time would be important for detailed anchor ice modeling.
- iii) A wider range of air temperature and bed roughness data (only three different air temperatures and roughnesses were used) should be examined.

---

## *References*

---

- Andreasson, P. Hammar, L. and Shen, H.T. 1998. The influence of surface turbulence on the formation of ice pans. 14<sup>th</sup> IAHR Symposium on ice, Potsdam, USA., 69-76.
- Arden, R.S. and Wigle, T.E. 1972. Dynamics of ice formation in the upper Niagara River. Proceedings of Banff Symposium on the role of Snow and Ice in Hydrology, Unesco-WMO-IAHS, Banff, Sep. Vol.2, pp1296-1312.
- Ashton, G.(ed), 1986. River and lake ice engineering. Water Resources Publication, Littleton, Colorado, pp. 282.
- Blinco, P.H. and Partheniades, E. 1971. Turbulence characteristics in free surface flows over smooth and rough boundaries. J. Hydraulic Research, IAHR, 9:43-69.
- Chanson, Hubert. 1999. The hydraulics of open channel flow. University of Queensland, Australia.
- Clark, S. and Doering, J., 2006. Isolating turbulence intensity as a testing variable for frazil ice research. Canadian Journal of Civil Engineering, submission number: 06-261.

- Colebrook, C.F. 1939. Turbulent flow in pipes with particular reference to the transition region between the smooth and rough pipe laws. *J. of the Institute of Civil Engineers*. No. 4, pp. 133-156.
- Coleman, N.L., 1970. Flume studies of the sediment transfer coefficient. *Water Res. Res.*, Vol.6, No. 3, 801-809.
- Daly, S.F. 1984. Frazil ice dynamics. CRREL monograph 84-1.
- Daly, S.F. 1994. Report on Frazil ice. USA Cold Regions research and Engineering Laboratory, Special Report 94-23.
- Devik, O., Kanavin, E.V., 1965. Final report on analysis and consideration of the ice conditions in the Hvita and Thjorsa river systems, Southern Iceland. State Electric Authority, Reykjavik.
- Doering, J.C., Bekeris, L.E., Morris, M.P., Dow, K.E., and Girling, W.C. 2001. Laboratory study of anchor ice growth”, *Journal of cold regions engineering*. Vol.15, No. 1, pp60-67.
- Doering, J. C. and Morris, M. P. 2003. A digital image processing system to characterize frazil ice. *Canadian Journal of Civil Engineering*. 30: 1-10.
- Friedlander, S.K. and Johnstone, H.F. 1957. Deposition of suspended particles from turbulent gas streams. *Ind. And Eng. Chem.* 49, 1151-1156.
- Girling, W.C., and Groeneveld, J., 1999. Anchor ice formation below Limestone Generating Station: A case study. *Proc 10th Workshop on River Ice, Winnipeg, MB*, 160-173.
- Gosink, J.P. and Osterkamp, T.E. 1982. Measurements and analysis of velocity profile and frazil ice-crystal rise velocity during periods of frazil –ice formation in rivers.

- Annals of Glaciology, International Glaciological Society, Proceedings of the second Symposium on Applied Glaciology, pp.79-84.
- Grass, A.J., 1971. Structural features of turbulent flow over smooth and rough boundaries. *J. Fluid Mech.*, Vol. 50, , 233-255.
- Hammar, L. and Shen, H.T. 1995. Anchor ice growth in channels. 8th workshop on river ice, Kamloops, BC. Pp.77-92.
- Hammar, L. and Shen, H.T. 1994. Anchor ice growth and frazil accretion. Proceedings of ice symposium, IAHR, Trondheim, pp.1059-1067.
- Hammer, L., Kerr, D. J., Shen, H.T., and Liu, L.. 1996. Anchor ice growth in gravel-bedded channels. 13th IAHR symposium on ice, Beijing pp.843-850.
- Im, K.H. and Chung, P.M., 1983. Particulate deposition from turbulent parallel streams. *AICHE J.*, 29, 498.
- Jackson, P.S. 1981. On the displacement height in logarithmic velocity profile. *J. Fluid Mechanics*, Vol III pp15-25.
- Kerr, K.J. 1997. An experimental study on anchor ice evolution. M.S. Thesis Department of Civil Engineering Clarkson University Potsdam N.Y.
- Kerr, D.J., Shen, H.T., and Daly, S.F. 2002. Evolution and hydraulic resistance of anchor ice on gravel beds. *Cold Regions Science and Technology*, 35, pp. 101-114.
- Kivisild, H.R. 1970. River and lake ice terminology. Proceedings, IAHR Symposium on Ice and Its Action on Hydraulic Structures, Lulea, 1-14.
- Marcotte, N. and Robert, S. 1986. Elementary mathematical modeling of anchor ice. Proc. Of IAHR Symposium on Ice, Iowa city, Iowa, 493-506.

- Mercier, S. 1984. The reactive transport of suspended particles: Mechanics and Modeling. Ph.D. dissertation, Joint Program in Ocean Engineering, Massachusetts Institute of Technology, Cambridge. MA.
- Michel, B, 1967. Morphology of frazil ice”, Proceedings of international conference in low temperature science. Hokkaido University, Sapporo, Japan, pp119-128.
- Morris, M. P., 2002. A digital image processing system for the characterization of frazil ice. M. Sc. Thesis, University of Manitoba.
- Nakagawa, H., et al. 1975. Turbulence of open channel flow over smooth and rough beds. Proc. of Japan Soc. Civil Engrs., 241:155-168.
- Newbury, R. 1968. A study of subarctic river processes, the Nelson River. Ph. D. Thesis, Johns Hopkins University.
- Nezu, I. and Nakagawa, H. 1993. Turbulence in open-channel flows. Monograph series, IAHR.
- Omstedt, Anders. 1985. On supercoolign and ice formation in trubulent sea-water. J. of Glaciology. Vol.31, No. 109.
- Ontario, Hydro, 1967. Study of river and lake ice-I.H.D. Project No.R-SIG-6 Ontario-27. Progress Report No.1, Niagara River ice, June, Contributors:Bryce,J.B. Arden, R.S., Wigle, T.E.
- Ontario, Hydro, 1968. Study of river and lake ice-I.H.D. Project No.C.6.7. Progress Report No.2, Niagara River ice, June, Contributors:Bryce,J.B. Arden, R.S., Wigle, T.E.

- Ontario, Hydro, 1969. Study of river and lake ice-I.H.D. Project No. C.6.7. Progress Report No.3, Niagara River ice, June, Contributors: Bryce, J.B. Arden, R.S., Wigle, T.E.
- Ontario, Hydro, 1970. Study of river and lake ice-I.H.D. Project No. C.6.7. Progress Report No.4, Niagara River ice, June, Contributors: Bryce, J. B. Arden, R.S., Wigle, T.E.
- Parkinson, F.E., 1984. Anchor ice effects on water levels. Proc. Workshop on the Hydraulics of River Ice, Fredericton, NB, 345-370.
- Raupach, M.R. 1981. Conditional statistics of Reynolds stress in rough-wall and smooth wall turbulent boundary layers. *J. Fluid Mech.*, 108:363-382.
- Schlichting, H. 1979. *Boundary layer theory*. 7<sup>th</sup> edition (McGraw-Hill: New York, USA).
- Terada, K., Hirayama, K., and Sasamoto, M., 1999. Field measurement of anchor and frazil ice. Proc. 14th IAHR Symposium on Ice, Clarkson University, Potsdam, N.Y., 697-702.
- Tesaker, E. 1994. Ice formation in steep rivers. *Proceeding of IAHR Ice Symposium 12th, Trondheim Vol.2*. pp. 631-638.
- Tsang, G. 1982. Frazil and anchor ice. NRC Subcommittee on Hydraulics of Ice Covered Rivers. Ottawa, Ontario, Canada.
- Tsang, G. 1988. A theory for frazil distribution in turbulent flow. *Proceedings of the 9th International Symposium on Ice*. International Association for Hydraulic Research, Sapporo, Japan, August 23-27, pp.152-169.

- Tsang, G. 1992. Laboratory investigation of frazil evolution, flocculation and the formation of anchor ice. Progress Report No.3, National Hydrology Research Institute, Environment Canada, Saskatoon, Sask., NHRI contribution No. CS-92057.
- Wang, D.S. and Shen, H.T. 1991. Frazil and anchor ice evolution in rivers. Proceedings, First national conference on ice engineering, Chinese hydraulic engineering society, Baode, pp. 115-127.
- Wang, D.S.,1993. A study on frazil and anchor ice processes and development of a river ice model. Ph.D. thesis, Clarkson University, Potsdam, NY, 228pp.
- Wood, N.B.1981. A simple method of the calculation of turbulent deposition to smooth and rough surfaces. *J. Aerosol Sci.* 12, 275-290.
- Ye, S.Q., Doering, J. and Shen, H.T. 2004. "A laboratory study of frazil evolution in a counter-rotating flume". *Canadian journal of civil engineering.* 31:899-914.

---

Appendix A

## *Calibration Curves of the Counter-rotating Flume*

---

The data presented in this appendix shows the calibration curves for the bed and wall velocities of the counter-rotating flume. Each experiment was designed to run at a calibrated bed and wall velocity, so that the shear force on the water would be balanced and the water would be stationary in an absolute frame of reference. Three water depths 8, 10, 12 cm and three bottom roughness 0.34, 1, 2 cm, were used in the experiments and the corresponding curves follow.

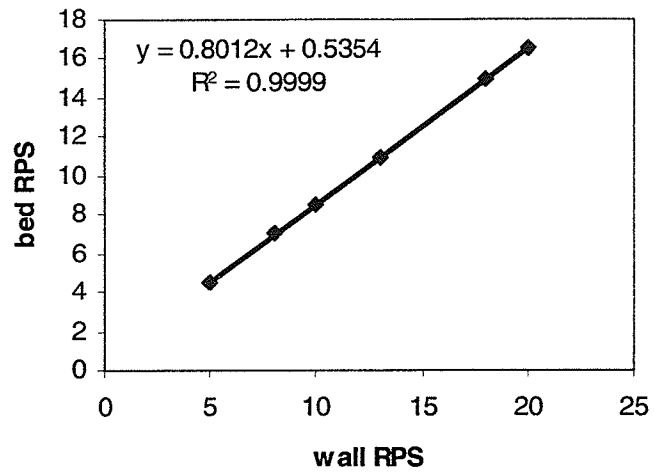


**Figure A1** Velocity calibration curve when bed roughness is 0.34 cm and water depth is 8 cm.

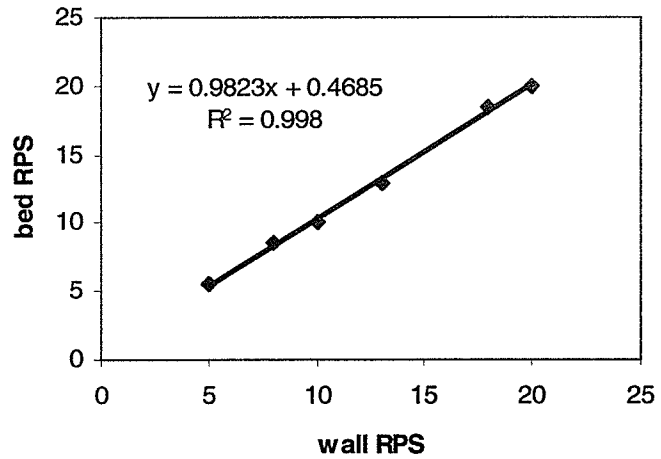


**Figure A2** Velocity calibration curve when bed roughness is 0.34 cm and water depth is 12 cm.

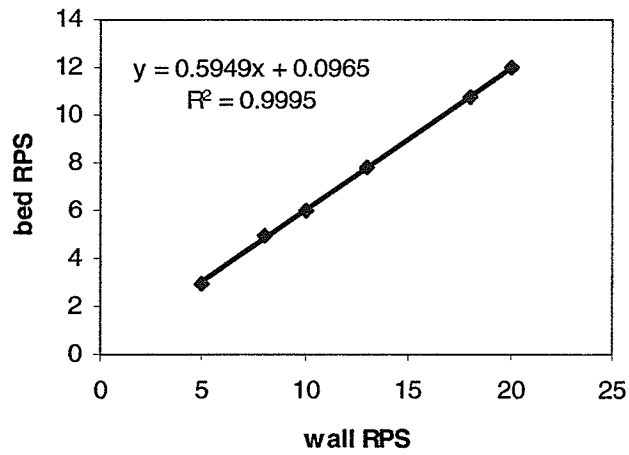


**Figure A3** Velocity calibration curve when bed roughness is 1 cm and water depth is 8 cm.

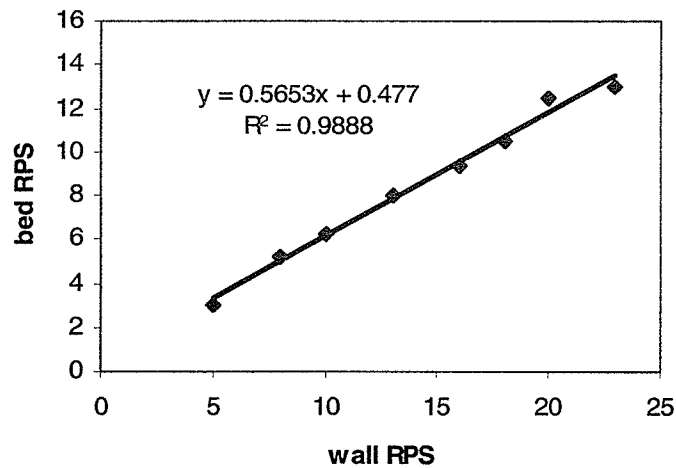


**Figure A4** Velocity calibration curve when bed roughness is 1 cm and water depth is 12 cm.

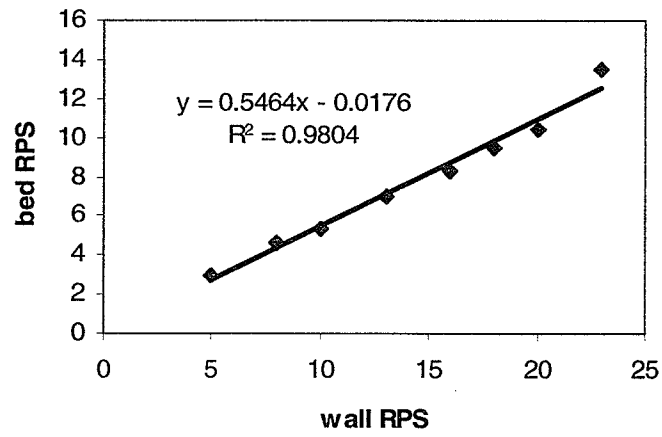


**Figure A5** Velocity calibration curve when bed roughness is 2 cm and water depth is 12 cm.

---

Appendix B

## *Water Temperature Measurements*

---

The data presented in this appendix shows the water temperature curves for the experiments carried out. The experiments were divided into three groups with three water depths 8, 10, 12 cm. Unfortunately, when the water depth was 8 cm, the thermometer probe was too close to the surface and sometimes it was exposed to the air, therefore, some of the temperature curves do not show the real water temperature. Only water temperature curves for water depths of 10 and 12 cm are shown in this appendix.

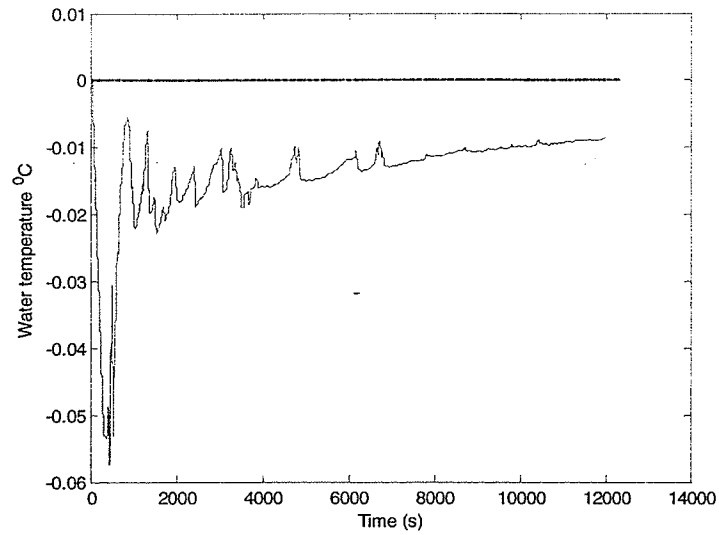


**Figure B1** Water temperature curve from Exp. 3-2 when the bed velocity is 0.57 m/s, water depth is 0.1 m and air temperature is  $-20^{\circ}\text{C}$ .

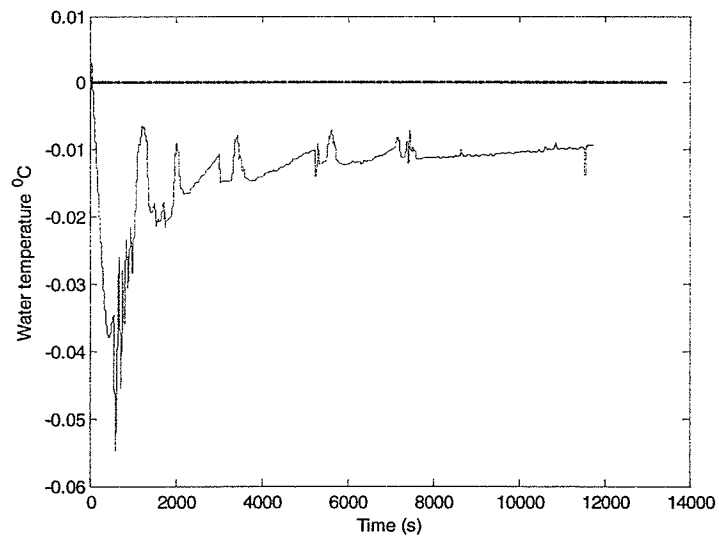


**Figure B2** Water temperature curve from Exp. 3-3 when the bed velocity is 0.57 m/s, water depth is 0.1 m and air temperature is  $-16^{\circ}\text{C}$ .

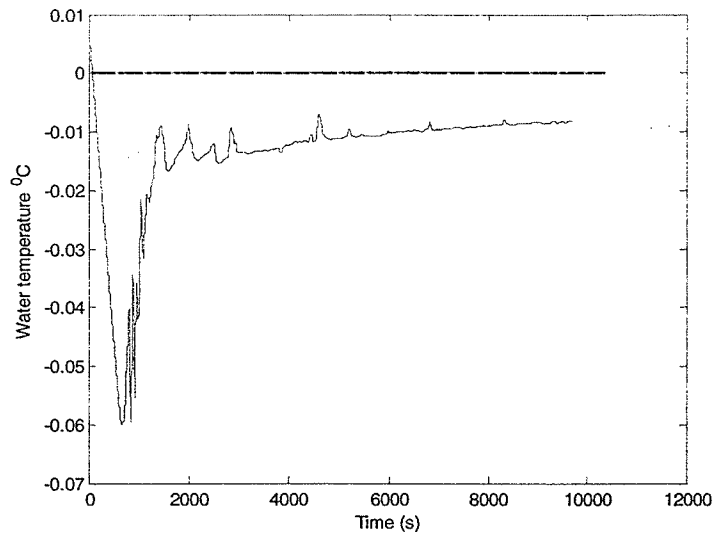


**Figure B3** Water temperature curve from Exp. 3-4 when the bed velocity is 0.75 m/s, water depth is 0.1 m and air temperature is  $-16^{\circ}\text{C}$ .

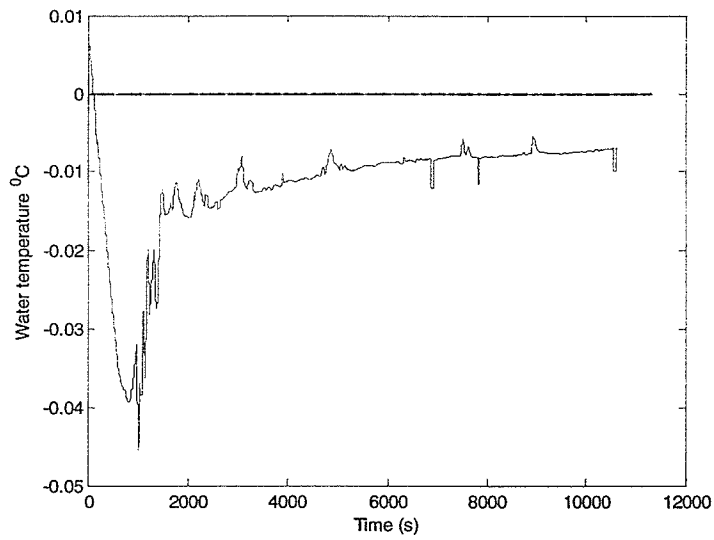


**Figure B4** Water temperature curve from Exp. 3-5 when the bed velocity is 0.57 m/s, water depth is 0.1 m and air temperature is  $-12^{\circ}\text{C}$ .

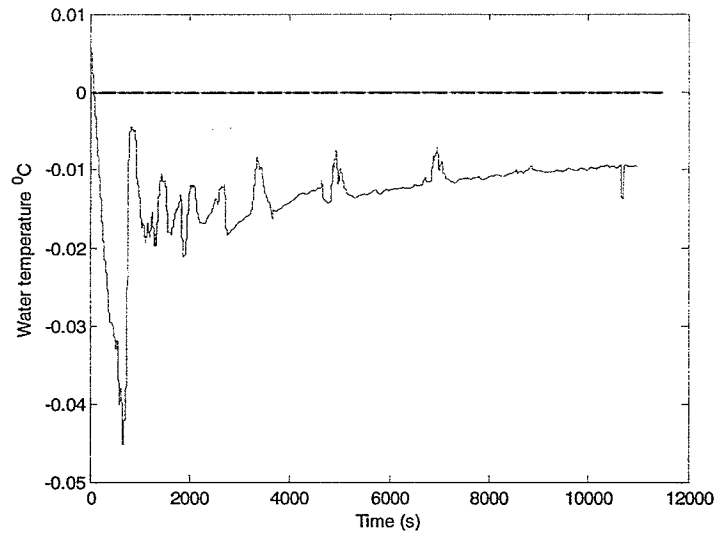


**Figure B5** Water temperature curve from Exp. 3-9 when the bed velocity is 0.38 m/s, water depth is 0.12 m and air temperature is  $-16^{\circ}\text{C}$ .

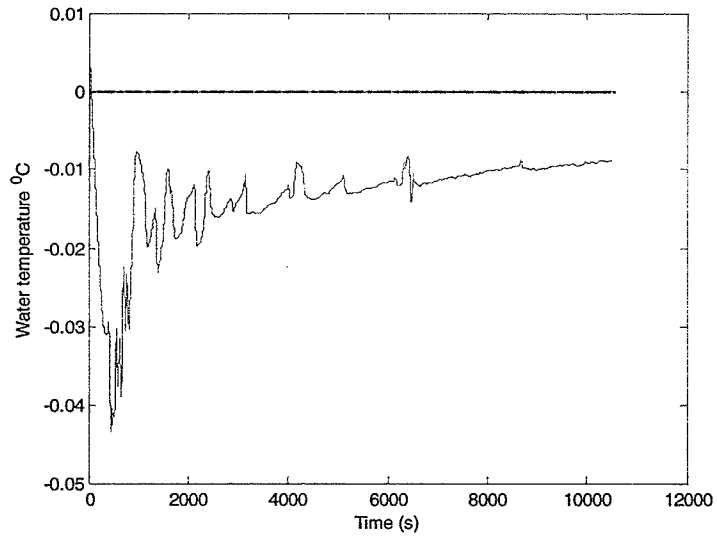


**Figure B6** Water temperature curve from Exp. 3-10 when the bed velocity is 0.57 m/s, water depth is 0.12 m and air temperature is  $-20^{\circ}\text{C}$ .

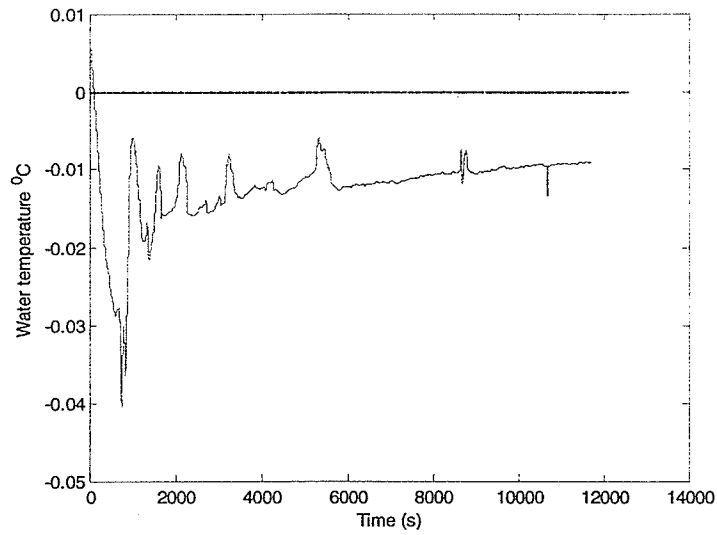


**Figure B7** Water temperature curve from Exp. 3-12 when the bed velocity is 0.57 m/s, water depth is 0.12 m and air temperature is  $-16^{\circ}\text{C}$ .

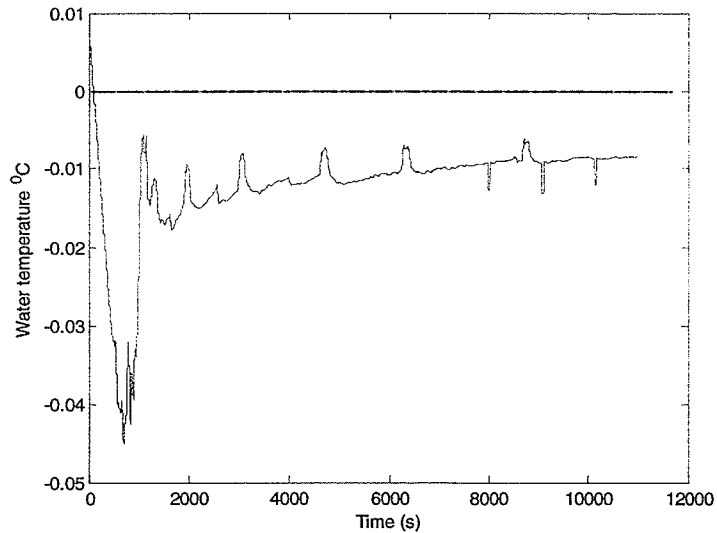


**Figure B8** Water temperature curve from Exp. 3-15 when the bed velocity is 0.57 m/s, water depth is 0.12 m and air temperature is  $-12^{\circ}\text{C}$ .

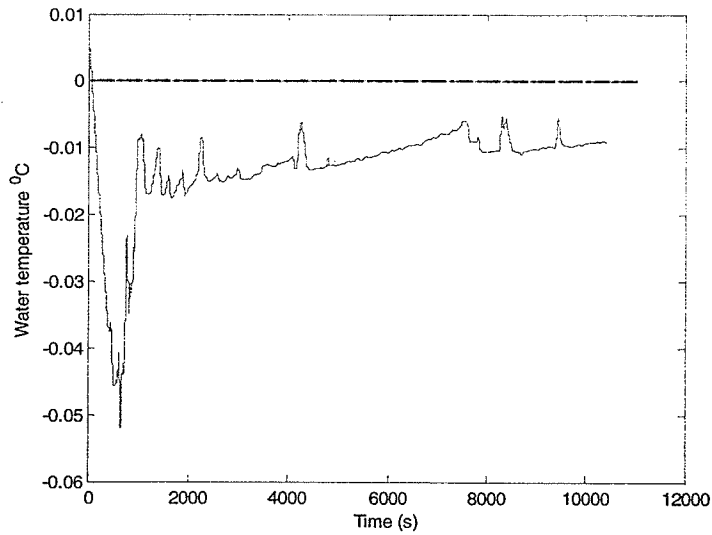


**Figure B9** Water temperature curve from Exp. 3-16 when the bed velocity is 0.75 m/s, water depth is 0.12 m and air temperature is  $-16^{\circ}\text{C}$ .

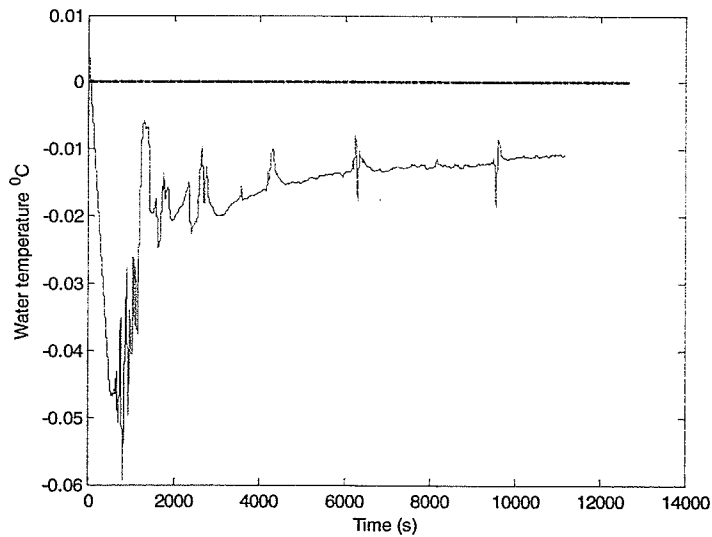


**Figure B10** Water temperature curve from Exp. 3-17 when the bed velocity is 0.38 m/s, water depth is 0.08 m and air temperature is  $-12^{\circ}\text{C}$ .

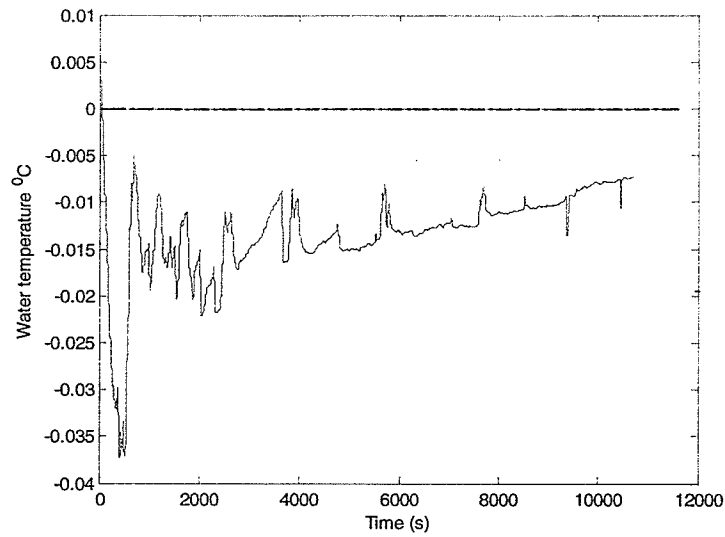


**Figure B11** Water temperature curve from Exp. 4-5 when the bed velocity is 0.38 m/s, water depth is 0.1 m and air temperature is  $-20^{\circ}\text{C}$ .

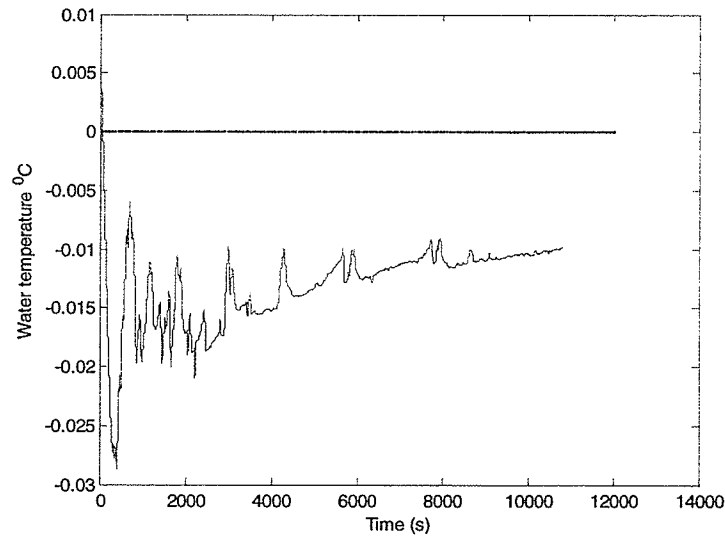


**Figure B12** Water temperature curve from Exp. 4-6 when the bed velocity is 0.38 m/s, water depth is 0.1 m and air temperature is  $-16^{\circ}\text{C}$ .

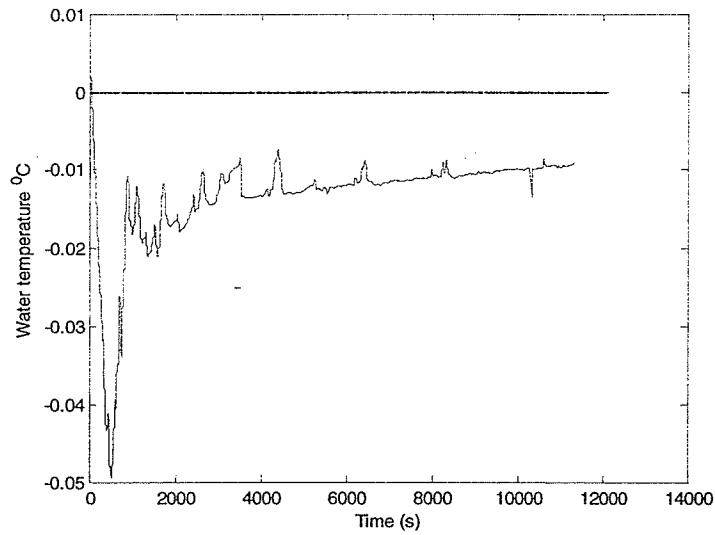


**Figure B13** Water temperature curve from Exp. 4-7 when the bed velocity is 0.57 m/s, water depth is 0.1 m and air temperature is  $-16^{\circ}\text{C}$ .

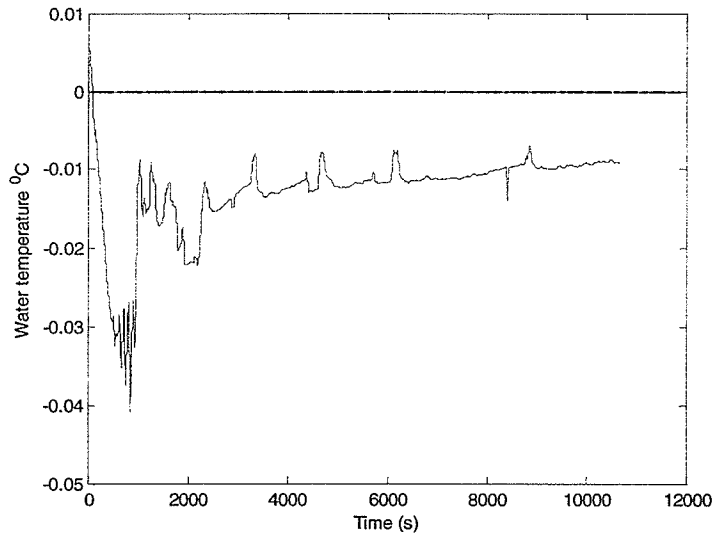


**Figure B14** Water temperature curve from Exp. 4-9 when the bed velocity is 0.38 m/s, water depth is 0.1 m and air temperature is  $-12^{\circ}\text{C}$ .

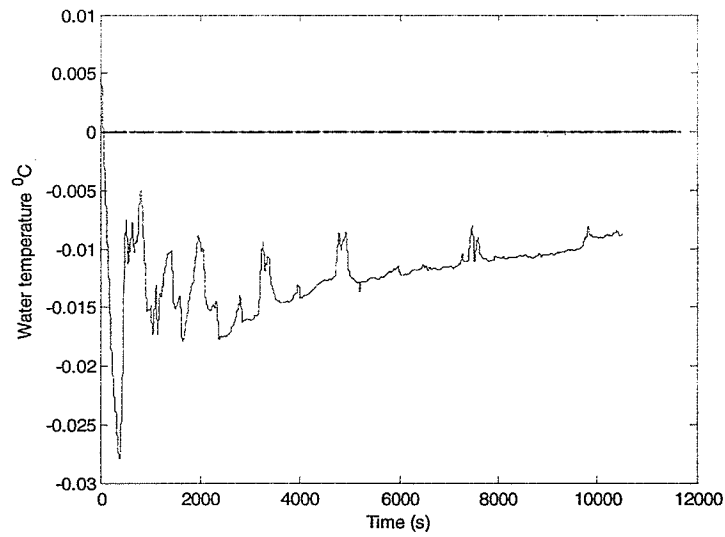


**Figure B15** Water temperature curve from Exp. 4-12 when the bed velocity is 0.38 m/s, water depth is 0.12 m and air temperature is  $-16^{\circ}\text{C}$ .

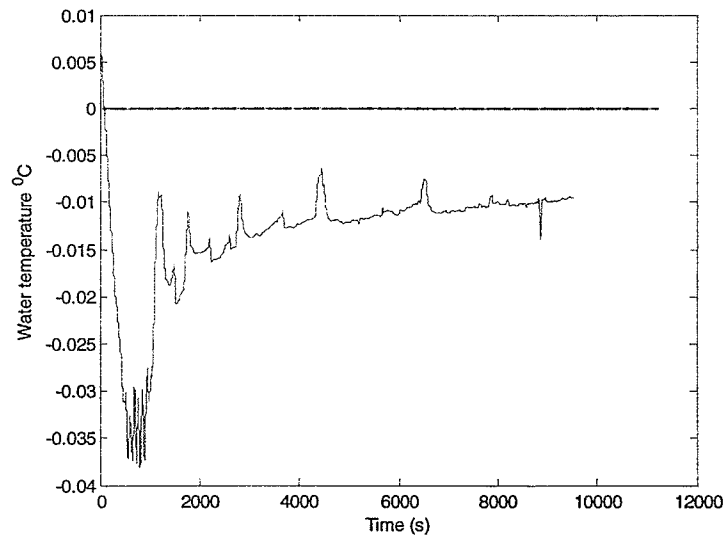


**Figure B16** Water temperature curve from Exp. 4-14 when the bed velocity is 0.57 m/s, water depth is 0.12 m and air temperature is  $-16^{\circ}\text{C}$ .

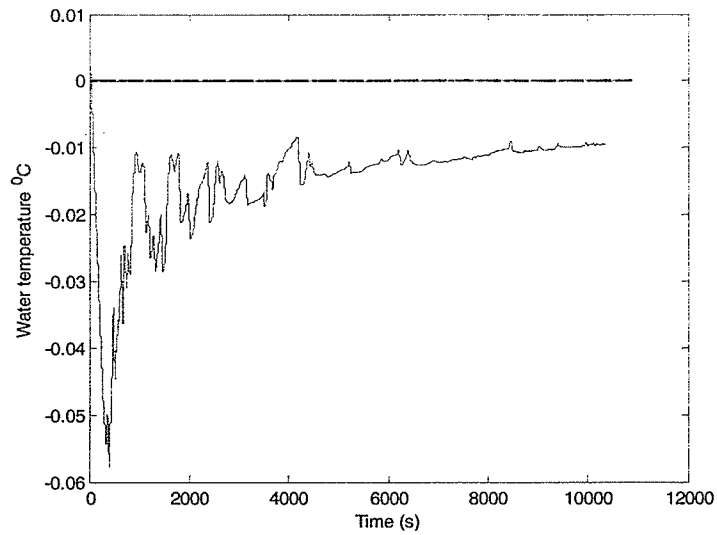


**Figure B17** Water temperature curve from Exp. 4-25 when the bed velocity is 0.38 m/s, water depth is 0.1 m and air temperature is  $-20^{\circ}\text{C}$ .

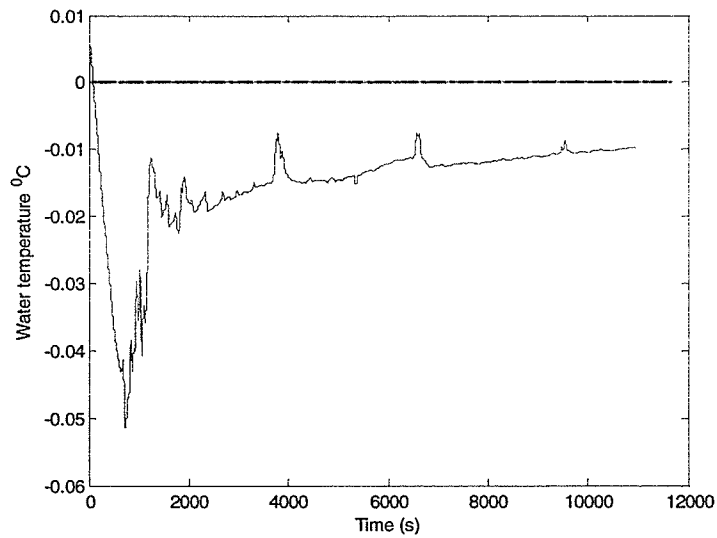


**Figure B18** Water temperature curve from Exp. 4-27 when the bed velocity is 0.38 m/s, water depth is 0.1 m and air temperature is  $-12^{\circ}\text{C}$ .

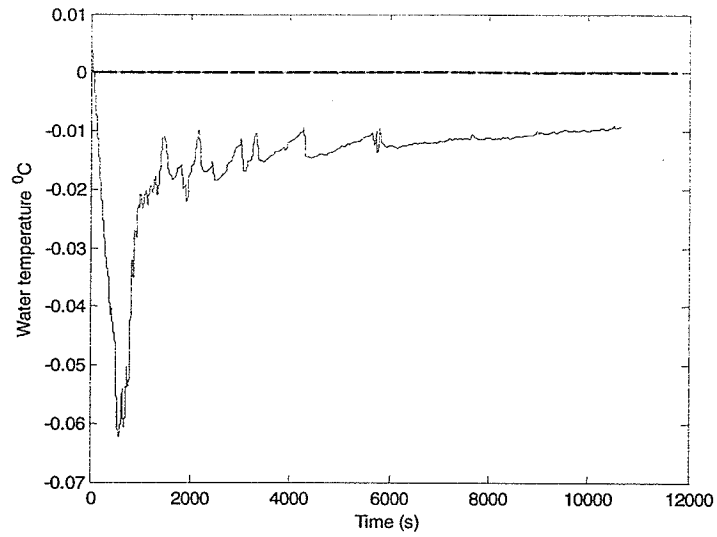


**Figure B19** Water temperature curve from Exp. 4-29 when the bed velocity is 0.57 m/s, water depth is 0.1 m and air temperature is -16°C.

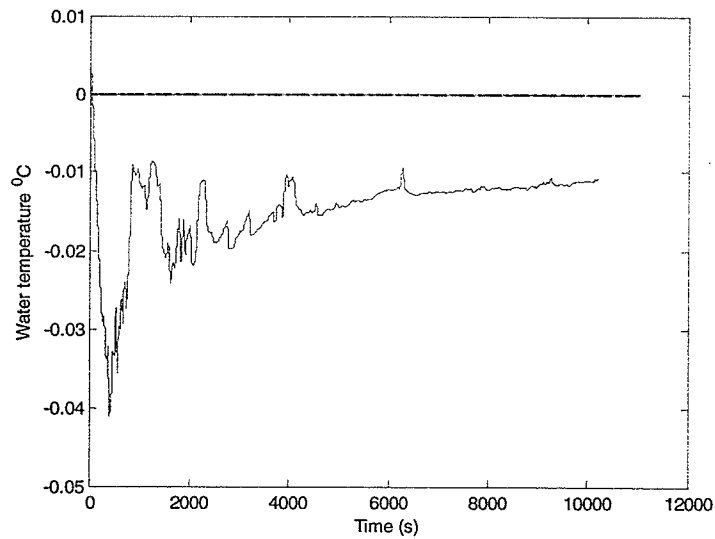


**Figure B20** Water temperature curve from Exp. 4-30 when the bed velocity is 0.38 m/s, water depth is 0.12 m and air temperature is -20°C.

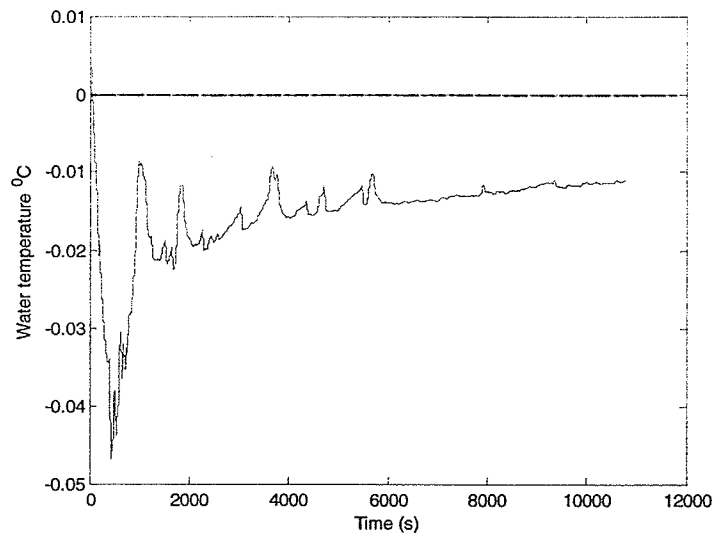


**Figure B21** Water temperature curve from Exp. 5-2 when the bed velocity is 0.38 m/s, water depth is 0.12 m and air temperature is  $-16^{\circ}\text{C}$ .

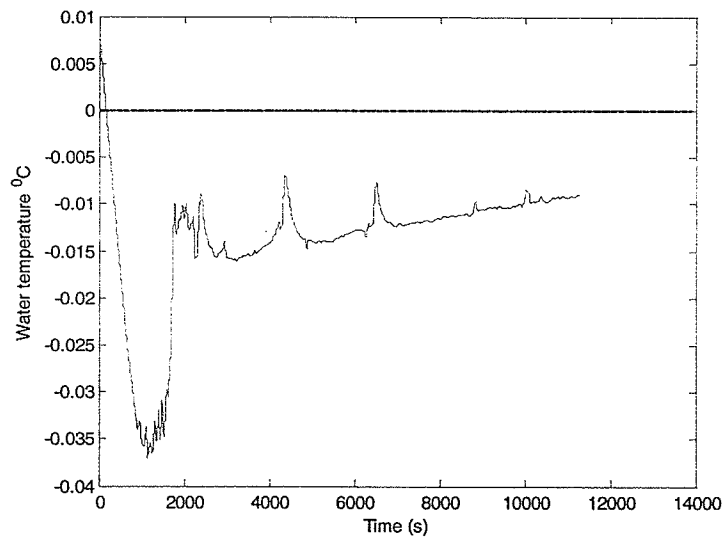


**Figure B22** Water temperature curve from Exp. 5-4 when the bed velocity is 0.38 m/s, water depth is 0.12 m and air temperature is  $-12^{\circ}\text{C}$ .

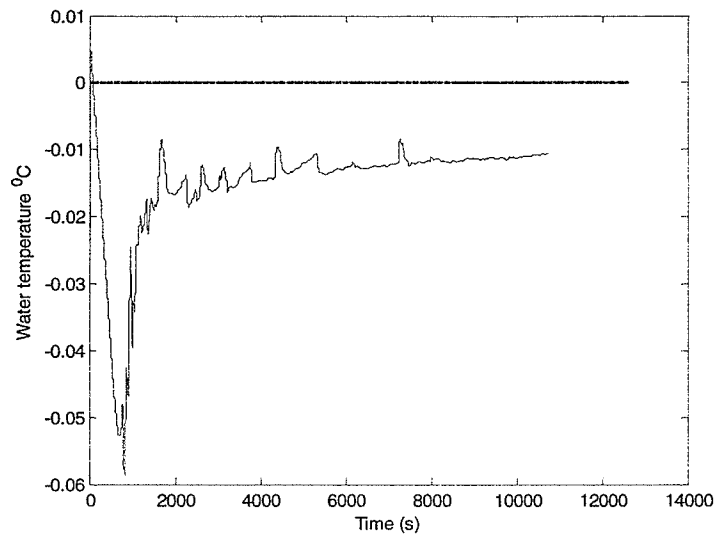


**Figure B23** Water temperature curve from Exp. 5-5 when the bed velocity is 0.57 m/s, water depth is 0.12 m and air temperature is -16°C.

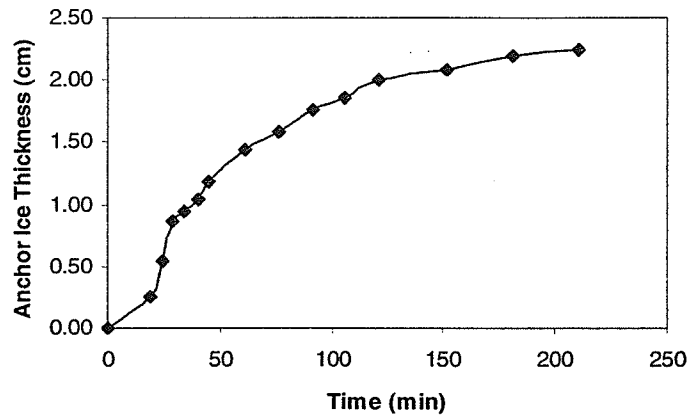
---

Appendix C

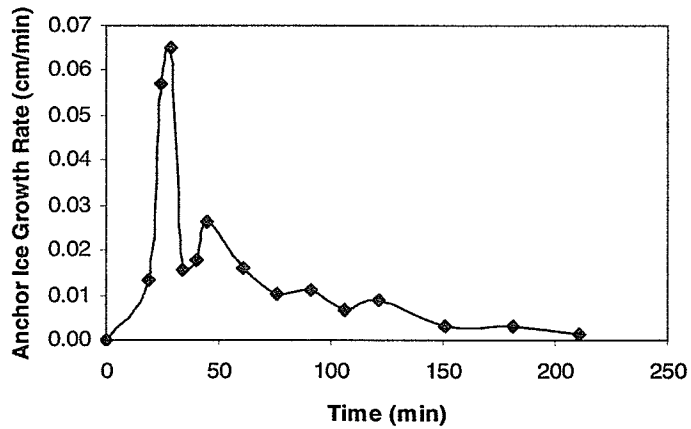
## *Anchor Ice Thickness and Growth Rate Measurements*

---

The data presented in this appendix shows the anchor ice thickness and growth rate measurements for experiments under different air temperature and flow conditions. It was observed that anchor ice grew the quickest during the peak production of frazil ice particles, which occurred usually during the first hour of the tests as shown in the anchor ice growth rate figures. Therefore, the thickness and growth rate of anchor ice were analyzed every 5 minutes in the first hour of each test and after that, they were analyzed every 15 or 30 minutes by the image processing program.

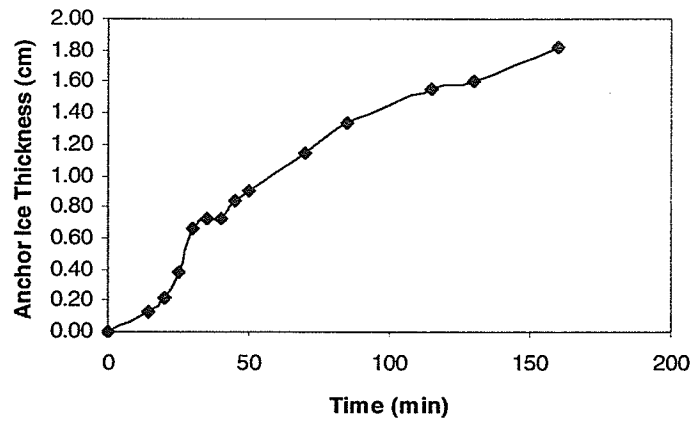


(a)

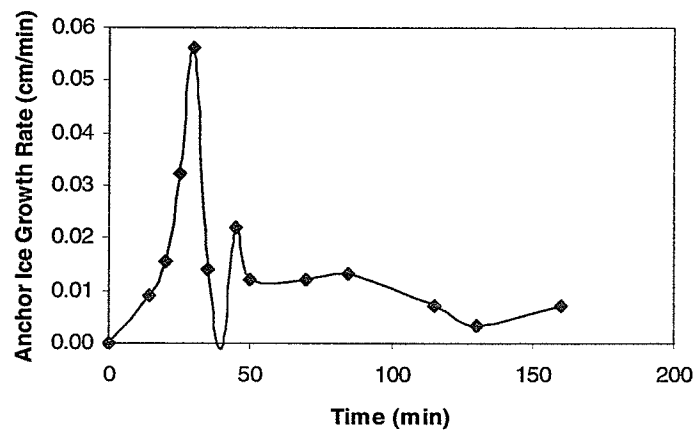


(b)

**Figure C1** (a) Anchor ice thickness (b) Anchor ice growth rate from Exp. 2-23 when the bed velocity is 0.38 m/s, water depth is 0.1 m and air temperature is  $-16^{\circ}\text{C}$ .

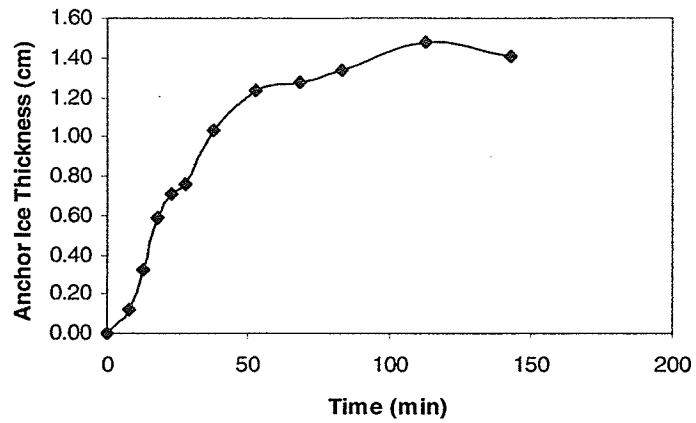


(a)

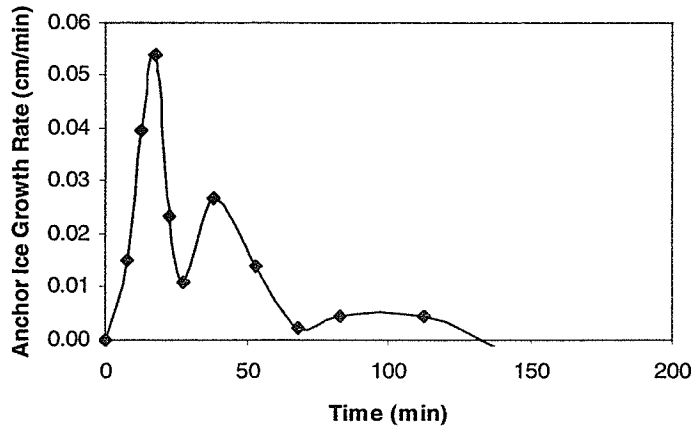


(b)

**Figure C2** (a) Anchor ice thickness (b) Anchor ice growth rate from Exp. 2-24 when the bed velocity is 0.38 m/s, water depth is 0.1 m and air temperature is  $-12^{\circ}\text{C}$ .

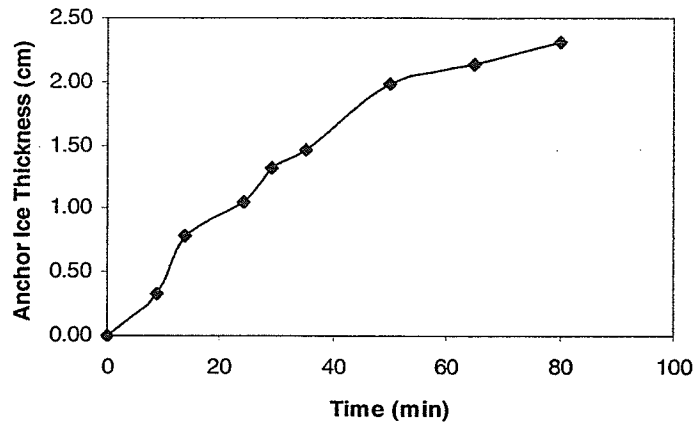


(a)

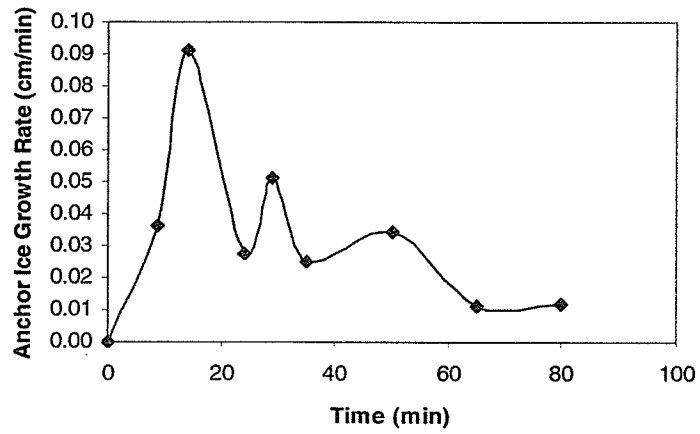


(b)

**Figure C3** (a) Anchor ice thickness (b) Anchor ice growth rate from Exp. 3-4 when the bed velocity is 0.75 m/s, water depth is 0.1 m and air temperature is  $-16^{\circ}\text{C}$ .

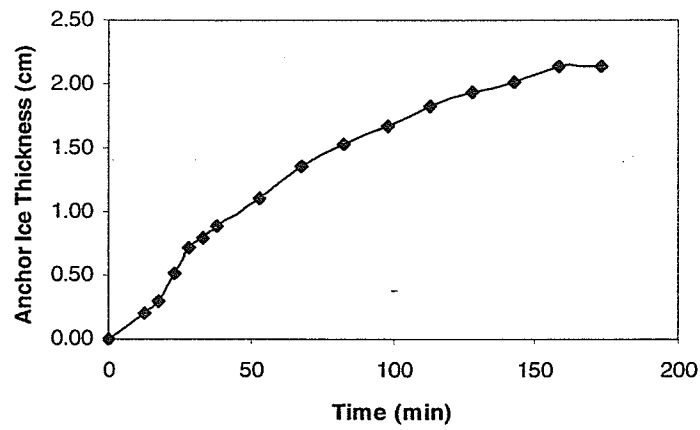


(a)

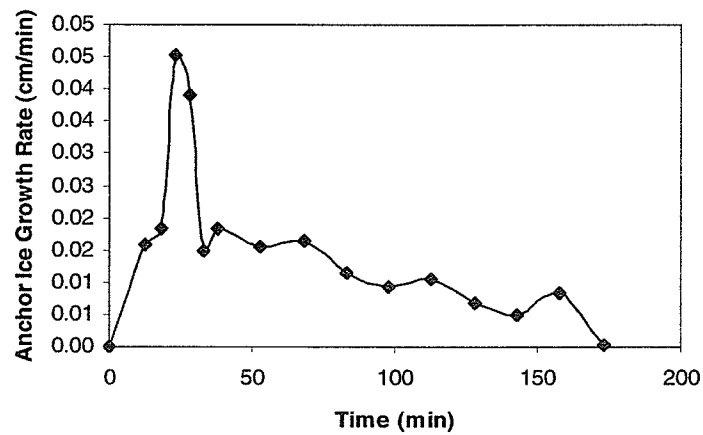


(b)

**Figure C4** (a) Anchor ice thickness (b) Anchor ice growth rate from Exp. 3-8 when the bed velocity is 0.38 m/s, water depth is 0.12 m and air temperature is  $-20^{\circ}\text{C}$ .

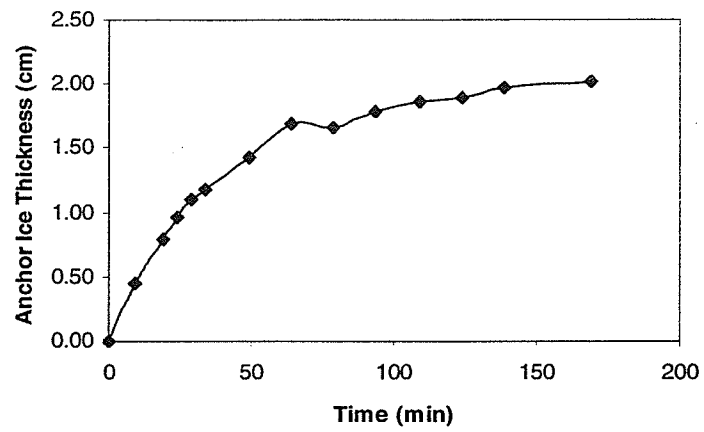


(a)

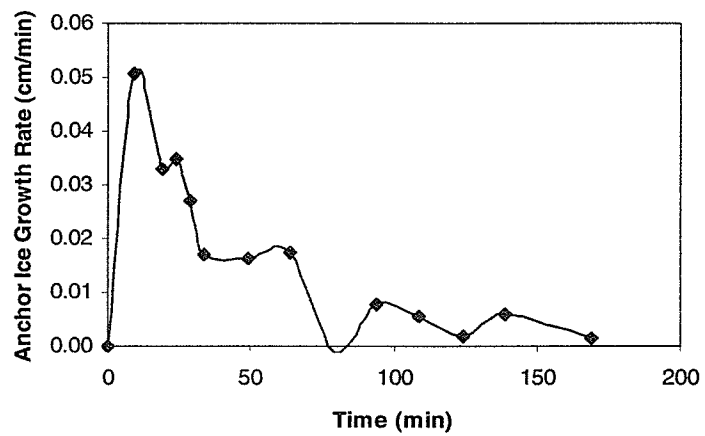


(b)

**Figure C5** (a) Anchor ice thickness (b) Anchor ice growth rate from Exp. 3-9 when the bed velocity is 0.38 m/s, water depth is 0.12 m and air temperature is  $-16^{\circ}\text{C}$ .

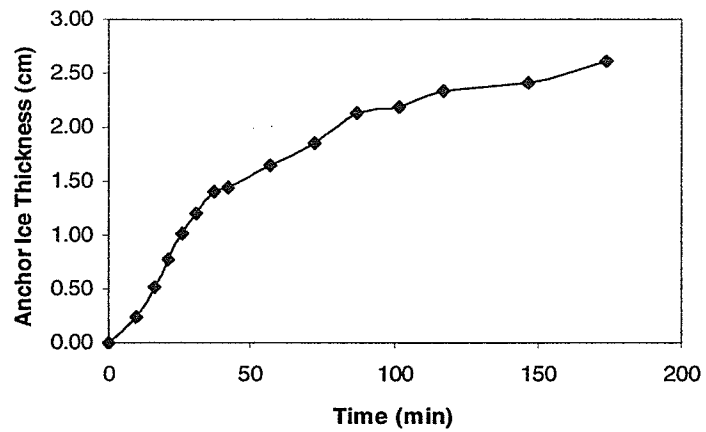


(a)

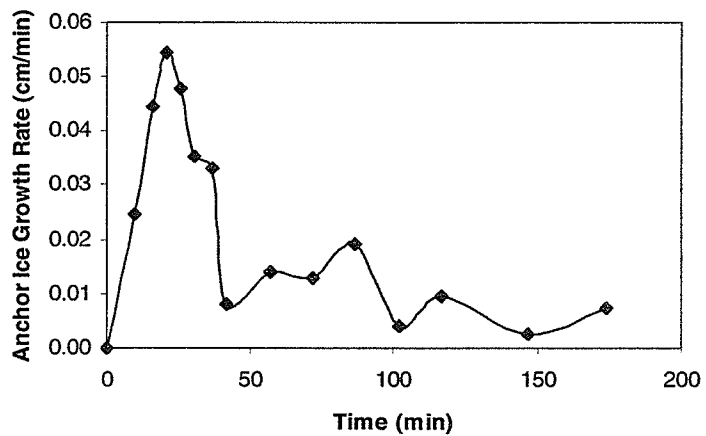


(b)

**Figure C6** (a) Anchor ice thickness (b) Anchor ice growth rate from Exp. 3-10 when the bed velocity is 0.57 m/s, water depth is 0.12 m and air temperature is  $-20^{\circ}\text{C}$ .

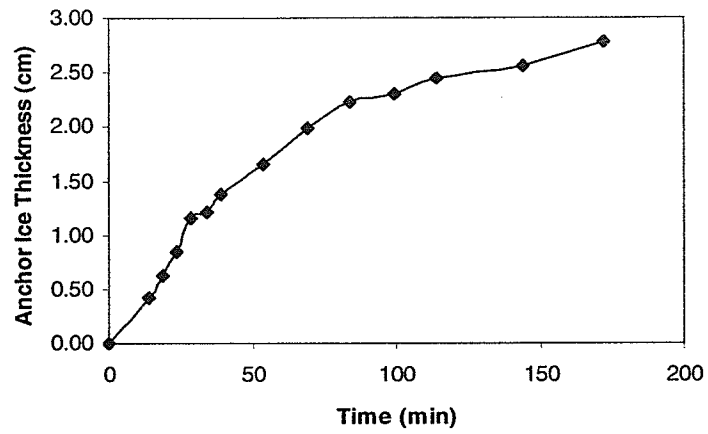


(a)

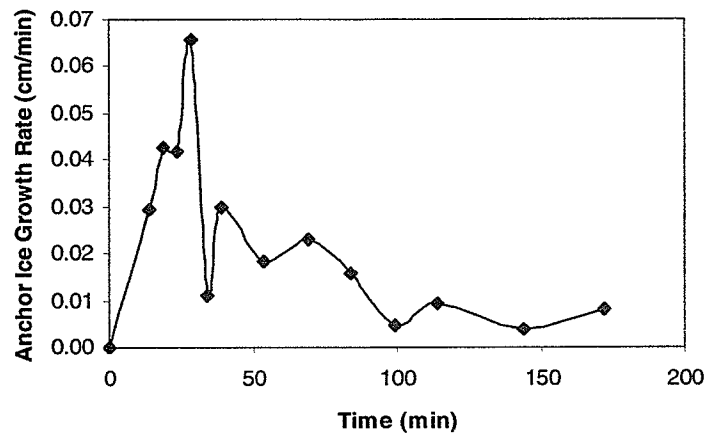


(b)

**Figure C7** (a) Anchor ice thickness (b) Anchor ice growth rate from Exp. 3-18 when the bed velocity is 0.38 m/s, water depth is 0.08 m and air temperature is  $-16^{\circ}\text{C}$ .

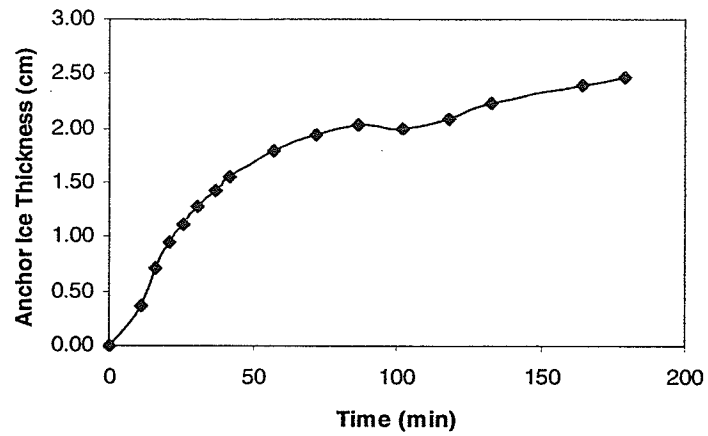


(a)

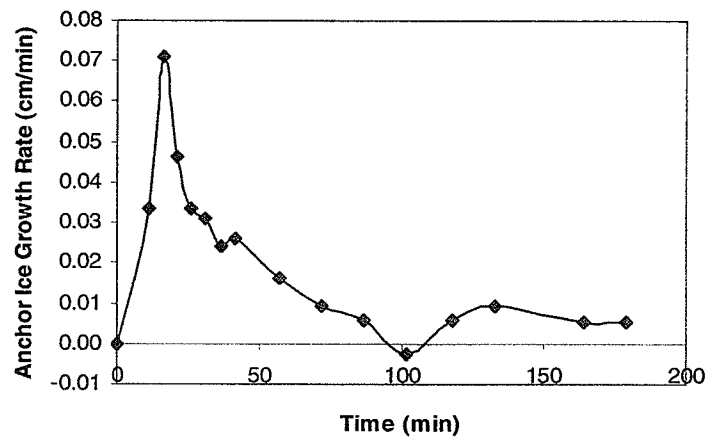


(b)

**Figure C8** (a) Anchor ice thickness (b) Anchor ice growth rate from Exp. 3-19 when the bed velocity is 0.38 m/s, water depth is 0.08 m and air temperature is  $-20^{\circ}\text{C}$ .

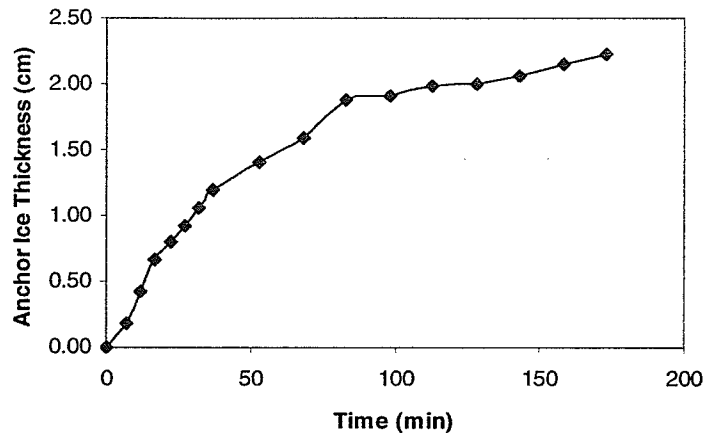


(a)

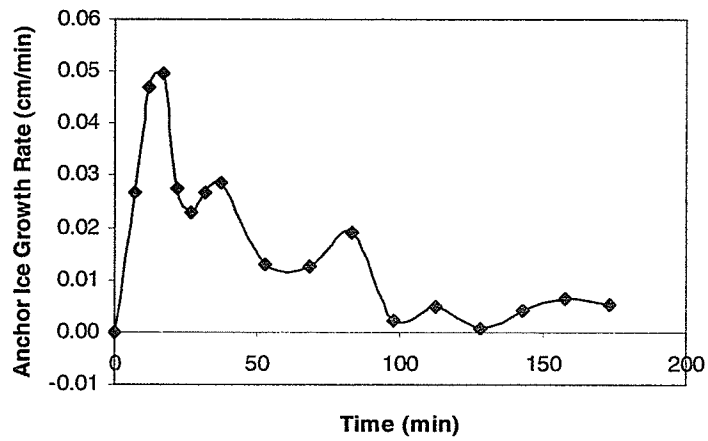


(b)

**Figure C9** (a) Anchor ice thickness (b) Anchor ice growth rate from Exp. 3-21 when the bed velocity is 0.57 m/s, water depth is 0.08 m and air temperature is  $-20^{\circ}\text{C}$ .

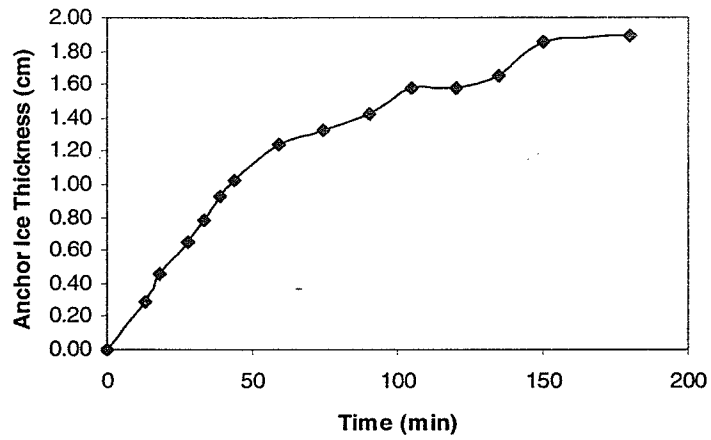


(a)

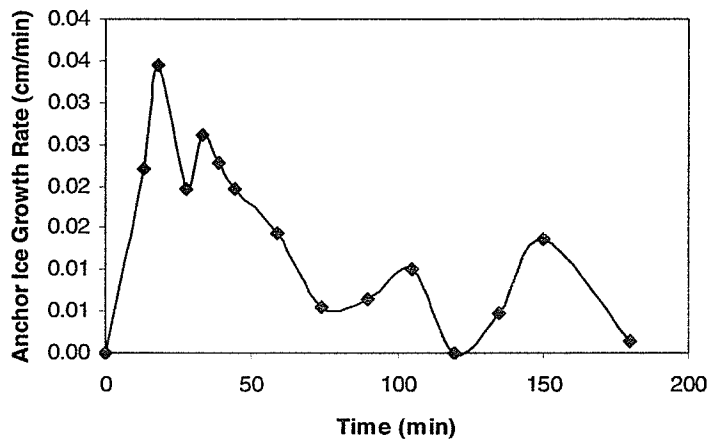


(b)

**Figure C10** (a) Anchor ice thickness (b) Anchor ice growth rate from Exp. 3-22 when the bed velocity is 0.57 m/s, water depth is 0.08 m and air temperature is  $-16^{\circ}\text{C}$ .

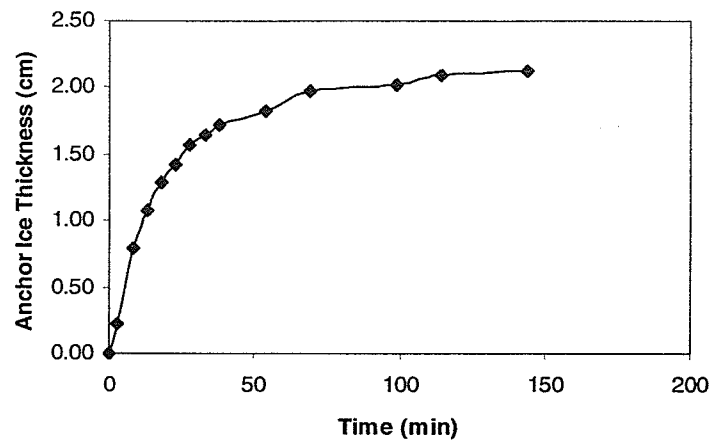


(a)

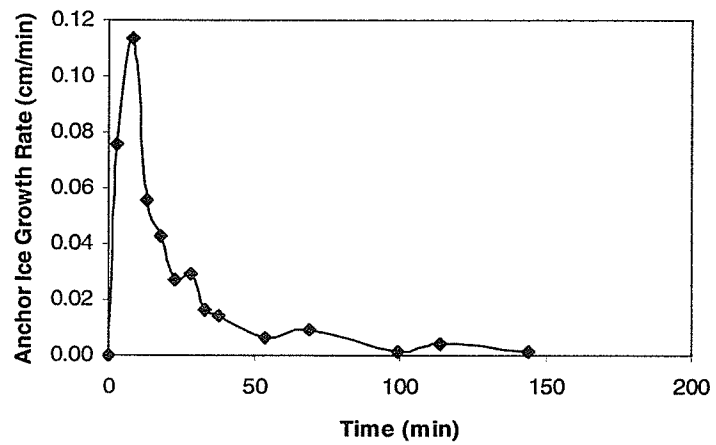


(b)

**Figure C11** (a) Anchor ice thickness (b) Anchor ice growth rate from Exp. 3-23 when the bed velocity is 0.57 m/s, water depth is 0.08 m and air temperature is  $-12^{\circ}\text{C}$ .

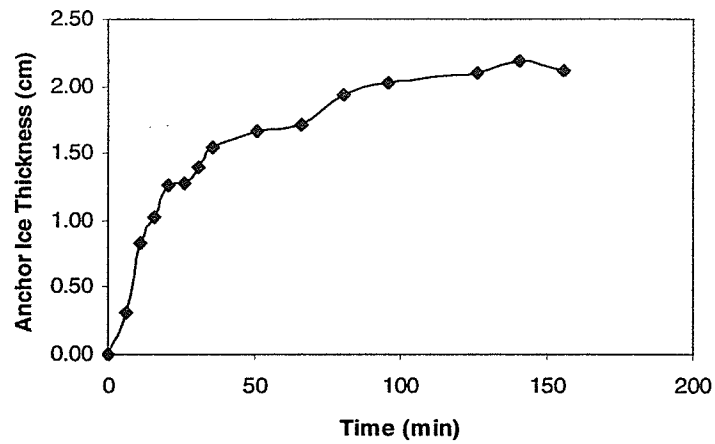


(a)

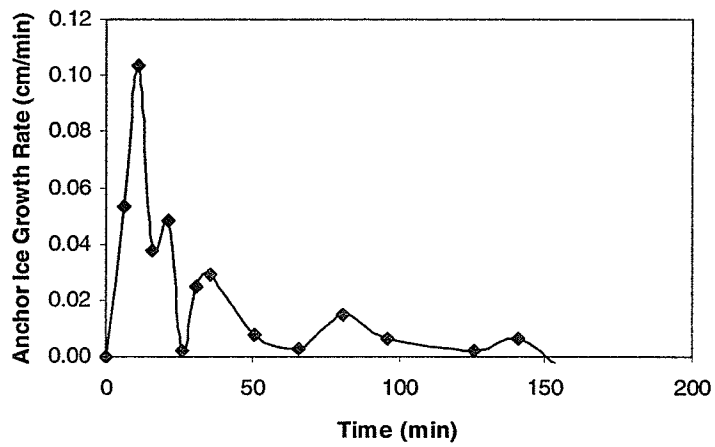


(b)

**Figure C12** (a) Anchor ice thickness (b) Anchor ice growth rate from Exp. 3-30 when the bed velocity is 0.38 m/s, water depth is 0.08 m and air temperature is  $-20^{\circ}\text{C}$ .

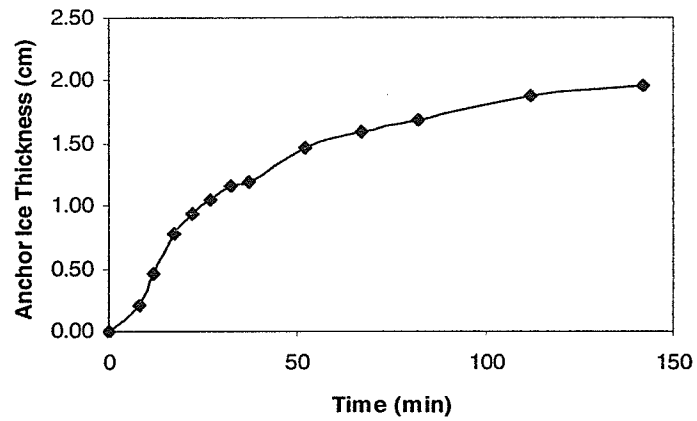


(a)

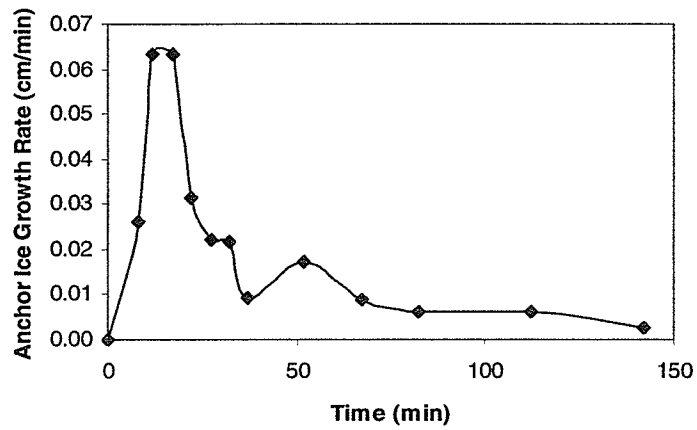


(b)

**Figure C13** (a) Anchor ice thickness (b) Anchor ice growth rate from Exp. 3-31 when the bed velocity is 0.38 m/s, water depth is 0.08 m and air temperature is  $-16^{\circ}\text{C}$ .

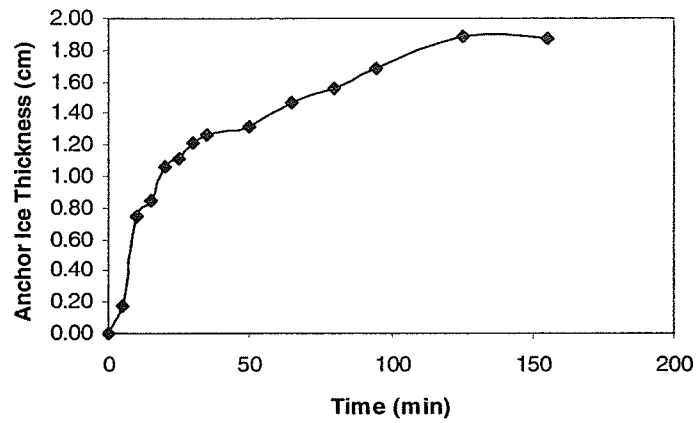


(a)

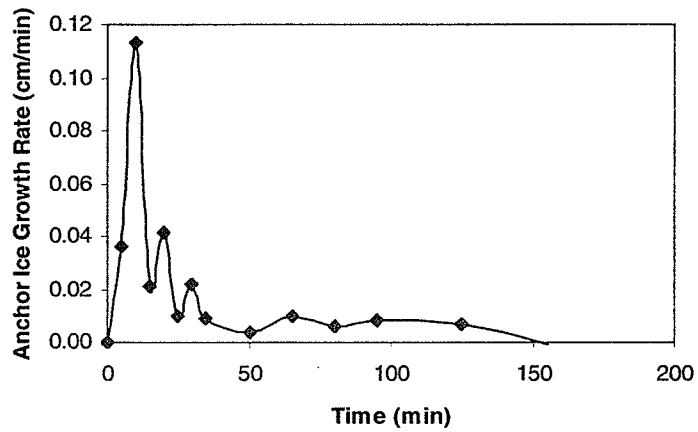


(b)

**Figure C14** (a) Anchor ice thickness (b) Anchor ice growth rate from Exp. 4-1 when the bed velocity is 0.38 m/s, water depth is 0.08 m and air temperature is  $-12^{\circ}\text{C}$ .

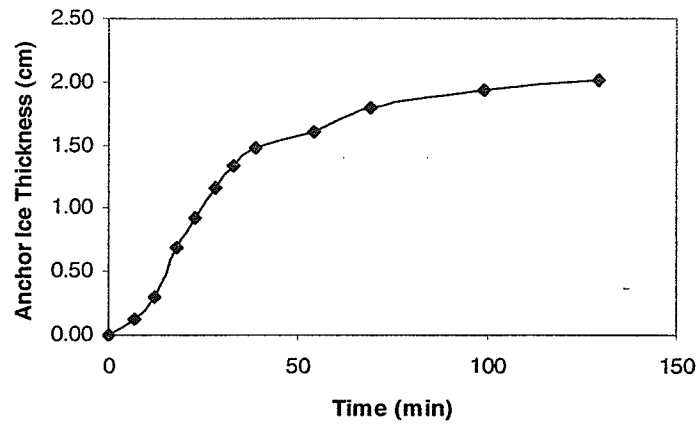


(a)

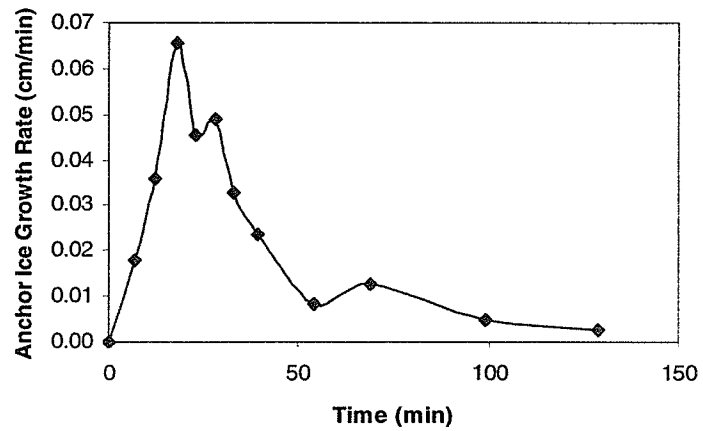


(b)

**Figure C15** (a) Anchor ice thickness (b) Anchor ice growth rate from Exp. 4-2 when the bed velocity is 0.57 m/s, water depth is 0.08 m and air temperature is  $-16^{\circ}\text{C}$ .

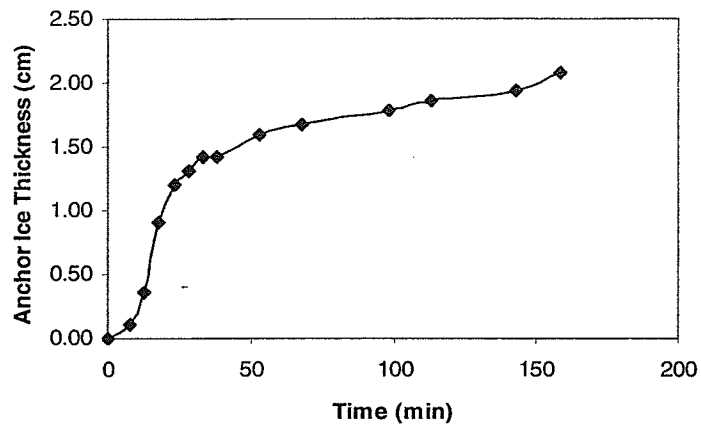


(a)

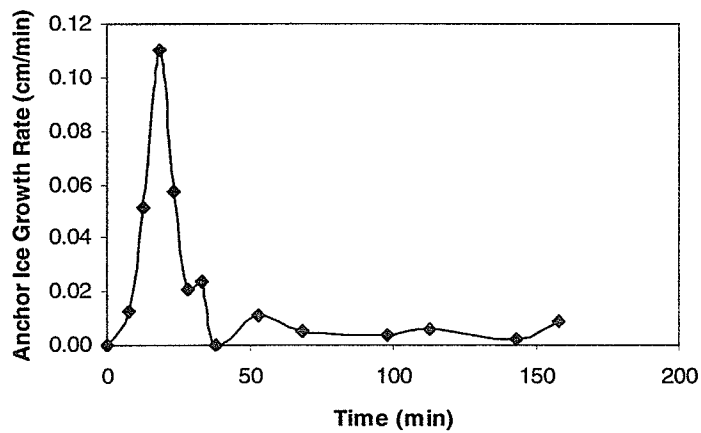


(b)

**Figure C16** (a) Anchor ice thickness (b) Anchor ice growth rate from Exp. 4-5 when the bed velocity is 0.38 m/s, water depth is 0.1 m and air temperature is  $-20^{\circ}\text{C}$ .

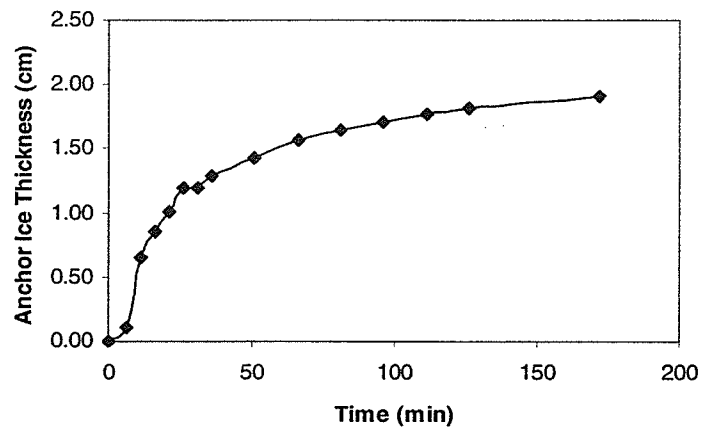


(a)

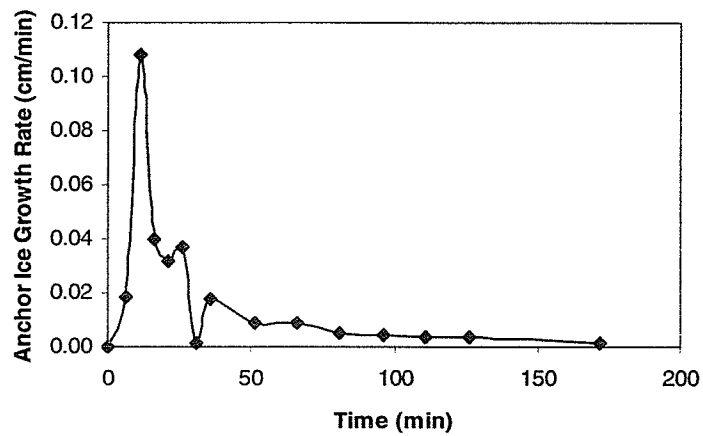


(b)

**Figure C17** (a) Anchor ice thickness (b) Anchor ice growth rate from Exp. 4-6 when the bed velocity is 0.38 m/s, water depth is 0.1 m and air temperature is  $-16^{\circ}\text{C}$ .

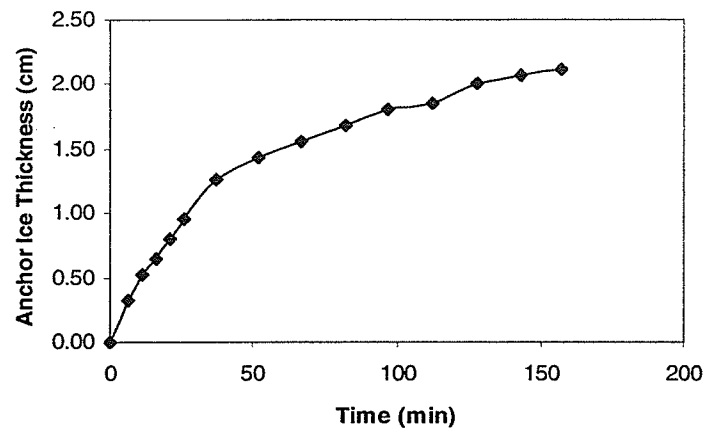


(a)

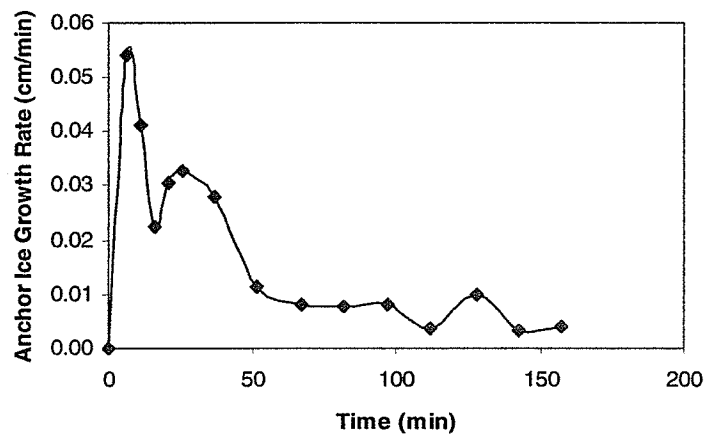


(b)

**Figure C18** (a) Anchor ice thickness (b) Anchor ice growth rate from Exp. 4-7 when the bed velocity is 0.57 m/s, water depth is 0.1 m and air temperature is  $-16^{\circ}\text{C}$ .

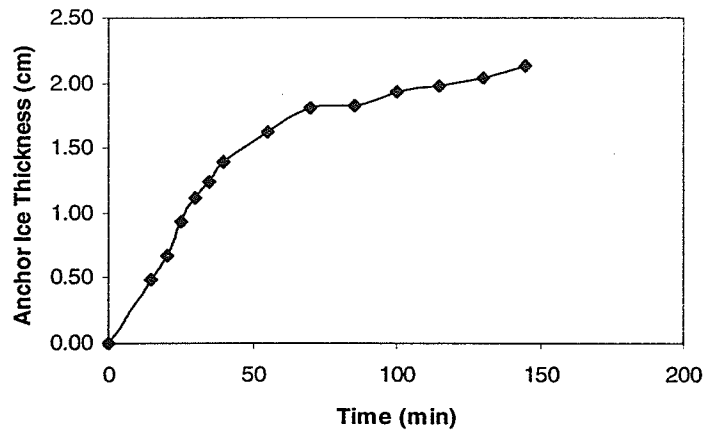


(a)

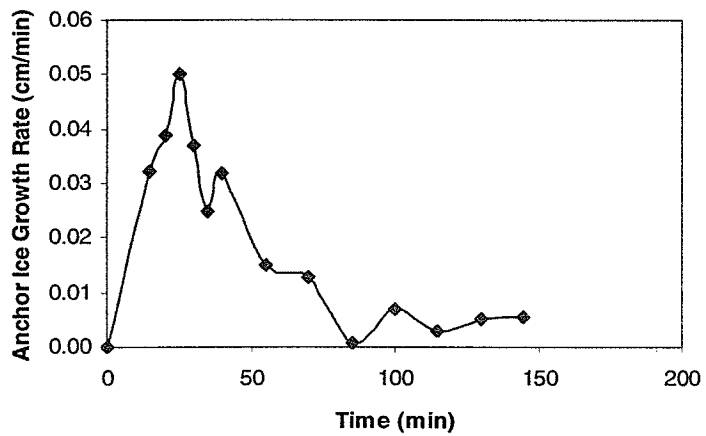


(b)

**Figure C19** (a) Anchor ice thickness (b) Anchor ice growth rate from Exp. 4-9 when the bed velocity is 0.38 m/s, water depth is 0.1 m and air temperature is  $-12^{\circ}\text{C}$ .

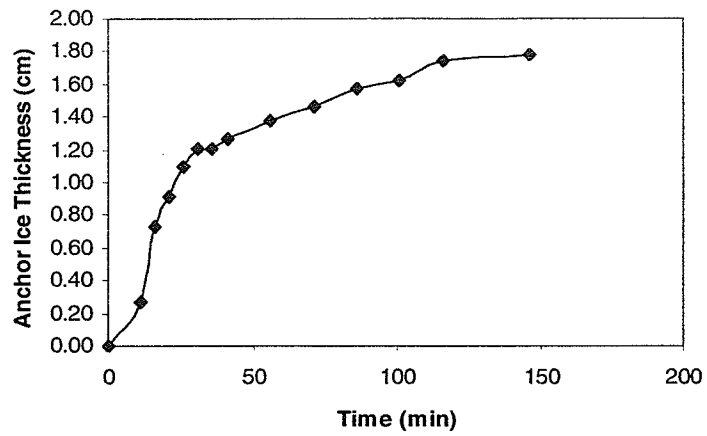


(a)

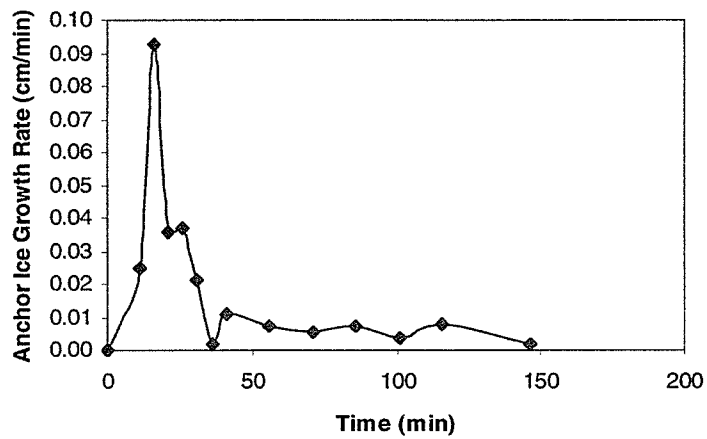


(b)

**Figure C20** (a) Anchor ice thickness (b) Anchor ice growth rate from Exp. 4-12 when the bed velocity is 0.38 m/s, water depth is 0.12 m and air temperature is  $-16^{\circ}\text{C}$ .

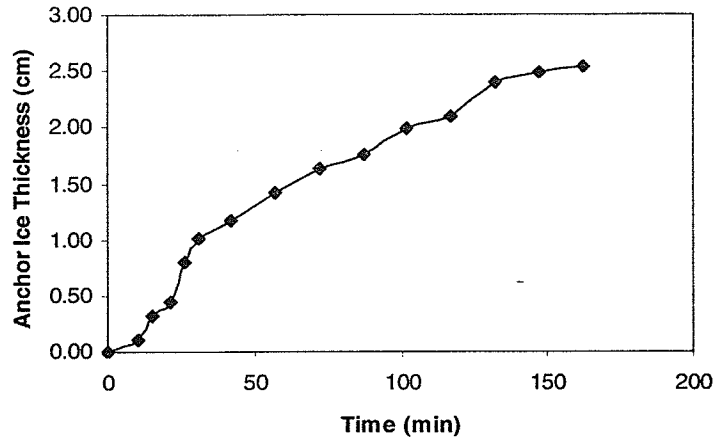


(a)

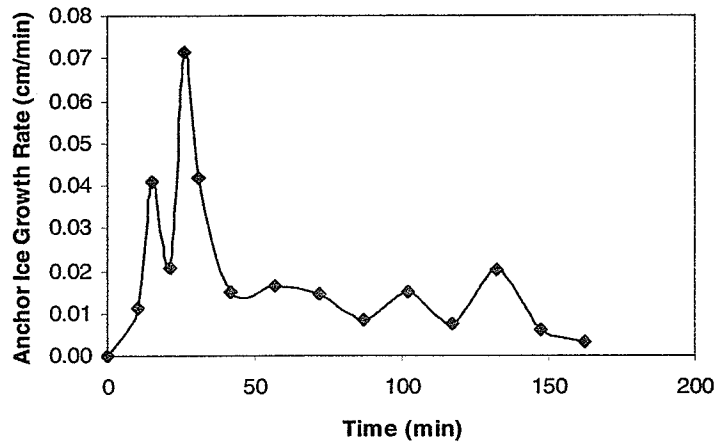


(b)

**Figure C21** (a) Anchor ice thickness (b) Anchor ice growth rate from Exp. 4-14 when the bed velocity is 0.57 m/s, water depth is 0.12 m and air temperature is  $-16^{\circ}\text{C}$ .

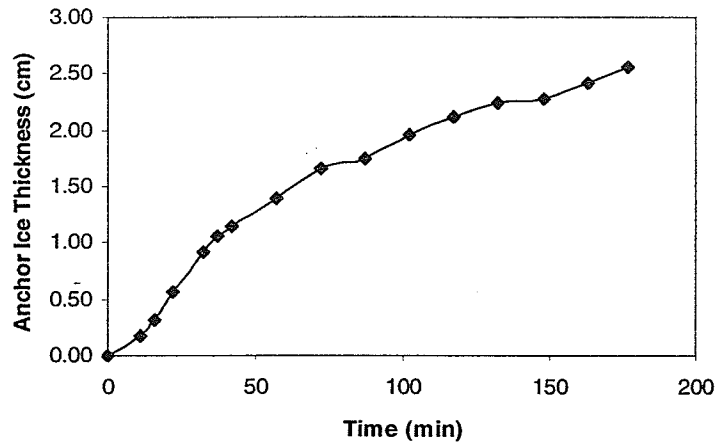


(a)

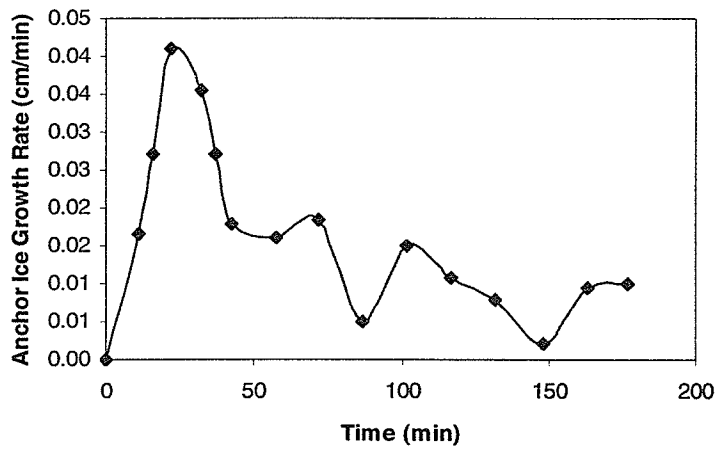


(b)

**Figure C22** (a) Anchor ice thickness (b) Anchor ice growth rate from Exp. 4-19 when the bed velocity is 0.38 m/s, water depth is 0.08 m and air temperature is  $-20^{\circ}\text{C}$ .

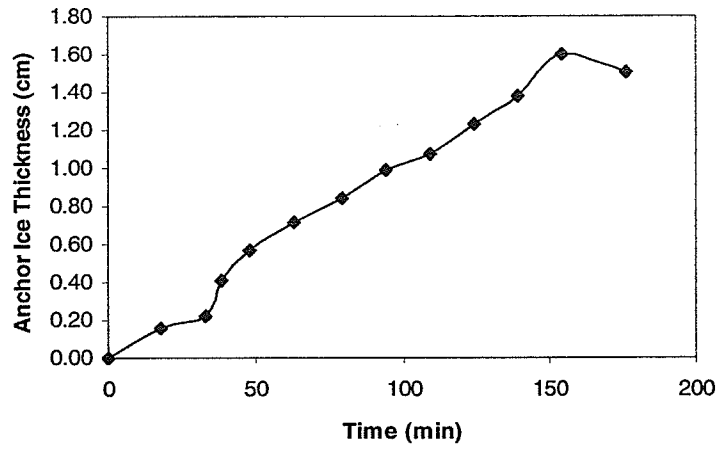


(a)

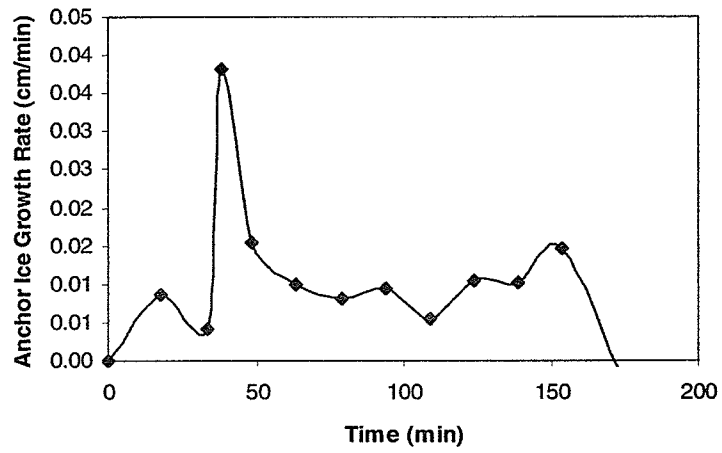


(b)

**Figure C23** (a) Anchor ice thickness (b) Anchor ice growth rate from Exp. 4-20 when the bed velocity is 0.38 m/s, water depth is 0.08 m and air temperature is  $-16^{\circ}\text{C}$ .

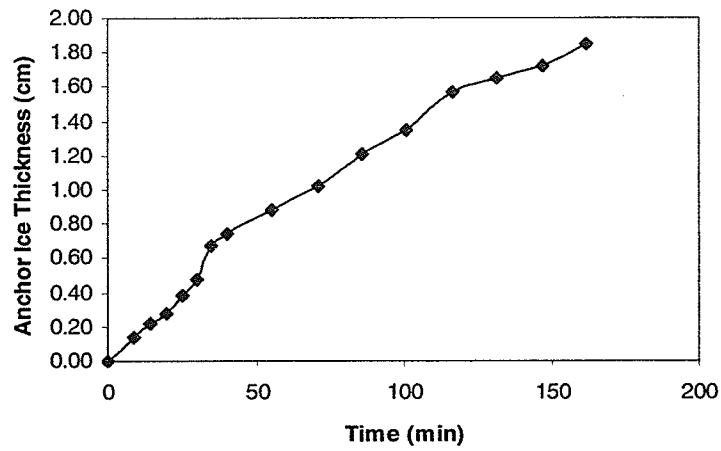


(a)

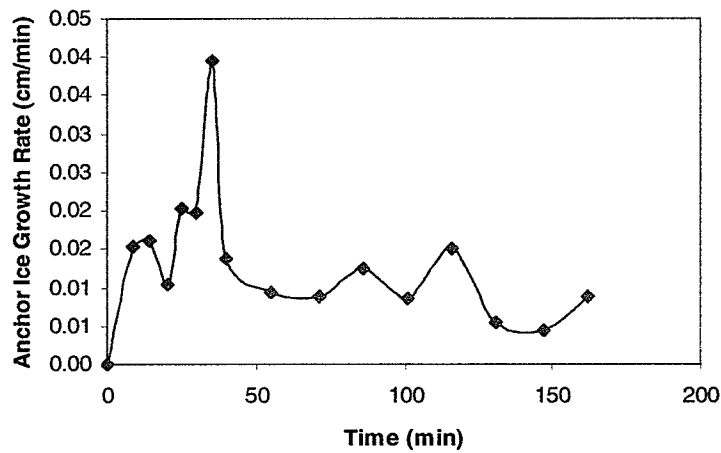


(b)

**Figure C24** (a) Anchor ice thickness (b) Anchor ice growth rate from Exp. 5-4 when the bed velocity is 0.38 m/s, water depth is 0.12 m and air temperature is  $-12^{\circ}\text{C}$ .



(a)



(b)

**Figure C25** (a) Anchor ice thickness (b) Anchor ice growth rate from Exp. 5-5 when the bed velocity is 0.57 m/s, water depth is 0.12 m and air temperature is  $-16^{\circ}\text{C}$ .

## *The Runge-Kutta Method*

---

Runge-Kutta methods are designed to approximate Taylor series methods, but have the advantage of not requiring explicit evaluations of the derivatives of  $f(t, y)$ . The basic idea is to use a linear combination of values of  $f(t, y)$  to approximate  $y(t)$ . This linear combination is matched up to a specific order with a Taylor series for  $y(t)$  to obtain values of the highest possible order  $P$ .

The development of Runge-Kutta formula is illustrated by deriving a method using two evaluations of  $f(t, y)$  per step; the technique employed in the derivation extends easily to the development of all Runge-Kutta type formulas. Given values  $t_i, y_i$ , choose values  $\hat{t}_i, \hat{y}_i$  and constants  $\alpha_1, \alpha_2$  so as to match

$$y_{i+1} = y_i + h[\alpha_1 f(t_i, y_i) + \alpha_2 f(\hat{t}_i, \hat{y}_i)], \quad (\text{D-1})$$

with the Taylor expansion

$$y(t_{i+1}) = y_i + \left[ f(t_i, y_i) + f^{(1)}(t_i, y_i) \frac{h}{2} + f^{(2)}(t_i, y_i) \frac{h^2}{6} \dots \right], \quad (\text{D-2})$$

as closely as possible. In what follows all arguments of  $f$  and its derivatives will be suppressed when they are evaluated at  $(t_i, y_i)$ . It will also be convenient to express  $\hat{t}_i$ ,

$\hat{y}_i$  as

$$\hat{t}_i = t_i + h\beta_1, \quad (\text{D-3})$$

and

$$\hat{y}_i = y_i + \beta_2 hf(t_i, y_i). \quad (\text{D-4})$$

So the object is to match

$$\begin{aligned} R &= \alpha_1 f + \alpha_2 f(t_i + \beta_1 h, y_i + \beta_2 hf) \\ &= (\alpha_1 + \alpha_2) f + \alpha_2 h (\beta_2 ff_y + \beta_1 f_t) + \frac{\alpha_2 h^2}{2} (\beta_2^2 f^2 f_{yy} + 2\beta_1 \beta_2 ff_{ty} + \beta_1^2 f_{tt}) + O(h^3) \end{aligned} \quad (\text{D-5})$$

with the Taylor expansion

$$\begin{aligned} T &= f + \frac{h}{2} f^{(1)} + \frac{h^2}{6} f^{(2)} + O(h^3) \\ &= f + \frac{h}{2} (ff_y + f_t) + \frac{h^2}{6} (f^2 f_{yy} + 2ff_{ty} + f_{tt} + f_t f_y + ff_y^2) + O(h^3) \end{aligned} \quad (\text{D-6})$$

Equating coefficients of similar powers of  $h$  in the above expressions for  $R$  and  $T$ , it is possible to obtain agreement in terms involving  $h^0$  and  $h^1$

$$h^0: \quad \alpha + \alpha_2 = 1, \quad (\text{D-7})$$

and

$$h^1: \quad \alpha_2 \beta_2 = \alpha_2 \beta_1 = \frac{1}{2}. \quad (\text{D-8})$$

Setting  $\alpha_2 = \gamma$  an arbitrary parameter, these equations can be solved exactly to give

$$\alpha_2 = \gamma$$

$$\alpha_1 = 1 - \gamma$$

$$\beta_1 = \beta_2 = \frac{1}{2\gamma}, \quad \gamma \neq 0. \quad (\text{D-9})$$

Combining all of this gives a one-step method of order  $P=2$  if  $\gamma \neq 0$  and  $f$  is sufficiently smooth.

**Runge-Kutta algorithm of order 2:**

To obtain an approximate solution of order  $P=2$ , let  $h = (b - a)/n$  and generate the sequences

$$y_{i+1} = y_i + h \left[ (1 - \gamma)f(t_i, y_i) + \mathcal{F}\left(t_i + \frac{h}{2\gamma}, y_i + \frac{h}{2\gamma}f(t_i, y_i)\right) \right]$$

$$t_{i+1} = t_i + h, \quad i = 0, 1, 2, \dots, n-1, \quad (\text{D-10})$$

where  $\gamma \neq 0$ ,  $t_0 = \alpha$ ,  $y_0 = A$

*Classical Runge-Kutta formulas:*

To obtain an approximate solution of order  $P=4$  on  $[a, b]$ , let  $h = (b - a)/n$  and generate the sequences

$$y_{i+1} = y_i + \frac{h}{6}(k_1 + 2k_2 + 2k_3 + k_4),$$

$$t_{i+1} = t_i + h, \quad i = 0, 1, 2, \dots, n-1, \quad (\text{D-11})$$

where

$$k_1 = hf(t_n, y_n),$$

$$k_2 = hf\left(t_n + \frac{h}{2}, y_n + \frac{k_1}{2}\right),$$

$$k_3 = hf\left(t_n + \frac{h}{2}, y_n + \frac{k_2}{2}\right),$$

$$k_4 = hf(t_n + h, y_n + k_3), \quad (\text{D-12})$$

and  $t_0 = \alpha, y_0 = A.$

In order to solve a second order ordinary differential equation, it is converted to a system of two first order ODE's and then a Runge-Kutta method is applied to each first order ODE to get the solution. For example, the equation

$$C''(y) = F(C, y), \quad (\text{D-13})$$

can be converted into two first order ODE's as follows,

$$v'(y) = F(C, y), \quad (\text{D-14})$$

and  $C''(y) = v(y) \quad (\text{D-15})$